CENTRO DE INVESTIGACIONES
EN OPTICA, A.C.

“FLUORESCENCE QUENCHING-BASED IMMUNOSENSING PLATFORM FOR THE DETECTION OF CLINICALLY RELEVANT PROTEINS”

A thesis submitted in partial fulfillment of the requirements for the degree of PhD in Science (Optics). Include corrections suggested by proofreaders

Present: Edwin Johan Ortiz Riaño

Supervisor: Dr. Eden Morales Narváez

León · Guanajuato · México
February 2023

Fluorescence quenching-based immunosensing Platform for the detection of clinically relevant proteins

Edwin johan Ortiz Riaño

Centro de Investigaciones en Óptica
Biophotonic Nanosensor Laboratory
León, México
2023

I dedicate this work to

To my parents who have always supported me and have given me their love, understanding and example.

To CONACYT for its financial supporting

Natural science does not simply describe and explain nature; it is part of the interplay between nature and ourselves.

Werner Heisenberg

Acknowledgments

I would like to express my gratitude to my parents for their unwavering love and support. I owe a significant part of my achievements, especially this one, to them. While instilling in me the values of responsibility and duty, they also granted me some freedom. However, the most crucial factor was the constant motivation that they provided me to achieve my goals.

Thanks mother and father.

I would like to express my gratitude to CONACYT for its financial support, as well as the Optics Research Center for providing me with the opportunity to be a part of this prestigious institution. I am also immensely grateful to all those who played a role in my academic development, including the researchers, friends, and colleagues who have supported me along the way.

Table of Contents

List of Figures

List of Tables

Preface

Abstract

Immunoassays are nowadays a crucial tool for diagnostics, drug development, and environmental monitoring. However, most immunoassay methods involve cumbersome procedures such as washing, blocking, or separation steps, and in general, require many bioreagents for their operation. In this thesis, "a single-step immunosensing platform based on the fluorescence quenching capability of graphene oxide (GO) and the versatile format offered by the famous 96 microwell plates was developed". This approach was used for the detection of clinically relevant proteins such as Human immunoglobulin G (H-IgG), Prostate Specific Antigen (PSA), and Heat Shock Protein 72 (Hsp72). Our immunosensing method exploits a single antibody conjugated with a fluorophore (F-Ab). The fluorescence intensity of F-Ab (a donor) can be strongly quenched when F-Ab is incubated within GO-covered microwell surfaces (an acceptor) via non-radiative energy transfer. However, when the analyte is added, the formation of immunocomplexes involves non-covalent intermolecular interactions such as hydrogen bonding, electrostatic interactions, hydrophobic, and Van der Waals forces. We hypothesize that such intermolecular interactions hinder the affinity between immunocomplexes and GO-covered microwell surfaces, and as a consequence, in the proposed biosensing platform, the aforementioned non-radiative energy transfer is not observable upon immunocomplexes formation. Moreover, we proved that the studied immunosensing platform can be successfully employed to monitor the association process occurring between proteins, and therefore, determine binding kinetic constants whose values obtained match with those values reported in the literature and by the respective suppliers. All in all, we developed a single-step immunosensing platform where the biodetection can be monitored in real-time, avoiding cumbersome procedures like washing, separation, or blocking steps, and it is a relatively cost-effective system as the assay is around 0.47 USD per test at the laboratory scale. Furthermore, our outstanding immunosensing platform is a potential method for the clinical diagnosis of prostate cancer and acute kidney injury, as demonstrated here via the analysis of real samples. In addition, as the association process is monitored, this technology can be used for the determination of the antibody affinity, or in biochemistry studies where the understanding of structure/function relationships are in function of protein-protein interactions, or even in the validation of potential biomarkers where binding kinetic parameters are relevant.

Objectives

General Objective

To develop and validate an immunosensing platform based on the quenching of fluorescence caused by Graphene oxide, and detect clinically relevant proteins (e.g. Human immunoglobulin G, Prostate Specific Antigen, Heat shock protein 72, and antibodies against SARS-CoV-2).

Specific Objectives

- To review the literature about optical-based immunosensor approaches that employ graphene oxide to understand the advantages that provide this material in the detection of diverse clinically relevant proteins.
- To apply the immunosensing platform for the detection of proteins in real samples.
- To carry out the respective validation parameters of analytical methods such as limits of detection and quantification, precision, and the analytical range of detection.
- To utilize different fluorophores like QDs and Fluorescein isothiocyanate (FITC) to validate that the immunosensing platform can operate with diverse fluorophores.
- To demonstrate that the immunosensing method can be used for the determination of binding kinetic constants.

Academic and scientific achievements derived from this PhD thesis

Publications

1. Ortiz-Riaño, E.J., Mancera-Zapata, D.L., Ulloa-Ramírez, M., Arce-Vega, F., Morales-Narváez, E., **2022**. Measurement of Protein Kinetics Using a Liquid Phase-Based Biosensing Platform. *Anal. Chem.* (**Front Cover Article**)
2. Ortiz-Riaño, E.J., Avila-Huerta, M.D., Mancera-Zapata, D.L., Morales-Narváez, E., **2020**. Microwell plates coated with graphene oxide enable advantageous real-time immunosensing platform. *Biosensors and Bioelectronics* 165, 112319.
3. Avila-Huerta, M.D., Ortiz-Riaño, E.J., Mancera-Zapata, D.L., Cortés-Sarabia, K., Morales-Narváez, E., **2021**. Facile Determination of COVID-19 Seroconversion via Nonradiative Energy Transfer. *ACS Sens.* 6, 2136–2140.
4. Avila-Huerta, M.D., Ortiz-Riaño, E.J., Mancera-Zapata, D.L., Morales-Narváez, E., **2020**. Real-Time Photoluminescent Biosensing Based on Graphene Oxide-Coated Microplates: A Rapid Pathogen Detection Platform. *Anal. Chem.* 92, 11511–11515. (**Front Cover Article**)
5. Rodríguez-Nava, C., Cortés-Sarabia, K., Avila-Huerta, M.D., Ortiz-Riaño, E.J., Estrada-Moreno, A.K., Alarcón-Romero, L. del C., Mata-Ruíz, O., Medina-Flores, Y., Vences-Velázquez, A., Morales-Narváez, E., **2021**. Nanophotonic Sialidase Immunoassay for Bacterial Vaginosis Diagnosis. *ACS Pharmacol. Transl. Sci.* 4, 365–371.

Relevant conferences and presentations

2022	Graphene oxide-based nanotechnology for the detection of clinical relevant proteins. II congress of engineering and physics applied to biomedicine.Guanajuato, Mexico.
2022	Graphene oxide-based nanotechnology for the quantification of proteins kinetic constants. Graduate student poster session, Guanajuato, Mexico.
2021	Real-time biosensing platform based on quenching of fluorescence. The 25th international conference on miniaturized systems for chemistry and life science (µtas 2021), Palm Springs, CA USA.
2020	Microwells coated Graphene oxide as a photoluminescence biosensing platform. LatinXChem Twitter conference.
2019	Quenching of fluorescence as a principle of protein detection. Talk event at Centro de Investigaciones en Óptica, Guanajuato, Mexico.

Chapter 1

Theoretical Framework

The sensor field emerged due to the need for early medical diagnosis and the detection of some bacteria that affect the environment.[1] Over the last 20 years, the interest in the development of new biosensors that permit the early detection of several diseases to treat them on time has increased. Optical biosensors used optical techniques to identify chemical or biological species.[2] These biosensors offer great advantages such as high sensitivity and specificity, and also the possibility of remote sensing. For these reasons, it is important to describe what are biosensors.

1.1 Optical Biosensors

1.1.1 What is a biosensor?

A definition of a sensor might be *"anything that responds to an external input"*.[3] Another definition a little bit precise is *"a device that receives a stimulus and responds with an electrical signal"*.[4] Thereby, the definition of sensor seems to be subject to the perspectives of the applications. Therefore, in areas such as biomedical engineering or medical physics these definitions are not convenient due to a device that only reveals the presence or absence of a physical parameter would be more a detector than a sensor. So, a more suitable definition for application in these areas might be "a device that responds to a physical input of interest with a recordable, functionally related output that usually is electrical or optical".[3] In the biomedical field "physical input" also encloses the biological, chemical, and biochemical species.

Often, sensor and transductor are both used in the context of measurement systems which generate a certain degree of confusion. A good definition of a transductor is *"a device that converts any type of energy into another, being the latter, in general, electrical"*.[3] Then, a sensor satisfied this definition and might be described as a transductor. Somewhat, the difference between a sensor and a transductor is that the sensor collects information from the real world and converts that information into an electrical signal whereas the transductor just transforms energy from one form to another.[5]

So, it can be said that a biosensor is an analytical device that can detect chemical, biological, or biochemical species and even microorganisms.[1] In general, biosensors used a biological biorecognition element that detects the presence of an analyte and makes a

physical or chemical response, which is transformed into an optical or electrical signal. Biosensors have a vast range of applications such as clinical diagnostics, pharmaceutical development, environmental monitoring, and food quality monitoring among others.

1.1.2 Basic elements of a biosensor

Now the main objective is to describe the basic elements involved in biosensing, in general. Figure 1-1 depicts these basic elements that constitute a biosensor. First, the sampling unit is where the analyte, to be detected, is placed. Then, the biorecognition unit is where the biological biorecognition element is located and it binds with a specific analyte providing high specificity. The biorecognition element can be an antibody, an enzyme, a biomimetic material, or even cells. The stimulation unit is also important because it extracts a response from the biodetection which might be, in general, optical or electrical.[1] In the transduction process, the chemical or physical response, obtained from the biological biorecognition, is transformed into these optical or electrical signals that are read by the detection unit.

Talking about optical biosensors, it is evident that the stimulation is in the form of an optical input. Therefore, in the transduction process, there is a change in the amplitude (intensity), polarization, phase, or frequency of the input light.[4] Frequently, the sensitivity and selectivity of a biosensor could be improved by immobilizing the biorecognition element onto an optical element such as a fluorophore, optical fiber, etcetera.[1] Indeed, many of the biorecognition elements used in biosensing (commercially) are found already conjugated with diverse fluorophores to improve the parameters previously mentioned.

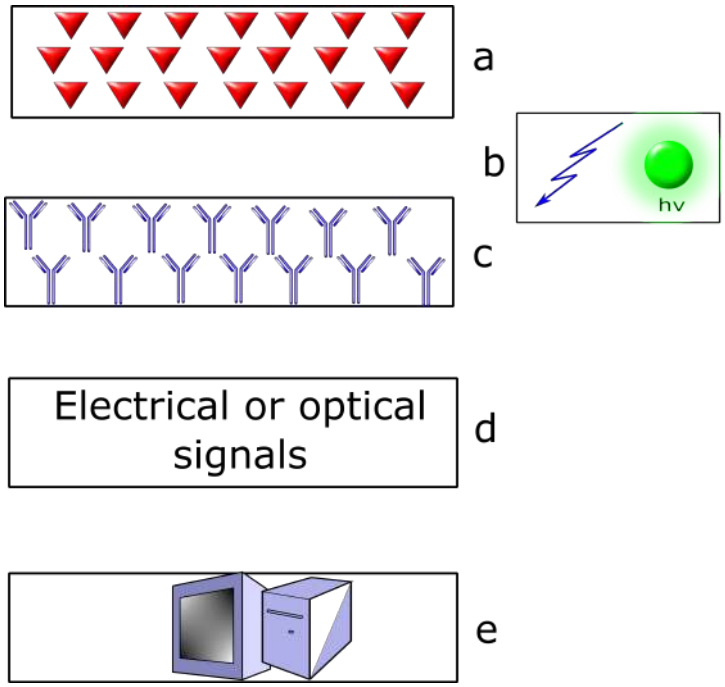

Figure 1-1. Units of a biosensor. **a)** sampling, **b)** stimulation, **c)** biorecognition, **d)** transduction, **e)** detection.

1.1.3 Biorecognition

Previously, it was mentioned some of the elements that could work as biological biorecognition elements: antibodies, enzymes, biomimetic materials, or cells. The most important characteristic of these elements is their great selectivity to recognize a specific analyte. Indeed, the specificity of the biorecognition element is pivotal for the biosensing field. The molecular bioreceptors most used for biorecognition in biosensing are described here. Currently, there are a lot of molecular bioreceptors used in biosensing such as peptides or polymers.

Enzymes: are organic molecules that are considered biological catalysts. The catalysts are molecules that accelerate chemical reactions.[6] The specificity of an enzyme with its respective reactant (substrate) is unique. That is, an enzyme acts over a specific substrate, which, is chemically modified to be transformed into one or more products.[1] This unique specificity of enzymes is what makes them excellent candidates to be biorecognition elements. The specific bind sites where substrates adhere to enzymes are known as active sites.[6] Moreover, the interaction between analytes/substrates with enzymes can provide optical transduction by producing a product that absorbs at a different wavelength.[1]

Antibodies: there are proteins that, given their highly specific aminoacid sequence, adhere to determined analytes or antigens. The association of antibody-analyte pair also can be described as a lock (antibody) that can only open with a specific key (analyte) combination, as depicted in figure 1-2. The specificity of antibodies makes them excellent candidates to be used as biorecognition elements. Also, an optical transducer (such as a fluorophore) can be used to tag antibodies.

Lectins: they also are proteins that bind to oligosaccharides and some glycoproteins such as immunoglobulins.[1] For that reason, the lectins are used as a biorecognition element for this class of molecules. These proteins are employed in biosensors for the detection of glucose.

DNA: it is known that DNA (Deoxyribonucleic Acid) is a macromolecule with an essential biological importance because it constitutes the fundamental deposit of genetic information.[6] DNA is composed of double-polynucleotide helicoidal chains which bind via four nucleobases (Guanine, Cytosine, Adenine, and Thymine). The complementarity principle of DNA makes it an exceptional biorecognition element to detect pair bases of DNA or RNA.

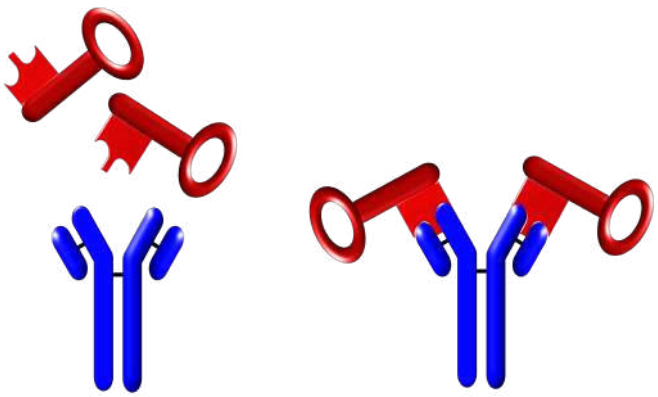

Figure 1-2. Lock-Key representation for the antibody-analyte association.

1.1.4 Optical transduction

The transduction process in a biosensor consists of transforming the biological activity that has been measured by the biorecognition element into a quantifiable signal such as a current, a voltage, or an optical signal.[4] Particularly for optical biosensors, there are a long variety of optical manifestations (transductions) that are summarized in Table 1-1. As previously mentioned, the transduction process consists of the variation of some parameters of the incident light like the phase, the intensity, or the frequency. Phase variations could be due to changes in the real part of the refractive index that could express as a change in the polarization of light, in the optical field distribution (due to a particular interference), or an alteration in the features of propagation for instance in an optical fiber.[1]

On the other hand, intensity changes are related to some loss mechanisms such as reflection, absorption, or transmission. The changes in frequency could be due to phenomena like stokes shift, Raman scattering, or non-linear optical interactions for example second-harmonic generation.[4]

Table 1-1. Overall forms of optical transduction.

Formsof Optical Transduction		
Phase Changes	**IntensityChanges**	**Frequency Changes**
Are produced by variations in the refraction index.	Absorption Propagation	They are principally due to Stokes shifts thanks to different phenomena: Fluorescence,Raman scattering, or nonlinear optics.
	Theyare due to any loss mechanism by transmission.	

1.1.5 Detection methods used in biosensing

There are many sensing methods employed in the detection of analytes in a biosensor. Therefore, it cannot be said that existed a preferential method in the biosensing area.[7] Some of the most used approaches in the biosensing area are surface plasmon resonance (SPR), enzyme-linked immunosorbent assay (ELISA), high-performance affinity chromatography, and radioligand binding assay, among others.[1] Although many biosensing methods are available, all can be classified into two groups: label-free methods and label-based methods.[1]

Label-based detection: A label is understood as a foreign molecule that is chemically bound to a biorecognition element, and that can transmit information from molecular events.[7] The labels either fluorescent, chemiluminescent, or nanoparticles frequently involved covalent or non-covalent interactions between certain chemical groups (such as hydrogen bonds, electrostatic interactions, π-effects, or Van der Waals forces). Particularly, detection methods based on fluorescent labels are the most used due to they are easy to use, they are stable, and also because they offer good sensitivity and resolution.[8] Currently, there are a lot of fluorescent labels available such as quantum dots, small organic

molecules, several fluorophores, and even fluorescent proteins.[1] All of these fluorescent molecules are biofunctionalized for different applications which made them excellent candidates in the biosensing area.

Label-free detection: is based on molecular biophysical properties such as refraction index, molecular weight, or frequency to monitor interaction related to the biorecognition.[8] The great advantage of these methods is that the detection can be made in real-time. So, many techniques can be used and the choice depends on the application.

1.2 Physical phenomena involved in optical biosensors

1.2.1 Fluorescence

Over the last 30 years, the use of fluorescence in biological science has increased considerably.[9] Indeed, not only in biology but also in areas like biochemistry or biophysics fluorescence has been used as a fundamental tool of investigation. Currently, there are a lot of luminescence techniques for the development of research in diverse areas of science. For this reason, it is important to talk about luminescence, particularly fluorescence.

Luminescence is the light emission of any substance from its electronically excited states.[9] Formally, luminescence is divided into two categories: fluorescence and phosphorescence which depend on the nature of the excited state. A general definition of fluorescence would be the emission of light, from an atom or molecule, as a consequence of the absorption of electromagnetic radiation. This definition also would be correct for phosphorescence, so a better definition is necessary. Another definition for fluorescence is the transition of photoexcited specimens from the first excited singlet state to the ground state.[10] In the excited singlet states, the electron is paired (by an opposite spin) to a second electron in the ground state and therefore return to the ground state is spin allowed and occurs rapidly followed by the emission of a photon of less energy than the absorbed one. In contrast, phosphorescence is the emission of light from triplet excited states in which electron spin has the same orientation that the electron in the ground state.[11] Fluorescence lifetimes are typically in nanoseconds due to transitions to the ground state are spin allowed whereas phosphorescence lifetimes are in milliseconds to seconds.

The process that happened between the absorption and emission of light typically is represented in Jablonski diagrams. Figure 1-3, depicts one of these diagrams where are represented the mechanisms of fluorescence and phosphorescence. At room temperature, the thermal energy is not enough to populate excited vibrational states. For this reason, the emission and absorption of light, frequently, occur from molecules with lower vibrational energy.[9,11] When a photon is absorbed, a fluorophore is excited until a high vibrational level either from S_1 or S_2 where (with a few rare exceptions) the fluorophore rapidly relaxes to the lower vibrational level of S_1. This process is known as internal conversion, see figure 1-3. Some molecules in the state S_1 can go to spin conversion to the triplet state T_1 in a process known as intersystem crossing, the mechanism of the phosphorescence.[10,11]

1.2.2 Quenching of fluorescence

The quenching of fluorescence is any chemical and/or physical process in which the intensity of a given signal decreases.[10,11] Diverse are the mechanisms that could produce the quenching for instance energy transfer, molecular rearrangements, or collisional quenching among others. Particularly, the concern in this part is to describe the quenching produced by collisional encounters between an excited-state fluorophore and some other molecule, which is called the quencher. This is known as collisional or dynamic quenching.

A fundamental requirement of collisional quenching is that must have physical contact between the quencher and the fluorophore.[9] Then, when such contact occurs, the excited-state fluorophore returns to the ground state without the emission of a photon and, in general, without any permanent change in the molecule. This is a time-dependent process, meaning that to the contact between the quencher and the fluorophore occurs, some time must pass. Exist another type of quenching known as static quenching. This process occurs when fluorophores form non-fluorescent complexes with quenchers.[9,11] So, in both collisional and static mechanisms, physical contact must exist between the quencher and the excited-state fluorophore for the quenching of fluorescence intensity occurs.

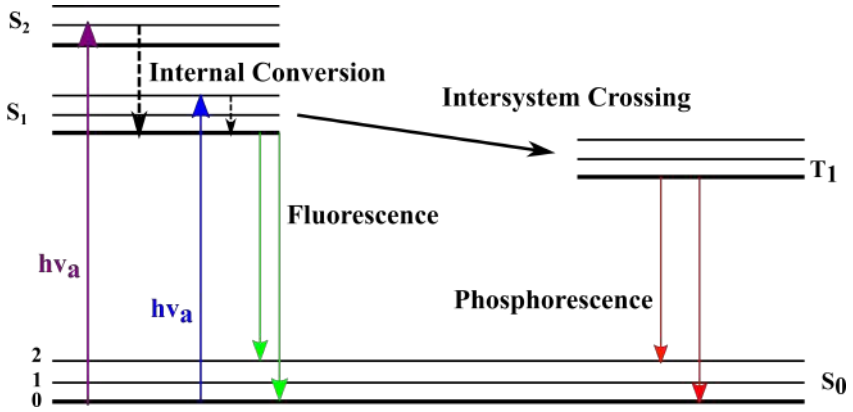

Figure 1-3. Jablonski Diagram.

1.2.3 Fluorescence Resonance Energy Transfer: FRET

Another process that takes place during the excited state of a fluorophore is the Fluorescence Resonance Energy Transfer FRET. This phenomenon occurs when the emission spectrum of a fluorophore known as the donor overlaps with the absorption spectrum of another molecule known as the acceptor.[9] Thus, the donor, electronically excited, can transfer its absorption energy to the acceptor in a non-radiative way by long-range dipole-dipole interactions. So, the theory to describe the FRET phenomenon consists of shaping a fluorophore as an oscitant dipole that can exchange energy with another dipole of similar frequencies.[9,10] The classic mechanics is enough to explain correctly this phenomenon.

The transfer of non-radiative energy occurs at distances bigger than solvent effects of short-range.[12] As mentioned previously, dynamic or static quenching demand molecular contact whereas FRET does not require such molecular contact. Moreover, the acceptor does not necessarily need to be fluorescent. The acceptor might be fluorescent but different from the donor; it not might be fluorescent and different from the donor; it may be

fluorescent and the same that the donor. The energy transfer rate depends on different parameters such as the scope of spectral overlap between the emission spectrum of the donor and the absorption spectrum of the acceptor, the quantum yield of the donor, the relative orientation of the dipoles of both the donor and the acceptor and the distance between them.[9,10,12] FRET phenomenon manifests with a decrease in the fluorescence intensity (emitted by the fluorophore) and a reduction of the excited-state lifetime.[12] Last, the distance in which 50 % of the excitation energy is transferred to the acceptor is known as the Förster distance R_0 and, typically, is between a range of 20 to 60 Å.[9,10]

1.2.4 Comparison between FRET and static and dynamic quenching

As described previously, the quenching of fluorescence can occur via the FRET phenomenon, dynamic or static processes, but how these processes can be distinguished? Somehow has already been shown a bit the difference when it was argued that the quenching, both the dynamic and the static, molecular contact is needed, unlike the FRET phenomenon that does not require such molecular contact. As a consequence, the range of quenching (dynamic and static) is sensitive to molecular factors that affect the contact probability for instance the interaction between charges.[9] In contrast, as FRET does not require molecular contact, this phenomenon is due to interactions through space and it is not affected by molecular factors.

In other words, the principal difference is that the quenching (dynamic and static) is due to short-range interactions between the fluorophore and the quencher whereas FRET is caused by long-range polar interactions within the donor and the acceptor.[9,10] When the quencher makes contact with the excited fluorophore, its exciting electron or electrons return to the ground state and the energy is dissipated as heat. How in dynamic and static quenching there is molecular contact, the electron clouds of both molecules interact with each other. These interactions between electron clouds are usually known as electron exchange or exchange interactions due to electrons can move within molecules at these short distances.[10] In contrast, considering a Förster distance of 30 Å, this distance would be so huge for a direct interaction between electron clouds. So, FRET is effective for relatively long distances whereas dynamic and static quenching are efficient in short distances, which means when electron clouds are inside of 2 Å.[9,10,12]

1.3 Graphene and its derivate: Graphene Oxide

Graphene is a bidimensional layer of carbon atoms binding by sp^2 hybridization arranged in a hexagonal network.[13,14] Graphite consisted of infinite sheets of Graphene stacked one on top of another, so, it is said that graphene is the fundamental unit of Graphite, as depicted in figure 1-4. Since its discovery, it has attracted the attention of several fields such as physics, chemistry, and materials science due to its astounding properties. Indeed, graphene not only has been a central topic in fundamental science but also has been a target for cutting-edge applications. The Nobel Prize in physics 2010 was awarded to Andre Geim and Konstantin Novaselov for their theoretical contributions to the understanding of this great material. The electrochemical and electronic properties

of Graphene, and its derivatives, strongly depend on its structure.[13] Due to every sheet of this material is finite, its composition is based on a basal sheet and edges. Indeed, there are two types of edges: zigzag and armchair, which are shown in Figure 1-4. These classes of structures have a profound influence on the electrochemical and electronic properties of Graphene and its derivatives.[13,14] Single-sheet Graphene is considered a gapless semiconductor (solids in which the conduction and valence bands meet at the Fermi level).[13]

Graphene can be oxidated by strong oxidants such as potassium permanganate ($KMnO_4$) or sulfuric acid (H_2SO_4) thus obtaining graphene oxide (GO).[14] So, the oxidation produces a graphene layer randomly binding with functional groups containing oxygen atoms. Carbon atoms are covalently bonded to the oxygen atoms, converting them from the sp^2-hybridized state (in graphene) into the sp^3-hybridized state.[15] These oxygen-containing functional groups might be considered defects introduced into the ideal Graphene sheet converting the electronic structure of gapless semiconductor into an insulator. GO acquires unique properties that graphene does not possess such as hydrophilicity and a tunable bandgap, the latter responsible for the electronic and optical properties of this material.[15] The atomic ratio C/O changes to some extent, but for samples of GO sufficiently oxidated, this proportion is 2:1 approximately.[13] Just like Graphene, the lateral size of GO can vary from hundreds of nanometers to hundreds of micrometers due to more atoms of both oxygen and carbon accumulated. The truly 2D form of GO can only exist in suspensions where it is completely exfoliated to single-layer sheets, and also, such layers are negatively charged thanks to the formation of an electrical double layer in the GO/water interface.[15] On the other hand, GO chemical composition depends on both its structure and its environment.[14] Indeed, its chemical structure is not fully understood and is still under investigation.

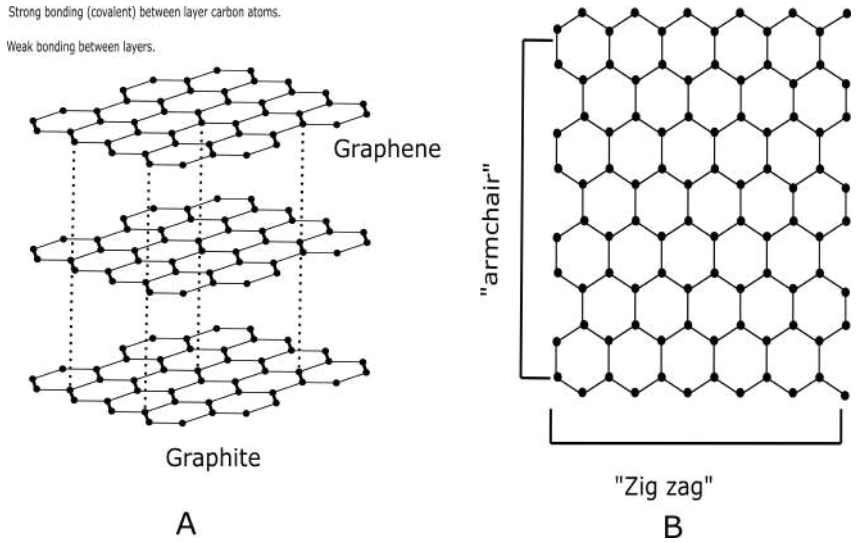

Figure 1-4. A. Graphene and Graphite; B. Type of edges in Graphene.

Due to its plane shape and chemical structure, graphene has some advantages over other nanomaterials for biosensing applications. For instance, the atomic thickness of a sheet and its high surface-to-volume ratio makes this material very sensitive to local environmental changes, being a very important candidate to improve the sensitivity of analytes detection, an aspect so important in the performance of a biosensor.[16] Furthermore, GO and Graphene can be conjugated with biomolecules via hydrophobic interactions and

$\pi-\pi$ stacking showing excellent biocompatibility.[17] Experimental and theoretical studies have shown that both Graphene and GO are highly efficient quenchers of photoluminescence being exceptional candidates for FRET-based biosensors.[17,18] In sum, due to the excellent properties of graphene and GO including a heterogeneous chemical and electronic structure, the ability to be suspended in the liquid phase and form colloidal suspensions in water, and the possibility to be tuned as a conductor, semiconductor, or insulator; graphene-based biosensors have several advantages over nanomaterials-based biosensor.[16]

1.4 Validation parameters of analytical methods

1.4.1 Linear regression: Linear least-squares method

Linear regression is a mathematical model used to approximate the dependence relationship between an independent variable x and a dependent variable y.[19] The method most employed for this end is the Linear Squares Approximation in which it is assumed that y errors are bigger than x errors. Then, the purpose of this approximation is that the sum of vertical distances squares between each experimental point and the straight-line fit be minimal. This vertical distance is known as residual.[20] Equations for the slope m and the y-intercept b that minimize the sum of residuals are the following,

$$m = \frac{n\sum(x_i y_i) - \sum x_i \sum y_i}{n\sum(x_i^2) - (\sum x_i)^2} \tag{1-1}$$

$$b = \frac{\sum(x_i^2)\sum y_i - \sum(x_i y_i)\sum x_i}{n\sum(x_i^2) - (\sum x_i)^2} \tag{1-2}$$

where n is the total amount of data in the fitting. With these equations, we can obtain a straight line that better fits to set of experimental data. For the reliability of results is necessary to know the uncertainty of both m and b which are in terms of the uncertainty of y-values.[21]The uncertainty expressions for equations 1-1 and 1-2 are the following,

$$s_m = \sqrt{\frac{n s_y^2}{n\sum(x_i^2) - (\sum x_i)^2}} \tag{1-3}$$

$$s_b = \sqrt{\frac{s_y^2 \sum(x_i^2)}{n\sum(x_i^2) - (\sum x_i)^2}} \tag{1-4}$$

where s_m and s_b is an estimation of the uncertainty (standard deviation) to the slope and the intercept, respectively. s_y is the y-values uncertainty which is defined as:

$$s_y = \sqrt{\frac{\sum(d_i^2)}{n-2}} \tag{1-5}$$

Where d_i are residual values. The coefficient of determination is fundamental in linear regression analysis since indicates the goodness of the fitting.[21] Values of this parameter are between 0 and 1 so values close to 1 indicate that the fitting is good to the set of experimental data. The coefficient of determination is given by:

$$R^2 = \frac{(n\sum(x_i y_i) - \sum x_i \sum y_i)^2}{(n\sum(x_i^2) - (\sum x_i)^2) - (n\sum(y_i^2) - (\sum y_i)^2)} = \frac{s_{xy}^2}{s_x^2 s_y^2} \tag{1-6}$$

Where s_x^2 and s_y^2 are the x and y standard deviation, respectively. The covariance of (x,y) is given by s_{xy}^2.Then, we have all the equations needed for the Linear least-squares method.

1.4.2 Calibration curves

In an analytical method, a calibration curve represents the method's response to known concentrations of an analyte.[20,21] So, the curve is constructed from serial dilutions which are obtained from a stock solution. The dilution that contains all the reactive involves in the analytical method, except the analyte, is known as the blank and has an important role since measures the response of the analytical method either to impurities present in reactive or its behavior in absence of the analyte. The calibration curves determine the set of concentrations suitable to the quantification of a particular analyte, that is, allow establishing the linear range of detection. The linearity of calibration curves is reported in the Literature as a requirement for the validation calculus of a given analytical method.[20] When data does not show a linear relation, a mathematical transformation, in general logarithmic, is made to obtain a linear relation of data. The linear interval might vary from one matrix (the constituents, apart from the analyte, of the given sample) to another due to the different interferences present in every matrix.

1.4.3 Limit of detection, quantification, and analytical range

The parameters that validate the quality of an analytical method are the sensitivity, the time needed to detect, the ease of analysis, and the cost of the method.[22] Also, the limit of detection LOD and quantification LOQ are of vital importance to analyzing the efficiency of the method.[20] LOD and LOQ are terms that denote the minimal concentration detectable by the analytical method. LOD refers to the minimal analyte concentration detectable without the consideration of another parameter. On the other hand, LOQ refers to the minimal analyte concentration detectable with acceptable levels of precision and accuracy under determined assay conditions.[20,22] The most used methods to determine these parameters are via signal-to-noise relation and the blank method. In particular, in this case, the blank method was used to obtain LOD and LOQ. So, this method requires a good performance of the blank replicates for reliable results. The expression to estimate LOD is the following:

$$LOD = LoB + 3(SD_{Lowanalyteconcentration}) \tag{1-7}$$

Where LoB ($LoB = \Delta B_l + 1.645(SD_{Bl})$) is the limit of the blank and is the behavior

resulting from blank replicates. ΔB_l is the average of the blank and SD_{Bl} its standard deviation. $\mathrm{SD}_{Lowanalyteconcentration}$ is the standard deviation of the lowest concentration of analyte detected. The value obtained by equation 1-7 is interpolated on the lineal equation obtained from fitting and this LOD is finally determined. The equation to determine LOQ is given by:

$$LOQ = \Delta B_l + 10(SD_{Bl}) \tag{1-8}$$

Likewise, the value is interpolated on the linear equation to obtain LOQ. On the other hand, the analytical range is defined as the interval of concentration where the analyte can be detected while maintaining linearity.[20]

1.4.4 Precision and sensitivity

The precision is defined as the dispersion obtained from repeated measurements of the same homogeneous sample.[23] In general, the precision is expressed via the coefficient of variation CV and the less this value is, the more precise will be the measurements. The equation used to determine CV is,

$$CV = \frac{SD}{\Delta x}100\% \tag{1-9}$$

where SD is the standard deviation and Δx is the average. On the other hand, sensitivity is the capacity of an analytical method to distinguish little variations of analyte concentrations.[20] Usually, the sensitivity is related to the slope: the bigger the slope value is, the more sensitive will have the analytical method.

1.5 References

1. Paras, P. Optical Biosensors. In Introduction to Biophotonics; John Wiley & Sons, Ltd, 2003; pp 311–356. https://doi.org/10.1002/0471465380.ch9.

2. Wang, P.; Liu, Q. Basics of Sensors and Measurement. In Biomedical Sensors and Measurement; Wang, P., Liu, Q., Eds.; Springer Berlin Heidelberg: Berlin, Heidelberg, 2011; pp 17–50. https://doi.org/10.1007/978-3-642-19525-9_2.

3. Jones, D.; Watson, J. Biomedical Sensors; Momentum Press, 2010.

4. McGrath, M. J.; Scanaill, C. N. Sensing and Sensor Fundamentals. In Sensor Technologies: Healthcare, Wellness, and Environmental Applications; McGrath, M. J., Scanaill, C. N., Eds.; Apress: Berkeley, CA, 2013; pp 15–50. https://doi.org/10.1007/978-1-4302-6014-1_2.

5. Khanna, K. Nanosensors: Physical, Chemical, and Biological., 1st ed.; CRC Press, 2012.

6. De Robertis, E. Biologia Celular y Molecular; El Ateneo: Argentina, 2005.

7. Syahir, A.; Usui, K.; Tomizaki, K.; Kajikawa, K.; Mihara, H. Label and Label-Free Detection Techniques for Protein Microarrays. Microarrays 2015, 4 (2). https://doi.org/10.3390/microarrays4020228.

8. Megger, D. A.; Pott, L. L.; Ahrens, M.; Padden, J.; Bracht, T.; Kuhlmann, K.; Eisenacher, M.; Meyer, H. E.; Sitek, B. Comparison of Label-Free and Label-Based Strategies for Proteome Analysis of Hepatoma Cell Lines. Biochimica et Biophysica Acta (BBA) - Proteins and Proteomics 2014, 1844 (5), 967–976. https://doi.org/10.1016/j.bbapap.2013.07.017.

9. Introduction to Fluorescence. In Principles of Fluorescence Spectroscopy; Lakowicz, J. R., Ed.; Springer US: Boston, MA, 2006; pp 1–26. https://doi.org/10.1007/978-0-387-46312-4_1.

10. Jameson, D. Introduction to Fluorescence, 1st ed.; CRC Press, 2015.

11. Fleming, K. G. Fluorescence Theory. In Encyclopedia of Spectroscopy and Spectrometry (Third Edition); Lindon, J. C., Tranter, G. E., Koppenaal, D. W., Eds.; Academic Press: Oxford, 2017; pp 647–653. https://doi.org/10.1016/B978-0-12-803224-4.00357-5.

12. Hussain, S. An Introduction to Fluorescence Resonance Energy Transfer (FRET). arXiv 2009.

13. Pumera, M. Graphene-Based Nanomaterials and Their Electrochemistry. Chem. Soc. Rev. 2010, 39 (11), 4146–4157. https://doi.org/10.1039/C002690P.

14. Toshiaki, E.; Tsuneya, A. Physics and Chemistry of Graphene, 1st ed.; Jenny Stanford Publishing: New York, 2013.

15. Dimiev, A. M. Mechanism of Formation and Chemical Structure of Graphene Oxide. In Graphene Oxide; John Wiley & Sons, Ltd, 2016; pp 36–84. https://doi.org/10.1002/9781119069447.ch2.

16. Morales-Narváez, E.; Merkoçi, A. Graphene Oxide as an Optical Biosensing Platform: A Progress Report. Advanced Materials 2019, 31 (6), 1805043. https://doi.org/10.1002/adma.201805043.

17. Morales-Narváez, E.; Merkoçi, A. Graphene Oxide as an Optical Biosensing Platform. Advanced Materials 2012, 24 (25), 3298–3308. https://doi.org/10.1002/adma.201200373.

18. Wang, Y.; Li, Z.; Wang, J.; Li, J.; Lin, Y. Graphene and Graphene Oxide: Biofunctionalization and Applications in Biotechnology. Trends in Biotechnology 2011, 29 (5), 205–212. https://doi.org/10.1016/j.tibtech.2011.01.008.

19. Danzer, K.; Currie, L. A. Guidelines for Calibration in Analytical Chemistry. Part I. Fundamentals and Single Component Calibration (IUPAC Recommendations 1998). Pure and Applied Chemistry 1998, 70 (4), 993–1014. https://doi.org/10.1351/pac199870040993.

20. Maria Dosal; Villanueva, M. Curva de Calibración en los métodos analíticos, 2008.

21. Harris, D. Análisis químico cuantitativo, 3rd ed.; Reverté, 2013; Vol. 1.

22. Shrivastava, A.; Gupta, V. Methods for the Determination of Limit of Detection and Limit of Quantitation of the Analytical Methods. CYS 2011, 2, 21–25. https://doi.org/10.4103/2229-5186.79345.

23. Findlay, J. W. A.; Smith, W. C.; Lee, J. W.; Nordblom, G. D.; Das, I.; DeSilva, B. S.; Khan, M. N.; Bowsher, R. R. Validation of Immunoassays for Bioanalysis: A Pharmaceutical Industry Perspective. Journal of Pharmaceutical and Biomedical Analysis 2000, 21 (6), 1249–1273. https://doi.org/10.1016/S0731-7085(99)00244-7.

Chapter 2

Optical biosensor approaches based on graphene oxide, state of the art

Graphene oxide has been used in the last years in the development of optical biosensing approaches due to its outstanding optical and chemical features. In this chapter, a revision of the literature was made to determine the role of Graphene oxide in the development of optical biosensing approaches. The advantages and disadvantages of each optical method, the detection mechanism, and its respective potential applications in medical diagnosis are described.

2.1 Photoelectrochemical-based biosensors

The photoelectrochemical mechanism (PEC) is based on the conversion of photons into electricity resulting from the separation of electric charges, and subsequently, charge transfer just after photon absorption during the irradiation.[1] This is a low-cost analytical method that involves charge transfer processes between a photoactive material, the analyte (to be detected), and an electrode that is under constant light irradiation. Light sources in photoelectrochemical methods are used as excitation agents whereas the electric current is determined as the detection signal output. In this process, three procedures are involved i) light absorption by a light-harvesting semiconductor, ii) generation of photoexcited charge carriers; electrons e^- and holes h^+, and iii) separation of photoexcited charge carriers to the respective terminals.[1] In a conventional photoelectrochemical biosensor, the presence of the target biomolecule (the analyte) induces an increase of the photocurrent after the oxidation, so such photocurrent generated is directly proportional to the amount of analyte.

An important and distinguished aspect of graphene-based photoelectrochemical biosensors is the high sensitivity that provides.[2,3] These biosensors have been used for the detection of different clinically relevant analytes such as tumoral biomarkers[3,4], heart failure related biomarker[5], bacterial infections biomarker[6], prostate cancer biomarker[7] and also for the detection of toxins; for instance, microcystin-LR.[2] The majority who use this biosensing method report limits of detection in the order of pg mL^{-1}, see table 4-1, high sensitivity in the detection of such analytes and excellent specificity important characteristics in biosensing applications.

A photoelectrochemical biosensor was developed for the detection of alpha-fetoprotein (AFP) which is a protein that normally only is produced in the developing fetus. When this protein is found in adults, it can serve as a tumoral marker.[3] In this approach, a photoelectrochemical electrode based on reduced graphene oxide was fabricated which provides a high surface area and a stable pathway for electron transport. The antibody, anti-AFP, is then immobilized onto the electrode and the AFP analyte was conjugated with the polymer PFBT (synthesized by authors) and glucose oxidase (AFP-PFBT-GOD). So, when AFP-PFBT-GOD adheres to the electrode-reduced-GO, PFBT dots can absorb visible light which results in the migration of photogenerated electrons to the electrode, and hence an electric signal is registered. The authors reported that the PEC biosensor based on reduced GO exhibited a linear detection range of 0.05-100 ng mL^{-1} and a LOD of 0.05 ng mL^{-1} reflecting the extremely high sensitivity of the biosensor.[3] Other photoelectrochemical biosensor was designed for the detection of AFP where the electrode also was covered with reduced GO and then the AFP analyte and graphite carbon nitrate were immobilized onto the electrode surface. Bovine serum albumin is added to avoid non-specific interaction and then horseradish peroxidase-labeled antibody was captured onto the sensing interface. The PEC signal originated from graphite carbon nitrate which is an excellent photoactive material and the signal was amplified by the electrode-reduced GO-covered electrode. The biosensor showed a linear detection range of 1-40 pg mL^{-1} with an ultralow LOD of 1 pg mL^{-1}. So, the second proposal showed a lower LOD for AFP detection.[4]

Heart failure is the deficiency of the heart to maintain the body's blood circulation.[5] The amino-terminal pro-B-type natriuretic peptide (NT-pro BNP) is one of the most important biomarkers for the diagnosis of lower-degree heart failure.[5] A sandwich-type PEC biosensor was constructed for the detection of NT-pro BNP where flower-like Bi_2WO_6/Ag_2S nanoparticles were employed as PEC matrix, and GO and polydopamine composite as signal labels. Here, the GO helps to amplify the photocurrent signal due to its brilliant conductivity speeding up the electron transfer. The linear response of the biosensor ranged from 0.1 pg mL^{-1} to 100 ng mL^{-1} with a LOD of 0.03 pg mL^{-1}. Moreover, the PEC biosensor exhibited high stability and selectivity.

Another sandwich-type PEC biosensor was designed for the detection of the prostate-specific antigen where reduced GO-doped with $BiVO_4$, which are photovoltaic materials with high electrical conductivity, were integrated into a capacitor circuit for the photocurrent generation when hydrogen peroxide is presented. The capture antibody is immobilized onto the surface of a microplate whereas the detection antibody is conjugate with gold nanoparticles and glucose oxidase. So, the oxidation of glucose produces H_2O_2 which acts as a co-reaction reagent to trigger the chemiluminescence of peroxyoxalate whose light induces a transient current that increases with the target Prostate-specific antigen concentration.[7] The biosensor detects the analyte in the linear range of 10-80 pg mL^{-1} with a LOD of 3 pg mL^{-1}.

PEC biosensors also have been constructed for the detection of different mycotoxins (fungal pathogens) for instance ochratoxin A. Ag/AgCl nanoparticles conjugated with reduced GO were employed as photoactive material which showed superior photocurrent response and stability under visible light irradiation.[8] Reduced GO nanosheets serve as the substrate for in situ growth of Ag/AgCl nanoparticles and improve the charge separation as well as transportation. The photocurrent increased with the concentration of ochratoxin A, and the dynamic range of detection was from 0.05 to 300 nM with a

LOD of 0.01 nM. This PEC biosensor also showed high sensitivity with good intra-assay precision and excellent reproducibility.

Some of the advantages that PEC biosensors possess are the high sensitivity since the majority of proposals found in the literature report LOD from ng mL^{-1} to pg mL^{-1}, diverse electrode surfaces can be used for their development, excellent selectivity, and accuracy. Moreover, most papers highlight the reproducibility of the immunoassay which is fundamental in biosensing applications. However, the principal disadvantages of PEC biosensors include (i) the requirement of multiple reagents and special equipment for their operation, (ii) cumbersome procedures with multiple washing and blocking steps, and (iii) photocorrosion can hinder analyte detection. Table 2-1 resumes some characteristics of PEC biosensors found in the literature.

2.2 Photoluminescence quenching-based biosensors

These type of biosensors are based on the FRET phenomenon and occurs when the emission spectrum of a fluorophore, known as the donor, overlaps with the absorption spectrum of another molecule, known as the acceptor.[10] Thus, the donor, electronically excited, can transfer its absorption energy to the acceptor in a non-radiative way by long-range dipole-dipole interactions. Thus, when biorecognition occurs (such as the antibody-analyte association), changes in the photoluminescence intensity are produced which might act as an indicator that reveals such biorecognition. The FRET phenomenon is described in detail in section 1.2.3. Photoluminescence quenching-based biosensors are easy to use, low cost, and offer excellent selectivity regarding analyte detection in real samples.[11] Some applications performed under this approach include the detection of biomarkers for bacterial infections,[12] food allergens,[13] viruses,[14]and also has been used for the determination of microRNA[15] and immunoglobulins such as IgG.[16] Fluorescence nowadays is one of the methods more used in the biosensing area due to the high sensitivity that offers.[11]

A fluorescence biosensor was constructed for the detection of methicillin-resistant Staphylococcus aureus (MRSA). This bacterial strain is responsible for diverse diseases including skin infection, food poisoning, gastroenteritis, and pneumonia.[17] Carboxyfluorescein-labeled single-stranded DNA was used as a capture and signal probe. Then, this capture and signal probe was adsorbed onto the GO surface via π- π stacking interactions which resulted in the fluorescence quenching of the probe. So, when the analyte is introduced, the fluorescence is restored since the probe is completely released from the GO surface. This biosensing proposal showed a linear range from 1 to 40 nmol L^{-1} with a LOD of 0.5 nmol L^{-1}. Moreover, the authors reported that the biosensor exhibits high sensitivity and selectivity with potential clinical detection of drug-resistant strains.

Food allergies have become a public health concern in food safety due to their significant effect on people's morbidity and the cost of medical treatments.[13] A microfluidic biosensor based on the quenching and recovery of fluorescence was developed for the detection of Ara h 1 (is a seed storage protein from *Arachis hypogaea*) allergen. QDs-aptamer functionalized GO is used as a biosensing probe, and in absence of the analyte the fluorescence provided by QDs is quenched, and so, when the analyte is added such fluorescence is recovered since QDs-aptamer conjugates are desorbed from the GO sur-

Table 2-1. Summary of the revised graphene-based PEC biosensors.

Graphene type	Advantages	Disadvantages	Analyte detected	LOD	Ref
Reduced GO	High sensitivity and reliability.	Multiple washing and blocking steps. Several reagents for its operation.	Procalcitonin	0.15 pg mL^{-1}	6
Reduced GO	Multiple electrode surfaces Can be used. Excellent accuracy and selectivity.	Multiple reagents for its operation. Multiple cumbersome procedures.	Ochratoxin A, aflatoxin B1 and zearalenone.	0.59, 0.17,and 0.6 pg mL^{-1}, respectively.	9
Reduced GO	Excellent selectivity, acceptable reproducibility, and stability.	Multiple washing and blocking steps. Analyte immobilization.	Alpha-fetoprotein.	1 pg mL^{-1}	4
Reduced GO	High sensitivity, good reproducibility, and satisfactory accuracy.	Multiple washing and blocking steps. Multiple reagents for its operation.	Ochratoxin A.	4 pg mL^{-1}	8
GO	High sensitivity and selectivity. Excellent stability and satisfactory reproducibility.	Immobilization of the antibody. Multiple washing and blocking steps. Multiple reagents for its operation.	Amino-terminal pro-B-type natriuretic peptide.	0.03 pg mL^{-1}	5
Reduced GO	Good reproducibility, precision, and high specificity.	Multiple reagents for its operation. Multiple washing and blocking steps. Multiple cumbersome procedures.	Prostate-specific antigen	3 pg mL^{-1}	7
Reduced GO	High detection sensitivity and good reliability.	Multiple reagents for its operation. Multiple washing and blocking steps.	Alpha-fetoprotein.	0.05 ng mL^{-1}	3
GO	High selectivity, reproducibility, and specificity in real samples.	Multiple washing and blocking steps. Multiple cumbersome procedures.	Microcystin-LR	0.011 pM	2

face. The linear range for Ara h 1 detection goes from 200 to 2000 ng mL^{-1} with a LOD of 56 ng mL^{-1}. This biosensor has the potential for on-site determination for rapidly detecting food allergens with high selectivity and sensitivity.

A fluorescence-based biosensor was fabricated for the detection of ferritin (is the principal protein that storages, transports and releases iron in a controlled manner) which is a biomarker that brings information about anemia and oxidative stress.[18] Amine-functionalized graphene-QDs conjugated with anti-ferritin antibodies were the biosensing probe in this method. Apart from the excellent photoluminescence quenching capacity of Graphene-based materials, they also have the ability to adsorb some molecules such as proteins and nucleic acids via π-stacking interactions or chemical coupling. Thus, Graphene facilitates the immobilization of antibodies on its surface. The graphene-QDs fluorescence is quenched by methyl orange, and the fluorescence is recovered when the analyte is added. The biosensor showed a linear range for ferritin detection from 10 to 4000 ng mL^{-1} with a LOD of 0.723 ng mL^{-1} and an R^2 of 0.994. The biosensor response was recorded in both standards as well as human serum samples.

Another interesting fluorescence-based biosensor was constructed for the detection of microRNA let-7a.[15] Carbon dots were conjugated to the end of a single-stranded fuel DNA and afterward were absorbed onto the surface of GO through π-π stacking interactions, which results in the quenching of fluorescence. When the analyte is added, the complex carbon dots-fuel DNA was desorbed from the GO surface, and so the fluorescence was restored due to two successive toehold-mediated strand displacement reactions on double-stranded DNA-modified gold nanoparticles.[15] The linear range for the detection of target DNA goes from 0.01 to 1 nM with a LOD of 7.8 pM. The principal advantages of the biosensor proposed were the signal amplification strategy, excellent sensitivity for analyte detection, and GO increases the biocompatibility since can adsorb multiple antibodies onto its surface.

Campylobacter jejuni is the pathogen responsible for severe gastroenteritis, a bacterial infection known as campylobacteriosis.[12] A fluorescence-based biosensor was constructed for the detection of Campylobacter jejuni in which the biosensing probe consists of polyclonal antibodies conjugated with graphene QDs, and such probe interacts with GO. In absence of bacteria cells, the fluorescence remains off due to π-π stacking interactions between graphene QDs and the GO quencher. But when bacteria cells are present, the specific binding of them with antibodies-labeled graphene QDs leads to generating a distance between graphene QDs and GO, and as a consequence, the fluorescence is recovered. The linear range for bacterial detection goes from 10 to 10^6 CFU mL^{-1} with a LOD of 10 CFU mL^{-1}.

To sum up, fluorescence quenching-based biosensors bring some advantages such as high sensitivity, good specificity regarding analyte detection in standard and real samples, simple operation, fast response, and multiple analyses. Moreover, in general not require secondary recognition antibodies for their development. However, the principal disadvantages include multiple washing and separation steps and require special instrumentation for their construction. Table 2-2 summarizes some characteristics of fluorescence-based biosensors found in the literature.

Table 2-2. Highlights for every photoluminescence quenching-based biosensor.

Graphene type	Advantages	Disadvantages	Analyte detected	LOD	Ref
GO	Retained stability/ sensitivity toward NS1 without impact from interferents.	Antibody immobilization. Involves cumbersome procedures.	Non-structural 1 protein.	0.48 ng mL^{-1}	14
GO	High selectivity and sensitivity, and the ability to perform at the minimum time.	Involves cumbersome procedures. Multiple washing steps.	Campylobacter jejuni.	10 CFU mL^{-1}	12
GO	One-step 'turn on' homogenous assay. High sensitivity and selectivity. Not complicated probe immobilization or tedious procedures.	Multiple washing and blocking steps.	Peanut allergen Ara h1.	56 ng mL^{-1}	13
GO	High sensitivity and good specificity.	This biosensing system requires multiple reagents for its operation.	Ferritin.	0.723 ng mL^{-1}	18
GO	Not require secondary recognition antibodies.	Multiple washing steps.	IgG	4.67 pmol mL^{-1}	16
GO	The excellent fluorescence quenching ability of GO significantly reduced the background signal for improved sensitivity.	Multiple reagents for its operation. The biosensing system requires washing and blocking steps.	Micro-RNA	7.8 pM	15
GO	High sensitivity and good specificity.	Multiple reagents for its operation. Multiple cumbersome procedures.	Matrix metallo-proteinases 2	40 ng mL^{-1}	19
GO	Rapid, sensitive, and selective fluorescent biosensor.	Multiple washing and blocking steps.	Methicillin-resistant *Staphylococcus aureus*	0.5 nM	17

2.3 Surface Plasmon Resonance (SPR)-based biosensors

Surface plasmons are electromagnetic waves that propagate throughout an interface between the conductor and dielectric materials.[11] in general, the excitation of surface plasmons is not made directly. The method used for the generation of surface plasmons is known as Kretschmann attenuated total reflectance. This configuration consists of a slide that is decorated with a thin metal film, generally gold or silver nanoparticles. Thus, a biorecognition element can be immobilized onto the metal film surface.[11] The slide is now coupled to a prism through an index-matching fluid or a polymer layer. Then, a polarized laser beam is directed at the prism and the light that is reflected (over metal film) is collected in a detector. So, reflectivity changes concerning the angle or the wavelength provide a signal. When the biorecognition element immobilized binds with the analyte a further shift of the SPR coupling angle occurs.[11] This method is used in the immunosensing of diverse analytes. SPR-based biosensors are widely used in clinical diagnostics, environmental monitoring, and food quality due to the real-time monitoring and the good sensitivity that offer. Moreover, is a label-free technique.

Immunoglobulin G (IgG) is a protein that has been under constant study due to its usefulness as a potential biomarker in diseases such as Parkinson's,[20] or multiple sclerosis[21] due to its important role in the immunocompetence process, so optimal detection of this molecule is pivotal for clinical treatments. A dual-channel fiber-optics SPR-based biosensor was constructed for the detection of Human-IgG in which one sensing channel is coated with a bilayer of GO and Au.[22] Then, Goat anti-Human-IgG is immobilized onto GO/Au bilayer surface. The GO contributes to improving the loading of biomolecules and the immunological response. Human-IgG is labeled with Au nanoparticles which act as an amplification tag to enhance the SPR sensing response. The second sensing channel is coated with a layer of Ag acting as a reference channel to eliminate measurement errors caused by non-specific binding and cross-sensitivity. The biosensor has a high refractive index sensitivity with 13.592 nm/RIU and a LOD of 15 nm mL^{-1}.

Other fiber-optics SPR-based biosensor was constructed for the detection of Human-IgG.[23] First, a gold layer was fixed onto the sensor surface and then a layer of GO was coated onto the gold film surface. The abundant functional groups and large surface area facilitate that GO can adsorb more antibodies onto its surface. The gold/GO layer is modified with staphylococcal protein A to improve the sensitivity of the biosensor. the linear range of the biosensor for Human-IgG detection goes from 30 to 100 µg mL^{-1} with a LOD of 0.5 µg mL^{-1}. The principal advantages of this biosensor include easy fabrication, high sensitivity, label-free, and rapid response.

Others fiber-optics SPR-based biosensors were constructed for the detection of IgG.[24,25] In the first, gold nanoparticles are deposited onto the sensing zone (the unclad portion), and afterward, a layer of GO is also deposited. This gold nanoparticles/GO composite is employed as the signal amplification element. Again, due to the abundant carboxylic groups present in the GO surface, more anti-IgG can be immobilized. So, antibodies are immobilized and the biosensor is ready to detect the analyte (IgG). The linear range of the biosensor for IgG detection goes from 0.1 to 1000 ng mL^{-1} with a LOD of 0.038 ng mL^{-1}. A sandwich-type biosensor where GO is also used to immobilize the antibody for the detection of IgG was designed.[25] The LOD obtained was 1.88 ng mL^{-1}, which is

260-fold lower than obtained by routine SPR biosensor with a sandwich-type assay.

An SPR-based biosensor was developed for the immunoassay of pregnancy-associated plasma protein A2 (PAPPA2) in human plasma.[26] The carboxyl-GO composite is used to modulate and enhance the work function, conductivity properties, and plasmon electric field for liquid interfaces. Moreover, the carboxyl groups contributed to improving the electron transfer between the gold electrode and carboxyl-GO. So, the electric field can be enhanced due to electron transfer. PAPPA2 analyte was detected in the linear range of 0.1 pg mL^{-1} to 10 ng mL^{-1} with a LOD of 0.1 pg mL^{-1}. The biosensor has high sensitivity and affinity which is demonstrated by the high association rate constant obtained 3.1 x10^9 $M^{-1}s^{-1}$. This biosensing proposal has the advantage of improving the SPR sensitivity without the need for amplification steps. For the detection of human cardiac myoglobin in serum samples was constructed a microfluidic SPR-based biosensor in which a gold film is modified with L-cysteine-graphene hydrogel. Then, specific cardiac myoglobin antibodies are in-situ functionalized onto the L-cysteine-graphene surface via EDC-NHS chemistry.[27] The biosensor can detect the analyte in serum samples in the linear range of 0.01-1000 ng mL^{-1} with a LOD of 10 pg mL^{-1}. Also, it has high sensitivity and good affinity which is demonstrated by association and dissociation rate constants obtained 4.93 $\pm$ 0.2 x10^5 $M^{-1}s^{-1}$ and 1.37 $\pm$ 0.08 x10^{-4} s^{-1}, respectively. Finally, the intra-assay precision calculated was 8 % for standard samples and 9 % for real serum samples.

The SPR-based biosensors have the advantages of being a label-free technique, the biodetection can be monitored in real-time, high detection sensitivity, small sample size requirement, sensor chips can be reused, and biomolecular binding interaction can be determined by this technique. Despite these advantages, the principal limitations of SPR technology include the immobilization of antibodies requiring special orientation for biodetection, non-specific binding events can occur, SPR instrumentation and chips are in general expensive, and limitation of mass transportation. On the other hand, GO has extraordinary physical and chemical properties such as high electrical conductivity, excellent specific surface area, and stability.[28,29] Moreover, the biocompatibility characteristic of GO is due to the presence of oxygen functional groups that facilitate the adsorption of molecules such as DNA, glucose, amino acids, and antibodies onto its surface through π-π stacking, hydrophobic interaction, and hydrogen bonding.[30]

2.4 References

1. Devadoss, A.; Sudhagar, P.; Terashima, C.; Nakata, K.; Fujishima, A. Photoelectrochemical Biosensors: New Insights into Promising Photoelectrodes and Signal Amplification Strategies. Journal of Photochemistry and Photobiology C: Photochemistry Reviews 2015, 24, 43–63. https://doi.org/10.1016/j.jphotochemrev.2015.06.002.

2. Fan, L.; Xiao, G.; Wang, M.; Zhao, S.; Yang, Q.; Cheng, L.; Huang, J. J.; Yue, Z. Ultrasensitive Photoelectrochemical Microcystin-LR Immunosensor Using Carboxyl-Functionalized Graphene Oxide Enhanced Gold Nanoclusters for Signal Amplification. Analytica Chimica Acta 2021, 1185, 339078. https://doi.org/10.1016/j.aca.2021.339078.

3. Wu, Y.; Su, H.; Yang, J.; Wang, Z.; Li, D.; Sun, H.; Guo, X.; Yin, S. Photoelec-

Table 2-3. Highlights for SPR-based biosensors.

Graphene type	Advantages	Disadvantages	Analyte detected	LOD	Ref
GO	Excellent sensitivity and selectivity.	Multiple washing and blocking steps. Multiple cumbersome procedures. Multiple reagents for its operation.	H-IgG	1.88 ng mL^{-1}	25
GO	A label-free immunoassay without amplification steps to enhance SPR sensitivity.	Multiple washing and blocking steps. Multiple cumbersome procedures.	Pregnancy-associated plasma protein A2.	0.01 pg mL^{-1}	26
Graphene	Real-time monitoring and label-free approach. High sensitivity and good specificity.	Multiple cumbersome procedures. Multiple washing and blocking steps.	Human cardiac myoglobin.	10 pg mL^{-1}	27
GO	Small size, ease of fabrication, high sensitivity, label-free, and rapid response.	Antibody immobilization. Multiple washing and blocking steps. Multiple cumbersome procedures.	H-IgG	0.5 µg mL^{-1}	23
GO	Label-free detection. High sensitivity and good specificity.	Multiple washing and blocking steps. Antibody immobilization.	Pig-IgG	37.5 ng mL^{-1}	31
GO	High sensitivity, accuracy, and temperature insensitive.	Multiple cumbersome procedures. Antibody immobilization. Multiple reagents for its operation.	H-IgG	15 ng mL^{-1}	22
GO	Satisfactory immunological specificity in human blood. No need for nanoparticle-induced signal amplification. Label-free, real-time monitoring, and sensitive immunoassay.	Antibody immobilization. Multiple washing and blocking steps.	D-dimer	5.08 ng mL^{-1}	32
GO	Good reproducibility, high sensitivity, and real-time monitoring.	Antibody immobilization. Multiple reagents for its operation.	IgG	0.038 ng mL^{-1}	24

trochemical Immunosensor for Sensitive Detection of Alpha-Fetoprotein Based on a Graphene Honeycomb Film. Journal of Colloid and Interface Science 2020, 580, 583–591. https://doi.org/10.1016/j.jcis.2020.07.064.

4. Yan, H.; Gong, L.; Zang, L.; Dai, H.; Xu, G.; Zhang, S.; Lin, Y. Dual-Responsive Competitive Immunosensor for Sensitive Detection of Tumor Marker on g-CN/RGO Conjugation. Sensors and Actuators B: Chemical 2016, 230, 810–817. https://doi.org/10.1016/j.snb.2016.02.144.

5. Qian, Y.; Feng, J.; Fan, D.; Zhang, Y.; Kuang, X.; Wang, H.; Wei, Q.; Ju, H. A Sandwich-Type Photoelectrochemical Immunosensor for NT-pro BNP Detection Based on F-Bi2WO6/Ag2S and GO/PDA for Signal Amplification. Biosensors and Bioelectronics 2019, 131, 299–306. https://doi.org/10.1016/j.bios.2019.02.029.

6. Abbas, Z.; Soomro, R. A.; Kalwar, N. H.; Tunesi, M.; Willander, M.; Karakuş, S.; Kilislioğlu, A. In Situ Growth of CuWO4 Nanospheres over Graphene Oxide for Photoelectrochemical (PEC) Immunosensing of Clinical Biomarker. Sensors 2020, 20 (1). https://doi.org/10.3390/s20010148.

7. Shu, J.; Qiu, Z.; Zhou, Q.; Lin, Y.; Lu, M.; Tang, D. Enzymatic Oxydate-Triggered Self-Illuminated Photoelectrochemical Sensing Platform for Portable Immunoassay Using Digital Multimeter. Anal. Chem. 2016, 88 (5), 2958–2966. https://doi.org/10.1021/acs.analchem.6b00262.

8. Tang, J.; Xiong, P.; Cheng, Y.; Chen, Y.; Peng, S.; Zhu, Z.-Q. Enzymatic Oxydate-Triggered AgNPs Etching: A Novel Signal-on Photoelectrochemical Immunosensing Platform Based on Ag@AgCl Nanocubes Loaded RGO Plasmonic Heterostructure. Biosensors and Bioelectronics 2019, 130, 125–131. https://doi.org/10.1016/j.bios.2019.01.014.

9. Qileng, A.; Huang, S.; He, L.; Qin, W.; Liu, W.; Xu, Z.; Liu, Y. Composite Films of CdS Nanoparticles, MoS2 Nanoflakes, Reduced Graphene Oxide, and Carbon Nanotubes for Ratiometric and Modular Immunosensing-Based Detection of Toxins in Cereals. ACS Appl. Nano Mater. 2020, 3 (3), 2822–2829. https://doi.org/10.1021/acsanm.0c00126.

10. Introduction to Fluorescence. In Principles of Fluorescence Spectroscopy; Lakowicz, J. R., Ed.; Springer US: Boston, MA, 2006; pp 1–26. https://doi.org/10.1007/978-0-387-46312-4_1.

11. Paras, P. Optical Biosensors. In Introduction to Biophotonics; John Wiley & Sons, Ltd, 2003; pp 311–356. https://doi.org/10.1002/0471465380.ch9.

12. Dehghani, Z.; Mohammadnejad, J.; Hosseini, M.; bakhshi, B.; Rezayan, A. H. Whole Cell FRET Immunosensor Based on Graphene Oxide and Graphene Dot for Campylobacter Jejuni Detection. Food Chemistry 2020, 309, 125690. https://doi.org/10.1016/j.foodchem.2019.125690.

13. Weng, X.; Neethirajan, S. A Microfluidic Biosensor Using Graphene Oxide and Aptamer-Functionalized Quantum Dots for Peanut Allergen Detection. Biosensors

and Bioelectronics 2016, 85, 649–656. https://doi.org/10.1016/j.bios.2016.05.072.

14. Kanagavalli, P.; Veerapandian, M. Opto-Electrochemical Functionality of Ru(II)-Reinforced Graphene Oxide Nanosheets for Immunosensing of Dengue Virus Non-Structural 1 Protein. Biosensors and Bioelectronics 2020, 150, 111878. https://doi.org/10.1016/j.bios.2019.111878.

15. Gao, Y.; Yu, H.; Tian, J.; Xiao, B. Nonenzymatic DNA-Based Fluorescence Biosensor Combining Carbon Dots and Graphene Oxide with Target-Induced DNA Strand Displacement for MicroRNA Detection. Nanomaterials 2021, 11 (10). https://doi.org/10.3390/nano11102608.

16. Huang, A.; Li, W.; Shi, S.; Yao, T. Quantitative Fluorescence Quenching on Antibody-Conjugated Graphene Oxide as a Platform for Protein Sensing. Scientific Reports 2017, 7 (1), 40772. https://doi.org/10.1038/srep40772.

17. Ning, Y.; Gao, Q.; Zhang, X.; Wei, K.; Chen, L. A Graphene Oxide–Based Sensing Platform for the Determination of Methicillin-Resistant Staphylococcus Aureus Based on Strand-Displacement Polymerization Recycling and Synchronous Fluorescent Signal Amplification. SLAS Discovery 2016, 21 (8), 851–857. https://doi.org/10.1177/1087057116653564.

18. Garg, M.; Vishwakarma, N.; Sharma, A. L.; Singh, S. Amine-Functionalized Graphene Quantum Dots for Fluorescence-Based Immunosensing of Ferritin. ACS Appl. Nano Mater. 2021, 4 (7), 7416–7425. https://doi.org/10.1021/acsanm.1c01398.

19. Yang, J.-K.; Hwang, I.-J.; Jeon, S.-J.; Ju, J.-M.; Kim, H.-I.; Yim, D.; Lee, Y.-S.; Kim, J.-H. Atomically-Tailored Graphene Oxide Displaying Enhanced Fluorescence for the Improved Optical Sensing of MMP-2. Sensors and Actuators B: Chemical 2019, 284, 485–493. https://doi.org/10.1016/j.snb.2018.12.100.

20. Russell, A. C.; Šimurina, M.; Garcia, M. T.; Novokmet, M.; Wang, Y.; Rudan, I.; Campbell, H.; Lauc, G.; Thomas, M. G.; Wang, W. The N-Glycosylation of Immunoglobulin G as a Novel Biomarker of Parkinson's Disease. Glycobiology 2017, 27 (5), 501–510. https://doi.org/10.1093/glycob/cwx022.

21. Talaat, F.; Ramadan, I.; Hamdy, E.; Sayed, A.; Elfatatry, A. M. Immunoglobulin G Index as a Biomarker of Relapse Response to Corticosteroids during Early Stages of Multiple Sclerosis. Multiple Sclerosis and Related Disorders 2020, 38, 101495. https://doi.org/10.1016/j.msard.2019.101495.

22. Wang, Q.; Wang, X.-Z.; Song, H.; Zhao, W.-M.; Jing, J.-Y. A Dual Channel Self-Compensation Optical Fiber Biosensor Based on Coupling of Surface Plasmon Polariton. Optics & Laser Technology 2020, 124, 106002. https://doi.org/10.1016/j.optlastec.2019.106002.

23. Q. Wang; J. -Y. Jing; B. -T. Wang. Highly Sensitive SPR Biosensor Based on Graphene Oxide and Staphylococcal Protein A Co-Modified TFBG for Human IgG Detection. IEEE Transactions on Instrumentation and Measurement 2019, 68 (9), 3350–3357. https://doi.org/10.1109/TIM.2018.2875961.

24. Chen, C.-H.; Chiang, C.-Y.; Wu, C.-W.; Wang, C.-T.; Chau, L.-K. Integrated Graphene Oxide with Noble Metal Nanoparticles to Develop High-Sensitivity Fiber Optic Particle Plasmon Resonance (FOPPR) Biosensor for Biomolecules Determination. Nanomaterials 2021, 11 (3). https://doi.org/10.3390/nano11030635.

25. Wu, Q.; Sun, Y.; Zhang, D.; Li, S.; Wang, X.; Song, D. Magnetic Field-Assisted SPR Biosensor Based on Carboxyl-Functionalized Graphene Oxide Sensing Film and Fe3O4-Hollow Gold Nanohybrids Probe. Biosensors and Bioelectronics 2016, 86, 95–101. https://doi.org/10.1016/j.bios.2016.06.035.

26. Chiu, N. F.; Tai, M. J.; Wu, H. P.; Lin, T. L.; Chen, C. Y. Development of a Bioaffinity SPR Immunosensor Based on Functionalized Graphene Oxide for the Detection of Pregnancy-Associated Plasma Protein A2 in Human Plasma. August 22, 2019, p 6735—6748.

27. Singh, N.; Ali, Md. A.; Rai, P.; Ghori, I.; Sharma, A.; Malhotra, B. D.; John, R. Dual-Modality Microfluidic Biosensor Based on Nanoengineered Mesoporous Graphene Hydrogels. Lab Chip 2020, 20 (4), 760–777. https://doi.org/10.1039/C9LC00751B.

28. Dimiev, A. M. Mechanism of Formation and Chemical Structure of Graphene Oxide. In Graphene Oxide; John Wiley & Sons, Ltd, 2016; pp 36–84. https://doi.org/10.1002/9781119069447.ch2.

29. Morales-Narváez, E.; Merkoçi, A. Graphene Oxide as an Optical Biosensing Platform: A Progress Report. Advanced Materials 2019, 31 (6), 1805043. https://doi.org/10.1002/adma.201805043.

30. Sharma, D.; Kanchi, S.; Sabela, M. I.; Bisetty, K. Insight into the Biosensing of Graphene Oxide: Present and Future Prospects. Arabian Journal of Chemistry 2016, 9 (2), 238–261. https://doi.org/10.1016/j.arabjc.2015.07.015.

31. Wu, Q.; Sun, Y.; Ma, P.; Zhang, D.; Li, S.; Wang, X.; Song, D. Gold Nanostar-Enhanced Surface Plasmon Resonance Biosensor Based on Carboxyl-Functionalized Graphene Oxide. Analytica Chimica Acta 2016, 913, 137–144. https://doi.org/10.1016/j.aca.2016.01.063.

32. Wang, J.; Lu, Y.; Zhang, Y.; Ning, Y.; Zhang, G.-J. Graphene Oxide-Assisted Surface Plasmon Resonance Biosensor for Simple and Rapid Determination of D-Dimer in Plasma. Journal of Nanoscience and Nanotechnology 2016, 16 (7), 6878–6883. https://doi.org/10.1166/jnn.2016.11308.

Chapter 3

The immunosensing platform for the detection of H-IgG and PSA

In this chapter is described the immunosensing platform which is based on the photoluminescence quenching capabilities of GO-covered microwell plates. The quenching of fluorescence is consequence of the highly efficient nonradiative energy transfer occurring between GO (acceptor) and photoluminescence fluorophores (donors). We found that fluorescence intensity of fluorophores-labeled antibodies (that is, the biosensing probes) are strongly quenched by GO-coated microwells whereas biosensing probe complex with its respective analyte is weakly quenched by the same surface due to low affinity and relative long distance between the biosensing probe-analyte complexes and GO-covered microwells. This immunosensing platform was used for the detection of Human immunoglobulin G and Prostate specific antigen.

3.1 Introduction

3.1.1 The operational principle of the proposed immunosensing platform

The operational principle of the immunosensing platform is based on the following hypothesis: the more analyte concentration, the less quenching of fluorescence of the biosensing probe (fluorophore-Antibody complex). In contrast, the blank (no analyte) undergoes the maximum quenching of fluorescence, see figure 3-1A. Graphene oxide (GO), which is an excellent quencher of fluorescence, has been observed to exhibit a high affinity with proteins that are not forming immunocomplexes.[1,2] Hence, the fluorescence intensity of F-Ab (fluorophore-labeled protein) (a donor) can be strongly quenched when F-Ab is incubated within GO-covered microwell surfaces (an acceptor) via non-radiative energy transfer (a phenomenon efficiently occurring when the distance between donor and acceptor is below 20 nm).[3] However, the formation of immunocomplexes involves non-covalent intermolecular interactions such as hydrogen bonding, electrostatic interactions, hydrophobic, and Van der Waals forces.[4] We hypothesize that such intermolecular interactions hinder the affinity between immunocomplexes and GO-covered microwell surfaces, and as a consequence, in the proposed biosensing platform, the aforementioned non-radiative energy

transfer is not observable upon immunocomplexes development, as depicted in figure 3-1B. Moreover, the analyte acts as a spacer between F-Ab and the GO-covered microwell surface, hence, upon immunocomplexes formation, the distance between donor and acceptor does not facilitate non-radiative energy transfer. The immunosensing platform proposed is based on 96-well tissue culture treated black plates with clear flat bottom (Costar, catalog number 3603).

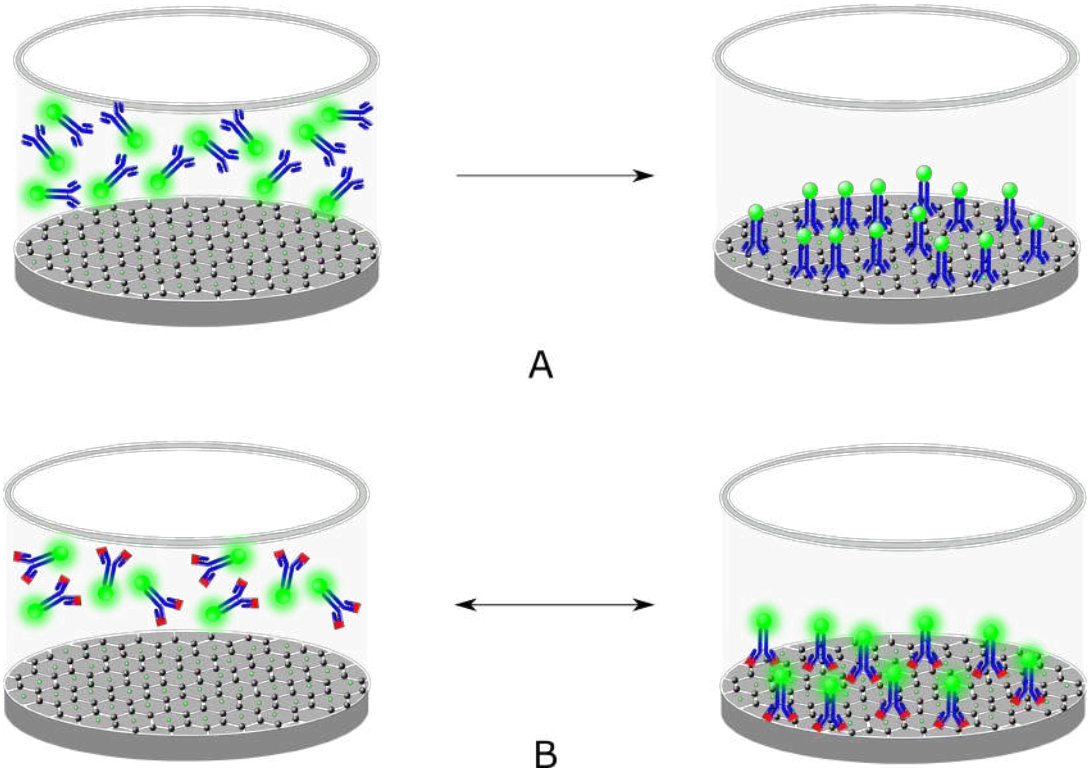

Figure 3-1. The operational principle of the immunosensing platform. **A.** The maximum quenching of fluorescence is reached by the blank. **B.** The quenching of fluorescence is inversely proportional to the analyte concentration.

3.1.2 Clinical relevance of Human immunoglobulin G (H-IgG)

This protein has been under constant study due to its usefulness in the diagnosis of different diseases. For example, metastatic melanoma is a type of skin cancer that is caused by exposure to ultraviolet radiation. Checkpoint Inhibitors is the therapy most used to treat, and improve the survival of metastatic melanoma. However, biomarkers that predict the response to therapy are needed. H-IgG is involved in the immunocompetence process which means the capacity of produced a normal immune response after the exposition to an antigen. As Checkpoint Inhibitors require a functional immune response, H-IgG is capitalized on to correlate with antitumor response, in doing so, H-IgG is used as a predictor of the success of the therapy in patients with metastatic melanoma.[5] Alzheimer's disease is the most common form of dementia which in the last decades has increased around the world. Peptoids are synthetic molecules that can replicate the biological behavior of antigens so they are surrogates that may bind selectively to antibodies raised against antigens which are responsible of trigger the Alzheimer's disease state. Indeed, different methodologies have been developed which used these Peptoids to search for IgG

antibodies that are plentiful in the serum of patients with Alzheimer's disease.[6] H-IgG has also been used as a potential biomarker in diseases such as Parkinson's,[7] or multiple sclerosis[8] due to its important role in the immunocompetence process, so optimal detection of this molecule is pivotal for clinical diagnosis and treatment.

3.1.3 Clinical relevance of Prostate Specific Antigen (PSA

The Prostate Specific Antigen PSA is a glycoprotein that is exclusively synthesized by Prostate cells. Its principal physiological function is dissolving the seminal coagulum (semen). Small quantities of PSA are present in the serum of men with a healthy prostate, and on the contrary, in men with prostate disorders, such PSA levels start to increment. Prostate cancer (PCa) is the principal men's cancer in developed countries (about 15 %) compared with 4 % in developing countries. The factors involved in developing clinical PCa are the pattern of sexual behavior, alcohol consumption, exposure to ultraviolet radiation, and chronic inflammation.[9] Reference values for normal PSA levels in serum differ from laboratory to laboratory but currently, the normal value accepted according to the European Association of Urology is $\leq$ 4 ng mL^{-1}. Thus, the higher the value, the more likely is the existence of PCa. However, elevated levels of PSA in serum not only are associated with PCa but also such increases might be related to other prostate disorders including prostatitis.[10] Some studies have evinced that the treatment of prostatitis decreases the PSA levels in the serum of men with that disorder.[11] The tissue inflammation of the prostate gland is known as prostatitis. It is classified into four categories acute, chronic, asymptomatic inflammatory prostatitis, and chronic pelvic pain syndrome. Benign Prostatic Hyperplasia (BPH) is another prostate disorder that may increase the PSA level in men's serum. BPH is an increase in the size of the prostate gland. Altogether, PSA might be considered a biomarker not only for prostate cancer diagnosis but also for the prognosis of prostatitis or Benign prostatic hyperplasia.

3.2 Experimental section

3.2.1 GO-coated microwells (GOμw) plates

The first step consisted of coating the polystyrene bottom of every microwell with GO. To this end, 100 µL of GO (at a specific concentration that depends on the analyte to be detected) is added per microwell and then, left overnight at gently shaking. In general, every microplate is left for about 15 hours. After that, three washing steps with ultrapure water are made to remove the excess GO that did not adhere to the microwell surface. Figure 3-2B shows a representation of a microwell after washing steps. An important question in this step is Why does GO adhere to every microwell surface of the plate? The answer lies in the composition of the microplates and the chemistry of GO. The surface charge of every microwell is altered by a treatment known as Enhanced Tissue Culture-treated surfaces. This treatment is made by the manufacturer to improve the attachment and growth of fastidious organisms (organisms that only grow when specific nutrients are included in their medium). Particularly in the employed plates (Costar, catalog number 3603), the microwells have a net negative surface charge due to oxygen-containing functional groups (about 9-17 % oxygen atoms) incorporated in the

polystyrene surface.[12] As a consequence, surfaces are more hydrophilic. On the other hand, GO has a negative charge in aqueous solution, the property of hydrophilicity, and also exhibits hydroxyl groups, among other oxygen-containing groups.[13] All in all, GO can attach to the microwell surface via hydrophilic interactions and hydrogen bonding. Figure 3-2A shows the charge configuration of GO and a microwell surface. This figure depicts the GO that adheres to the microwell surface after washing steps.

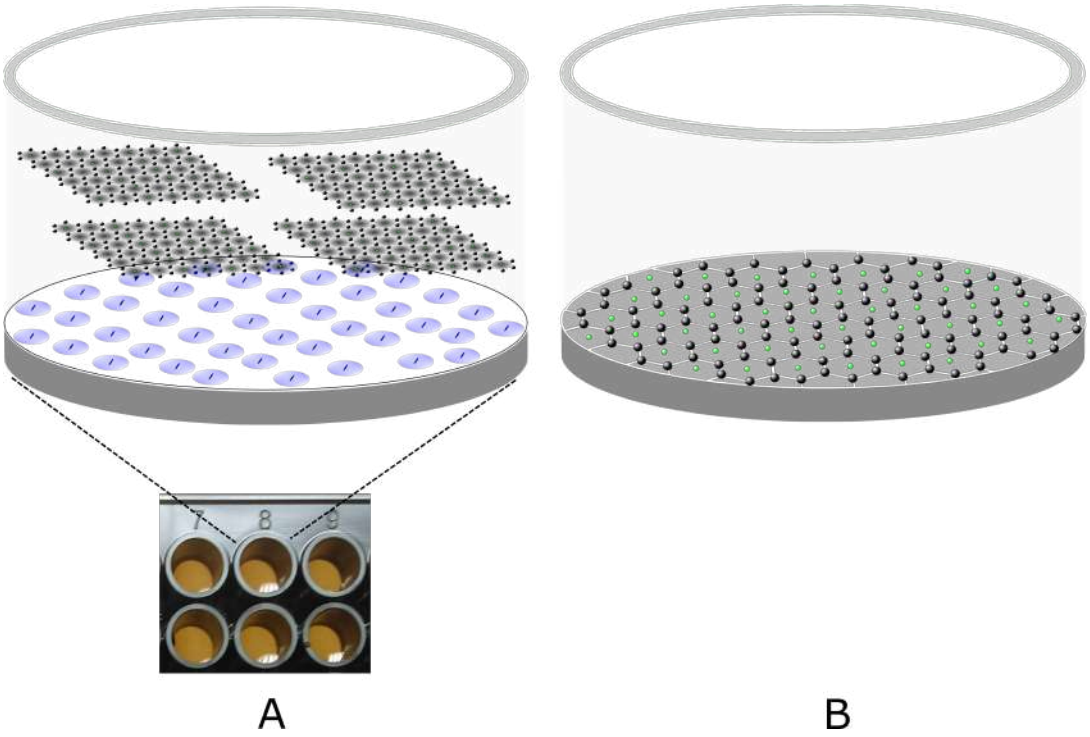

Figure 3-2. Process of GO adhesion to polystyrene surface of a microwell. Black dots depict the carbon atoms and green ones the oxygen atoms conforming hexagonal structure of GO **A.** GO can attach to the microwell surface via hydrophilic interactions and hydrogen bonding. **B.** GO that adheres after washing steps.

3.2.2 Experimental procedure for biodetection

Figure 3-3 depicts the experimental steps to perform the immunoassay. Panel **A** of Figure 3-3 shows a microwell whose surface is covered with GO (GOμW) and then is ready for an immunosensing experiment. Generally, 50-100 μL of the respective analyte to be detected is added in the GOμW, panel **B** of Figure 3-3. Then, 50-100 μL of the immunosensing probe is also added, panel **C**. The liquid is mixed to homogenize. Afterward, the plate is introduced to a microplate reader and the fluorescence intensity is recorded in a kinetic analysis for two hours with readings, in general, every 5 minutes, panel **F**. Usually, seven analyte concentrations and a blank (without analyte) are tested per experiment. The blank has huge importance not only to monitor the overall immunoassay performance, since it reaches the maximum quenching of fluorescence, but also to build the calibration curves, panel **D**. Three replicates per sample are evaluated in every experiment. During the kinetic analysis, the association process starts which means the formation of analyte-biosensing probe immunocomplexes, so the quenching of fluorescence reveals the biorecognition following the operational principle described previously, panel **E**.

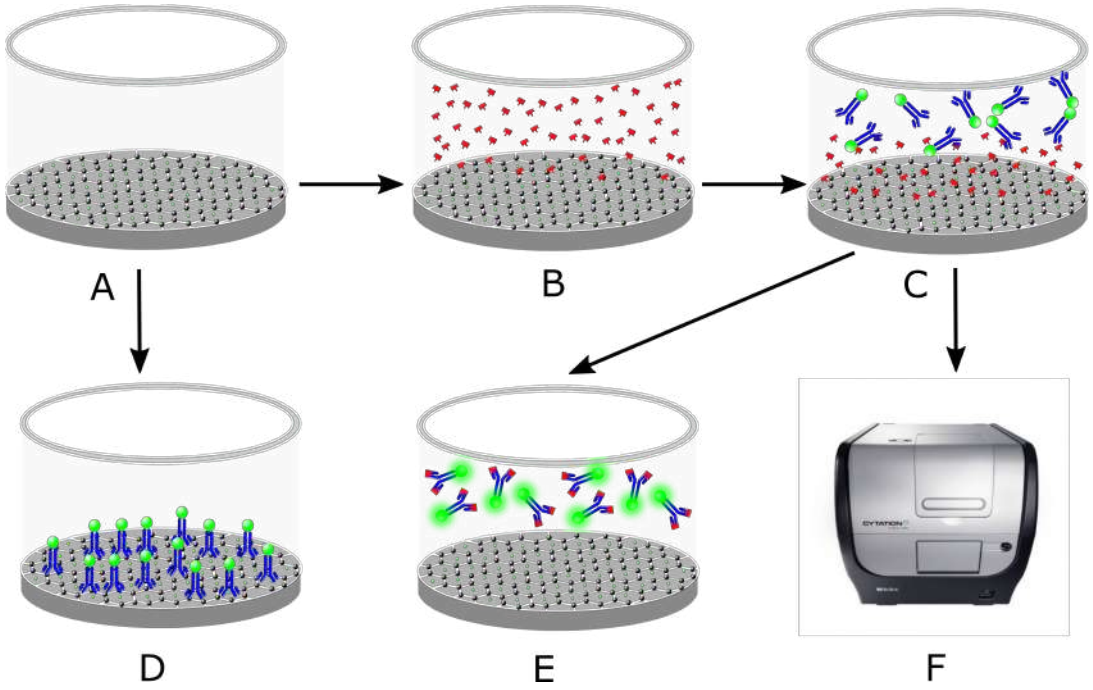

Figure 3-3. Experimental procedure. **A.** GO-coated microwell GOμW. **B.** GOμW with the analyte. **C.** GOμW with the analyte and the immunosensing probe. **D.** GOμW with the blank (no analyte) where the maximum quenching of fluorescence is reached. **E.** Formation of immunocomplexes: the process of association. **F.** microplate reader in which the kinetic analysis is carried out.

3.2.3 Human-IgG and Anti-Human-IgG-FITC: general description

The biosensing probe used for the detection of Human-IgG is Anti-H-IgG-FITC. The specific antibody Anti-H-IgG is conjugated with the fluorophore Fluorescein Isothiocyanate FITC. According to the datasheet provided by the supplier (Abcam, Cambridge, UK), the cross-reactivity with other immunoglobulins or free light chains is less than 0.1 %. The ratio Fluorophore/Antibody (is the average number of fluorophores conjugated by each molecule of antibody) is 5. The standard concentration of this product is 1 mg mL^{-1}. Optimal excitation and emission wavelengths for FITC are 493 nm and 528 nm, respectively. All of this information was important to establish the optimal biosensing probe concentration. Human IgG is one, and the more plentiful, of five immunoglobulins found in the human body. These immunoglobulins are purified from human serum by several techniques. The suppliers established the purity of Human-IgG (Cat No. I2511-10MG) via Immunoelectrophoresis and High-Performance Liquid Chromatography HPLC. So, according to the supplier, the Human-IgG purity is at least 95 %. The standard concentration of this product is 4.87 mg mL^{-1}.

3.2.4 PSA and Anti-PSA: general description

The specific antibody used is Anti-Prostate Specific Antigen [A67-B/E3], which is conjugated with biotin. Following the specifications provided by the supplier (Abcam), the monoclonal antibody is free of unconjugated biotin. The stock concentration of Biotin Anti-PSA is 1 mg mL^{-1}, and its isotype is IgG1. Native Human Prostate Specific Anti-

gen (cat. number ab78528) was also acquired from Abcam which has a purity of 96 %, according to the datasheet furnished by the company. The stock concentration of PSA reactive is 2.6 mg mL^{-1}.

3.2.5 Conjugation of QDs with Anti-PSA

The QDs655 was acquired from TermoFisher Scientific which is conjugated (by covalent bond) with Streptavidin. Following the datasheet, about 5 to 10 streptavidin molecules are contained in each QD nanocrystal. Streptavidin-QDs655 are made from a nanometric semiconductor material (CdSe) covered by a shell of additional semiconductor material (ZnS) which improves the optical properties of Streptavidin-QDs conjugated. The stock concentration of streptavidin-QDs655 is 1µM. On the other hand, it is known that streptavidin has an extraordinary affinity with biotin. Indeed, is one of the strongest non-covalent interactions known in nature.[14] So, conjugation of streptavidin-QDs with Biotin Anti-PSA is possible by those non-covalent interactions. To this end, a streptavidin-QDs655 concentration of 8 nM was mixed with biotin-Anti-PSA at µg mL^{-1} range concentrations. All conjugations were performed with immunobuffer (PBS + 0.5 % PBST + 1 % BSA) and allowing interaction by 45 minutes at a constant agitation rate of 650 rpm. Thus, the biosensing probe for PSA detection is QDs-Anti-PSA. The optimization of this conjugation is described later on.

3.2.6 Indicators employed to evaluate the analytical behavior of the biosensing platform

The limit of detection: is referring to the smallest specific analyte concentration that can be reliably distinguished from the blank sample at whose detection is feasible. LOD is obtained through equation 1-7 and it permits determining the minimum concentration of analyte that can be detected by the immunosensing platform proposed.

Limit of quantification: refers to the minimal analyte concentration detectable with acceptable levels of precision and accuracy under determined assay conditions. In other words, it permits establishing minimal analyte concentration detectable when acceptable values of precision are obtained. LOQ is obtained through equation 1-8.

Dynamic range/Analytical range: it is related to the range of concentrations in which an analyte can be quantified by a determined analytical method.

Slope: it is related to the sensitivity which is the capacity of an analytical method to distinguish little variations of analyte concentrations: the bigger the slope value, the more sensitive the analytical method. So, the slope helps us to establish the interval where the sensitivity is higher.

The coefficient of variation: is related to the precision which is defined as the dispersion obtained from repeated measurements of the same homogeneous sample. So, low values of CV indicate that every analyte concentration tested is detected with high precision. And therefore, the error will be minimal.

Coefficient of determination (R^2): it is a number between 0 and 1 that measures how well a statistical model fits the observed data. So, R^2 indicates if the previous indicators

obtained through the calibration curve are reliable. The closer to one the R2 value, the more precise the fitting.

3.3 Results and discussion

3.3.1 The immunosensing platform targeting Human-IgG

The optimization process for GO and biosensing probe concentrations

H-IgG was the first analyte detected via our immunosensing platform since is a model analyte in immunoassays. Conventional immunoassays are carried out from 2 to 6 hours, so in our first experiment, a kinetic analysis of 5 hours was selected. The next step was establishing the suitable GO concentration with which coated microwells of the plate. In this context, an experiment with three GO concentrations of 800, 1600, and 3200 µg mL^{-1} was carried out. Biosensing probe concentrations selected for the experiment were 0.25, 0.5, and 1 µg mL^{-1}. Graphs in figure 3-4 show the results of this quenching experiment. The natural fluorescence decay of the fluorophore is revealed by the non-GO-coated microwells.

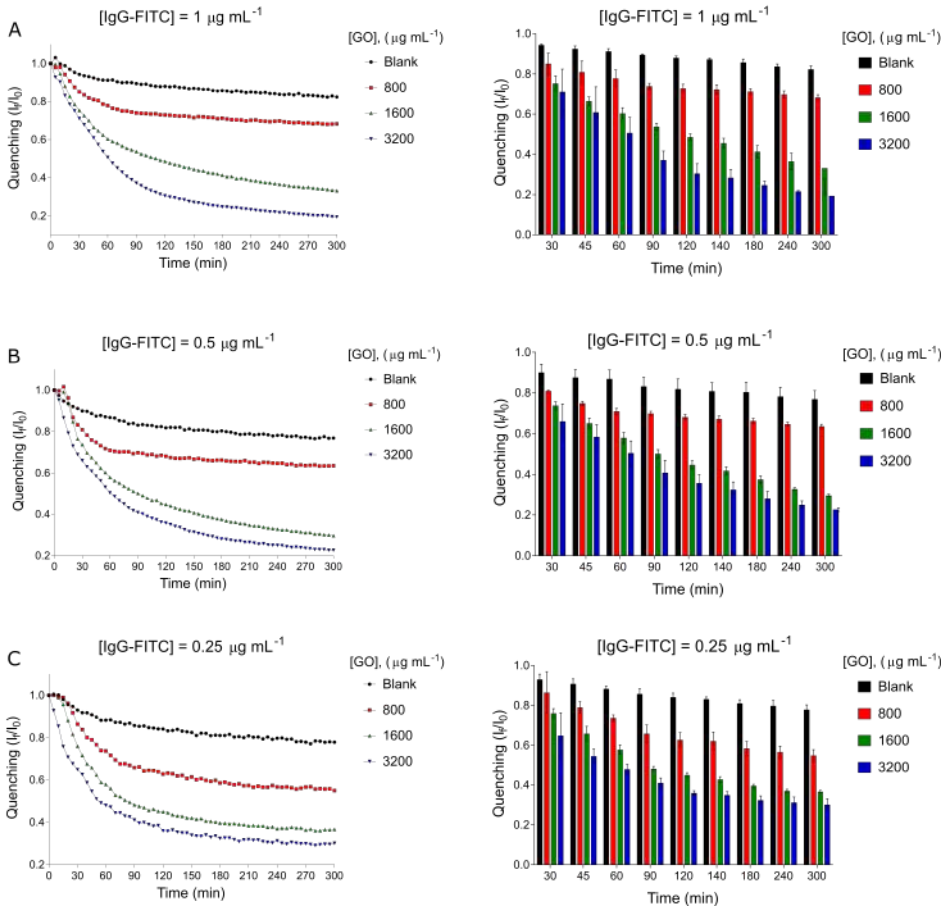

Figure 3-4. Quenching of fluorescence experiments for GO optimization. **A.** Performance to IgG-FITC of 1 µg mL-1. **B.** Performance to IgG-FITC of 0.5 µg mL-1 **C.** Performance to IgG-FITC of 0.25 µg mL-1.

Figure 3-4 shows that after 2 hours (120 minutes) the quenching of fluorescence levels did not change considerably. From this, kinetic analysis for 2 hours is appropriate for every immunoassay. In general, the higher the GO concentration, the bigger the quenching of fluorescence for the explored Biosensing probe concentrations. However, for the biosensing probe concentration of 0.25 µg mL^{-1} quenching of fluorescence reached about 70 % regarding the initial fluorescence intensity value (I_0). Although the microplate reader gives fluorescence intensity in Relative Fluorescence Units RFU, we normalize such intensities of fluorescence at a given time I_F with respect to the initial value I_0 just as shown in figure 3-4. So, from this experiment, we conclude that (i) kinetic analysis of 2 hours is appropriate for every immunoassay, (ii) biosensing probe concentration of 0.25 µg mL^{-1} is suitable for optimal quenching of fluorescence, and (iii) the optimal GO concentration to cover every microwell plate is 1600 µg mL^{-1} since efficiently quench the fluorescence intensity provided by biosensing probe concentration of 0.25 µg mL^{-1}.

Analytical range for the detection for H-IgG

The next step is determining the analytical range for the detection of H-IgG. To this end, an immunoassay with different H-IgG concentrations (from 15 to 960 ng mL^{-1}) and the blank was made to analyze if this range of concentration is detectable following the operational principle of detection, see Figure 3-5A. It was chosen relatively high and low analyte concentrations that allow us to determine the optimal range for H-IgG detection. The two highest H-IgG concentrations (480 and 960 ng mL^{-1}) had a peculiar performance since during the first 30 minutes there was an increase in fluorescence intensity. This might be associated with the homogeneity of the liquid considering that the analyte is added first and then the biosensing probe. To determine if this was the reason for this behavior, another experiment was carried out in which a shaking parameter was added. The microplate reader has the option of shaking the plate so this was selected to improve the homogeneity in every microwell. Orbital shake mode at a velocity of 355 cpm was included in the kinetic analysis. Figure 3-5B depicts kinetic behavior for this immunoassay. In effect, the shaking parameter helps to improve the homogeneity and so the curve for every concentration shows the behavior expected.

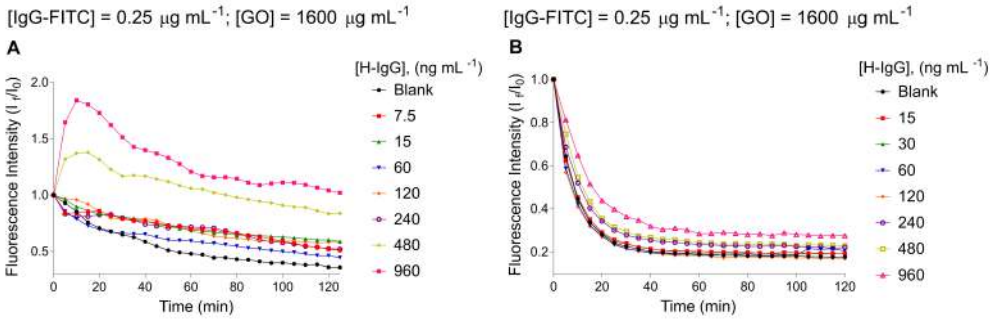

Figure 3-5. **A.** kinetic curves for the determination of the optimal range of detection for H-IgG. **B.** Shaking parameter helps to improve the homogeneity of the immunoassay.

Regarding H-IgG detection, just for the three highest concentrations (960, 480, and 240 ng mL^{-1}), there is an interaction between the analyte and the biosensing probe which is evident following the operational principle of detection, see section 3.1.1. In other words, these three concentrations are separated from the blank. So, it is necessary

to find the conditions that allow for the detection of low concentrations because this is crucial in diagnostics, where generally it is mandatory to obtain low limits of detection for early disease detection. With this in mind, a series of experiments where diverse conditions were tested allowed us to determine that (i) the optimal concentration of the biosensing probe is 0.125 µg mL^{-1} since can detect high and low concentrations of the analyte, (iii) the H-IgG range that is detectable for the immunosensing platform is 9.37-600 ng mL^{-1}. Figure 3-6 shows the optimal conditions for H-IgG detection with the immunosensing platform. So, H-IgG can be detected by the immunosensing platform following the operational principle of detection: the higher the analyte concentration, the lower the respective quenching of fluorescence, see Figure 3-6A. The graph of bars depicted in figure 3-6B let us observe the relationship between concentrations at various times to determine the optimal time detection by calibration curves. Therefore, optimal conditions of the biosensing platform for H-IgG detection are shown in Figure 3-6.

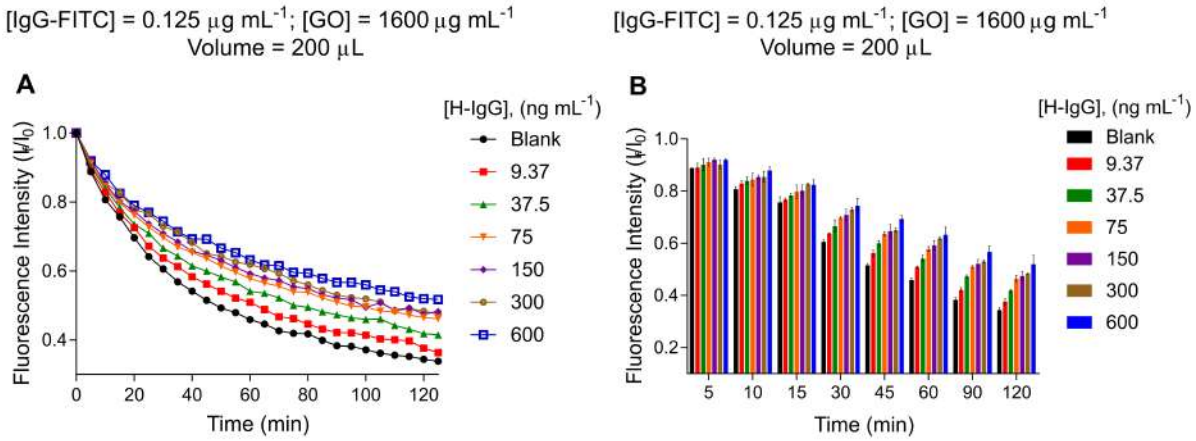

Figure 3-6. Analytical performance of immunosensing platform with optimal conditions for H-IgG detection. **A.** Real-time kinetic analysis of different concentrations of H-IgG and the blank, **B.** Relation between concentrations at several intervals to determine the best sensitivity.

Limit of detection and quantification

The first step to obtaining the LOD and LOQ is to construct the calibration curves graph from bars graph 2-6B. It is important to clarify that the complete analysis of validation was conducted for the experiment showed in figure 3-6 that is where H-IgG was detected with high sensitivity, in accordance with the operational principle of biodetection. A calibration curve relates the signal response (the intensity of fluorescence) with every concentration of the analyte at specific times. Before applying the linear regression to the data, a logarithmic transformation was carried out (to the analyte concentrations in the x-axis). Then, linear regression is applied to the data obtaining the curves shown in the Figure 3-7. To determine the goodness of fitting, coefficients of determination were established from the equation 1-6, whose values are shown in table 3-1.

Table 3-1. Values of coefficients of determination obtained for each fitting curve (for H-IgG detection).

Time (min)	**5**	**10**	**15**	**30**	**45**	**60**	**90**	**120**
$\mathbf{R^2}$	0.7046	0.9414	0.9207	0.9755	0.9752	0.9869	0.9731	0.9579

As seen in Table 3-1, R^2 values for 30, 45, 60, and 90 minutes are closer to 1 (when compared with the other R^2 values), which suggests that the linear fitting adjusts properly to the data. Thus, linear parameters such as the slope m and the intersection with y-axis b can be determined from equations 1-1 and 1-2. Also, uncertainties can be calculated following equations 1-3 and 1-4. Table 3-2 shows values obtained for these parameters. With these results, it can be determined the LOD and LOQ.

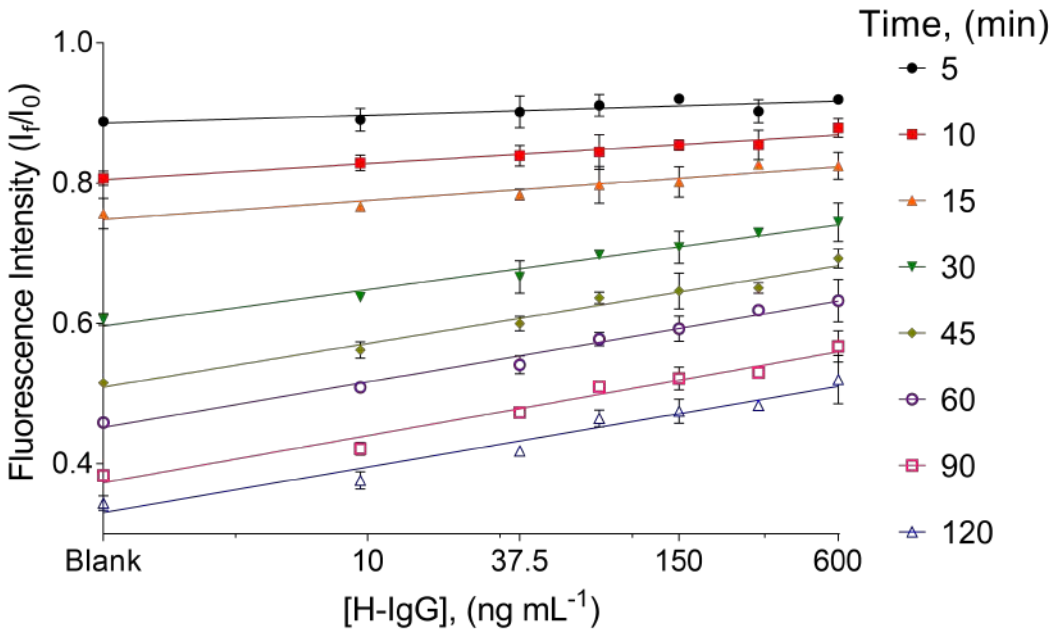

Figure 3-7. Calibrations curves for H-IgG at specific times.

Table 3-2. Values of linear regression with its respective uncertainties (for H-IgG detection).

Time (min)	Slope	y-intercept	L. Equation
30	0.0519 ± 0.0036	0.5962 ± 0.007	y = 0.0519x + 0.5962
45	0.0622 ± 0.0044	0.5092 ± 0.0084	y = 0.0622x + 0.5092
60	0.0648 ± 0.0033	0.4516 ± 0.0063	y = 0.0648x + 0.4516
90	0.0671 ± 0.0049	0.3729 ± 0.0095	y = 0.0671x + 0.3729

Through the Equation 1-7 and performing an interpolation process in the resulting linear equation, the LOD can be determined as follows,

$$X_{LOD} = \frac{(LoB + 3(SD_{Lowconcentrationsample})) - b}{m} \tag{3-1}$$

similarly, LOQ can be calculated through the expression:

$$X_{LOQ} = \frac{(\Delta B_l + 10(SD_{Bl})) - b}{m} \tag{3-2}$$

As a logarithmic transformation was made, it is necessary to carry out an exponential transformation to finally obtained the respective values of LOD = $10^{X_{LOD}}$ and LOQ = $10^{X_{LOQ}}$. Table 3-3 displays LOD and LOQ values calculated. Taking into account R^2 and

LOD values, for 60 minutes of assay we have the best results. So, the resulting values reflected that H-IgG is detected efficiently by the biosensing platform proposed.

Table 3-3. LOD and LOQ Values for H-IgG at respective times.

Time (min)	**[LOD] ng ml^{-1}**	**[LOQ] ng ml^{-1}**
30	3.17	60.6
45	3.8	13.7
60	2.38	15.5
90	3.74	22.3

Intra-assay Precision

As three parallel replicates are measured by each analyte concentration, it can be determined the intra-assay precision of the biosensing platform for detection of H-IgG. The present work takes the guidelines of the US Food and Drug Administration that indicate a CV (coefficient of variation) upper limit of 30 % can be accepted for biomarker quantification.[15,16] Table 3-4 shows the values obtained at the respective time for each H-IgG concentration. So, from Table 3-4, percentages go from 0.27 % to 5 % indicating that intra-assays precision is high and suitable for biomarker quantification.

Table 3-4. Precision values to each H-IgG concentration detected.

[H-IgG] ng mL^{-1}	**30 min CV %**	**45 min CV %**	**60 min CV %**	**90 min CV %**
Blank	1.37	1.26	1.53	2.10
9.37	0.27	2.10	0.69	2.18
37.5	3.49	1.72	2.35	1.16
75	0.44	1.29	1.59	0.93
150	3.24	3.98	3.04	3.10
300	0.92	1.19	1.0	0.89
600	3.71	1.96	4.80	3.93

3.3.2 The immunosensing platform targeting PSA detection

Optimization of GO concentration

Intending to validate that through the proposed immunosensing platform other clinically relevant proteins can be detected; we designed a configuration for the immunosensing of PSA using QDs-Anti-PSA as the biosensing probe. To this end, the GO concentration with which covered the surface of microwells should be determined. Three GO concentrations 1200, 1400, and 1600 µg mL^{-1} were selected to this end following the experimental procedure described in section 3.2.2. The range of PSA concentrations for this experiment were 4.68, 9.37, 18.75, 37.5, 75, 150, and 300 ng mL^{-1}. We established the final constant concentration of 0.05 nM for the biosensing probe (QDs-Anti-PSA) since it provided enough fluorescence intensity for the system. Then, an experiment was carried out following the experimental procedure for biodetection, previously described in section

3.2.2. The results of this experiment are depicted in Figure 3-8. In terms of quenching of fluorescence, the GO concentration of 1400 µg mL^{-1} was the one where the blank sample reached the most efficient levels. So, this concentration of GO is more adequate to cover the surface of the microwells.

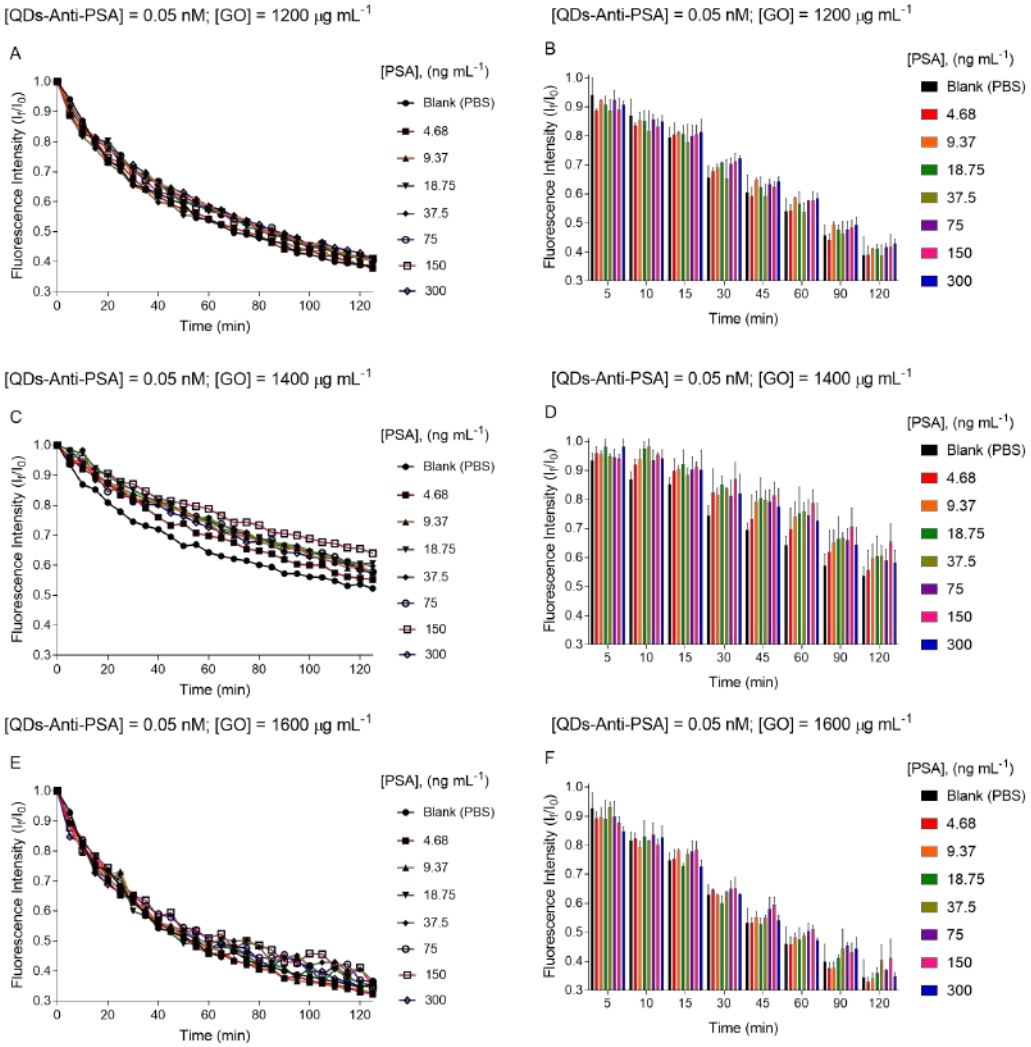

Figure 3-8. Optimization of the proposed immunosensing platform targeting PSA in terms of GO concentration. Experimental evidence resultant from GOµWs covered with a concentration of **A-B.** 1200 µg mL^{-1}. **C-D.** 1400 µg mL^{-1}. **E-F.** 1600 µg mL^{-1}. The concentration of the biosensing probe was kept constant (QDs at c.a. 0.05 nM conjugated with the antibody at c.a. 0.125 µg mL^{-1}).

Optimization of the biosensing probe targeting PSA

To continue with the optimization of the immunosensing platform for PSA detection, experiments to select the best biosensing probe concentration were performed following the experimental procedure described in section 3.2.2. The concentration of QDs was left constant (0.05 nM) since provides the fluorescence intensity suitable so that the quenching phenomenon caused by GO occurs efficiently. Three Anti-PSA concentrations (60, 50, and 28 ng mL^{-1}) were conjugated with the QDs concentration to determine which one provided the best analytical performance in terms of PSA detection. Such analytical

performance was monitored in terms of normal levels of PSA in healthy men, described in section 3.1.3, $\leq$ 4 ng mL^{-1}, so the initial analyte range was from 300 to 4 ng mL^{-1}. Figure 3-9 shows the graphs obtained for each Anti-PSA concentration. According to the operational principle of biodetection, the Anti-PSA concentration of 28 ng mL^{-1} generated better results than 60 and 50 ng mL^{-1} concentrations. Surprisingly, a rapid saturation is observed with relatively low concentrations of PSA (from concentrations $>$ 9.37 ng mL^{-1}) as depicted in Figure 3-9E-F. From these results, new experiments should be performed to establish the analytical range of PSA detection. Until now, 1400 µg mL^{-1} and 28 ng mL^{-1} are the optimal concentrations of GO and Anti-PSA (respectively) to be used in the immunosensing platform targeting PSA detection due to the blank reaching higher quenching levels compared to PSA concentrations indicating some of them were detected.

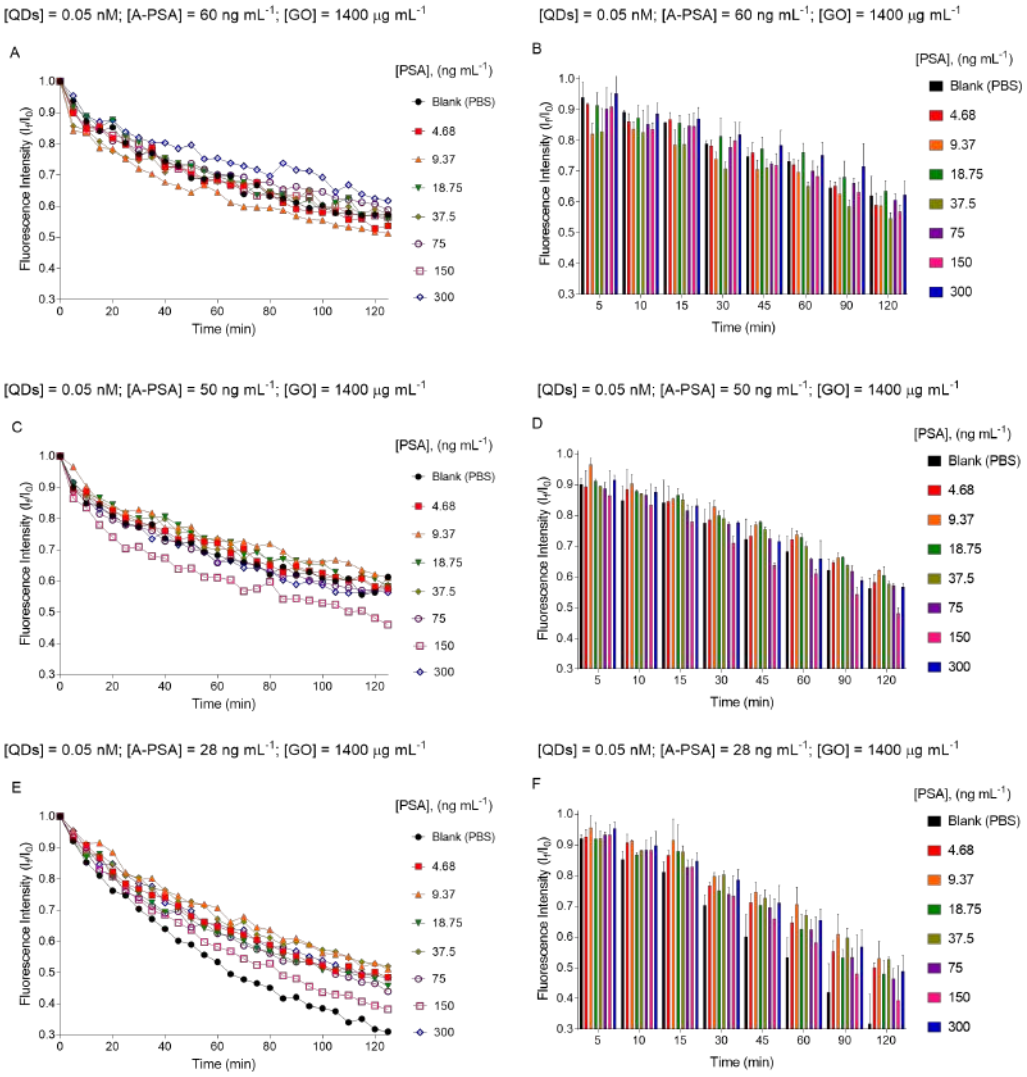

Figure 3-9. Optimization of the proposed immunosensing platform targeting PSA in terms of Ati-PSA concentration. Experimental behavior resultant from the antibody concentrated at **A-B.** 60 ng mL^{-1}. **C-D.** 50 ng mL^{-1}. **E-F.** 28 ng mL^{-1}. All the GOµWs were produced with GO concentrated at 1400 µg mL^{-1}. The final concentration of QDs was kept constant (0.05 nM). The error bars represent the standard deviation of three parallel experiments.

Analytical range for the detection of PSA

After a series of experiments, it was determined that the analytical range of PSA detection goes from 0.15 to 10 ng mL^{-1}. Serial dilutions were made until obtaining seven PSA concentrations. Figure 3-10 shows the optimal conditions for the detection of PSA. We can resume that (i) GO concentration of 1400 µg mL^{-1} provided excellent quenching levels for the employed biosensing probe concentration, (ii) conjugation of QDs at 0.05 nM with Anti-PSA at 28 ng mL^{-1} established the best biosensing probe to use in this immunosensing platform, (iii) sensitivity to PSA detection is high as reflected by the slopes calculated, see table 3-6. We can now proceed to determine the LOD and LOQ for PSA.

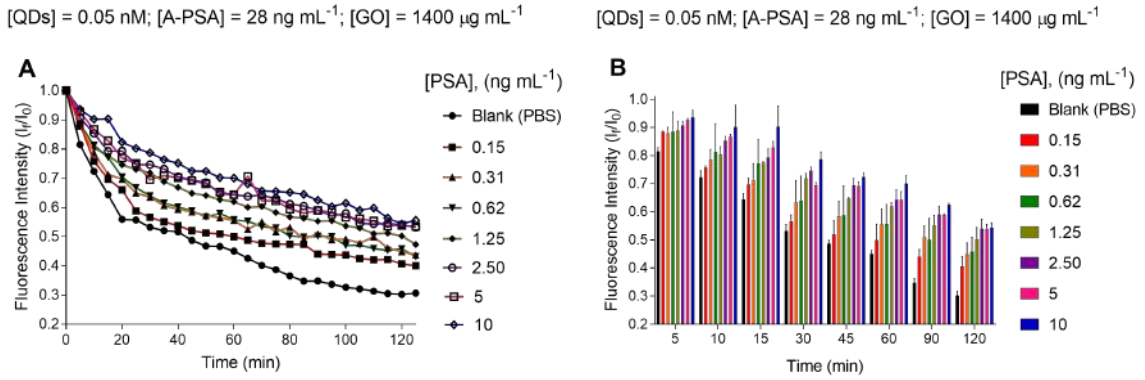

Figure 3-10. Analytical performance of immunosensing platform with optimal conditions for PSA detection. **A.** Real-time kinetic analysis of different concentrations of PSA and the blank, **B.** Relation between concentrations at different intervals to determine the best sensitivity.

Limit of detection and quantification of PSA

Likewise, we constructed the calibration curves from Figure 3-10B which is the experiment with the optimal immunoassay conditions for PSA detection since the biodetection is achieved following the operational principle. Also, a logarithmic transformation is applied to PSA concentrations in the x-axis. Then, the linear regression is carried out to the respective data, obtaining the curves of Figure 3-11. Coefficient of determination values R^2, which indicate the goodness of fitting, are shown in Table 3-5. In general, all values are above 0.9 units indicating suitable fitting to experimental data. Therefore, LOD and LOQ will be determined in all time intervals except for 30 minutes which was the only interval below 0.9.

Table 3-5. Coefficient of determination values resulting from each fitting curve (for PSA detection).

Time (min)	**5**	**10**	**15**	**30**	**45**	**60**	**90**	**120**
$\mathbf{R^2}$	0.9381	0.9303	0.9128	0.8631	0.9242	0.9459	0.9731	0.9677

Now, we need to establish the parameters of m and b, and so found the linear equation that allows us to estimate LOD and LOQ at specific times. Table 3-6 displays m and b values with their respective uncertainties calculated following equations described in

section 1.4.1. LOD and LOQ can be determined through equations 3-1 and 3-2, respectively.

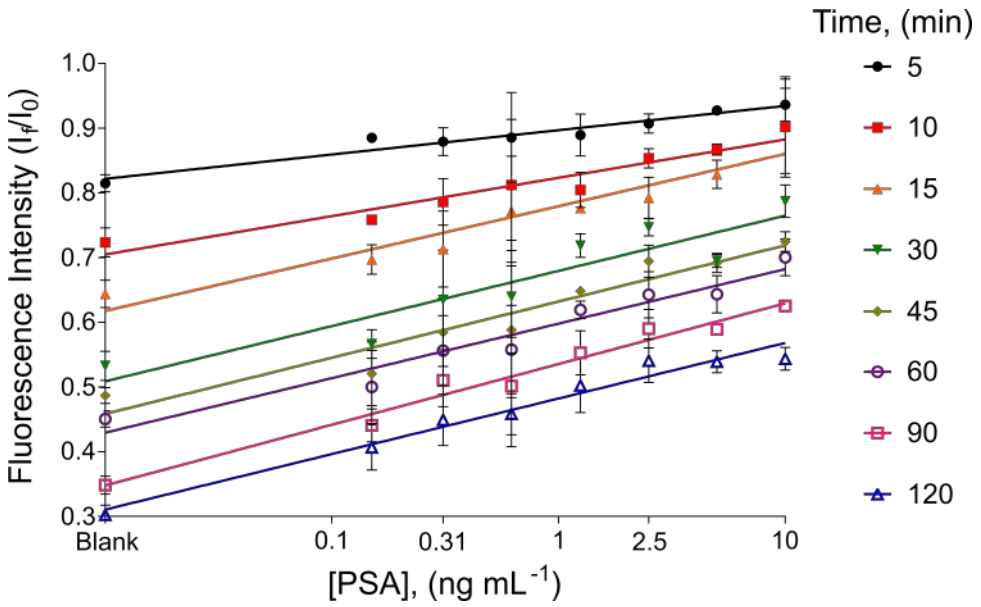

Figure 3-11. Calibrations curves for PSA at specific times.

Table 3-6. Values of linear regression with its respective uncertainties (for PSA detection).

Time (min)	Slope	*y*-intercept	L. Equation
5	0.0375 ± 0.0039	0.8217 ± 0.0080	y = 0.0375x + 0.8217
10	0.0592 ± 0.0066	0.7047 ± 0.0135	y = 0.0592x + 0.7047
15	0.0808 ± 0.0102	0.6175 ± 0.0208	y = 0.0808x + 0.6175
45	0.0868 ± 0.0101	0.4584 ± 0.0206	y = 0.0868x + 0.4584
60	0.0842 ± 0.0082	0.4294 ± 0.0167	y = 0.0842x + 0.4294
90	0.0938 ± 0.0063	0.3478 ± 0.0129	y = 0.0938x + 0.3478
120	0.0858 ± 0.0064	0.3105 ± 0.0130	y = 0.0858x + 0.3105

As a logarithmic transformation was made, it is necessary to carry out an exponential transformation to finally obtained the respective values of LOD = $10^{X_{LOD}}$ and LOQ = $10^{X_{LOQ}}$. Table 3-7 displays LOD and LOQ values calculated. So, those values reflected the high sensitivity of the immunosensing platform proposed for the detection of PSA. LOD and LOQ values are in concordance with the PSA concentrations examined.

Table 3-7. LOD and LOQ Values for PSA at respective times.

Time (min)	[LOD] ng mL^{-1}	[LOQ] ng mL^{-1}
5	0.033	20.98
10	0.12	133
15	0.165	8.58
45	0.31	0.5392
60	0.399	0.5558
90	0.049	0.3042
120	0.073	0.4749

Intra-assay Precision

Table 3-8 shows the CV values obtained at respective times for every PSA concentration. CV percentages go from 0.35 % to 17 % indicating that intra-assays precision is good for PSA quantification. Just for PSA concentration of 0.62 ng mL^{-1} CV values are relatively high (compared with other concentrations) so the precision for that concentration is fewer and therefore the variability was also higher for such concentration.

Table 3-8. Precision values to each PSA concentration detected.

[H-IgG] ng mL^{-1}	5 min CV %	10 min CV %	15 min CV %	45 min CV %	60 min CV %	90 min CV %	120 min CV %
Blank	1.62	3.12	3.28	2.50	2.79	3.98	5.03
0.15	0.35	0.71	3.29	9.46	11.32	5.80	8.61
0.31	2.46	4.58	8.25	9.04	9.74	7.94	8.83
0.62	7.86	12.46	11.00	17.78	12.25	15.03	11.10
1.25	3.66	3.39	0.40	0.48	2.23	6.14	8.34
2.5	1.62	1.74	4.01	3.60	5.54	5.04	6.25
5	0.57	0.99	2.64	2.16	4.49	0.78	3.13
10	2.73	8.61	8.07	2.09	4.08	0.96	3.24

3.4 Conclusions

The proposed GO-based immunosensing platform possesses good transformative capabilities for the detection of both H-IgG and PSA analytes. First, the immunosensing platform enjoys a high sensitivity, following the operational principle, in the detection of mentioned analytes as reflected by low LODs obtained. Also, the detection of mentioned analytes was reached before two hours whereas conventional assay times in ELISA are around 6 hours for the detection of H-IgG and PSA. The immunosensing platform is a highly transformative approach since can operates not only with different analytes but also with organic dye-conjugated antibodies and streptavidin-QDs conjugated to biotinylated antibodies due to the universal fluorescence quenching ability of GO this immunosensing platform can work at different wavelengths. Moreover, a single antibody conjugated with a fluorophore is necessary for its operation avoiding cumbersome procedures such as blocking, washing, or separation steps which contribute to save valuable time and reagents. Lastly, this immunosensing platform can be used for high-throughput in vitro diagnosis of clinical samples which indeed is the principal issue of the next chapter.

3.5 References

1. Ortiz-Riaño, E. J.; Avila-Huerta, M. D.; Mancera-Zapata, D. L.; Morales-Narváez, E. Microwell Plates Coated with Graphene Oxide Enable Advantageous Real-Time Immunosensing Platform. Biosensors and Bioelectronics 2020, 165, 112319. https://doi.org/10.1016/j.bios.2020.112319.

2. Avila-Huerta, M. D.; Ortiz-Riaño, E. J.; Mancera-Zapata, D. L.; Cortés-Sarabia, K.;

Morales-Narváez, E. Facile Determination of COVID-19 Seroconversion via Nonradiative Energy Transfer. ACS Sens. 2021, 6 (6), 2136–2140. https://doi.org/10.1021/acssensors.1c00795.

3. Morales-Narváez, E.; Merkoçi, A. Graphene Oxide as an Optical Biosensing Platform: A Progress Report. Advanced Materials 2019, 31 (6), 1805043. https://doi.org/10.1002/adma.201805043.

4. Cheeveewattanagul, N.; Morales-Narváez, E.; Hassan, A.-R. H. A.; Bergua, J. F.; Surareungchai, W.; Somasundrum, M.; Merkoçi, A. Straightforward Immunosensing Platform Based on Graphene Oxide-Decorated Nanopaper: A Highly Sensitive and Fast Biosensing Approach. Advanced Functional Materials 2017, 27 (38), 1702741. https://doi.org/10.1002/adfm.201702741.

5. Diem, S.; Fässler, M.; Bomze, D.; Ali, O. H.; Berner, F.; Niederer, R.; Hillmann, D.; Mangana, J.; Levesque, M. P.; Dummer, R.; Risch, L.; Recher, M.; Risch, M.; Flatz, L. Immunoglobulin G and Subclasses as Potential Biomarkers in Metastatic Melanoma Patients Starting Checkpoint Inhibitor Treatment. Journal of Immunotherapy 2019, 42 (3).

6. Reddy, M. M.; Wilson, R.; Wilson, J.; Connell, S.; Gocke, A.; Hynan, L.; German, D.; Kodadek, T. Identification of Candidate IgG Biomarkers for Alzheimer's Disease via Combinatorial Library Screening. Cell 2011, 144 (1), 132–142. https://doi.org/10.1016/j.cell.2010.11.054.

7. Russell, A. C.; Šimurina, M.; Garcia, M. T.; Novokmet, M.; Wang, Y.; Rudan, I.; Campbell, H.; Lauc, G.; Thomas, M. G.; Wang, W. The N-Glycosylation of Immunoglobulin G as a Novel Biomarker of Parkinson's Disease. Glycobiology 2017, 27 (5), 501–510. https://doi.org/10.1093/glycob/cwx022.

8. Talaat, F.; Ramadan, I.; Hamdy, E.; Sayed, A.; Elfatatry, A. M. Immunoglobulin G Index as a Biomarker of Relapse Response to Corticosteroids during Early Stages of Multiple Sclerosis. Multiple Sclerosis and Related Disorders 2020, 38, 101495. https://doi.org/10.1016/j.msard.2019.101495.

9. Heidenreich, A.; Bastian, P. J.; Bellmunt, J.; Bolla, M.; Joniau, S.; van der Kwast, T.; Mason, M.; Matveev, V.; Wiegel, T.; Zattoni, F.; Mottet, N. EAU Guidelines on Prostate Cancer. Part 1: Screening, Diagnosis, and Local Treatment with Curative Intent—Update 2013. European Urology 2014, 65 (1), 124–137. https://doi.org/10.1016/j.eururo.2013.09.046.

10. Potts Jeannette M. Prospective identification of national institutes of health category IV prostatitis in men with elevated Prostate Specific Antigen. Journal of Urology 2000, 164 (5), 1550–1553. https://doi.org/10.1016/S0022-5347(05)67026-7.

11. Azab, S.; Osama, A.; Rafaat, M. Does Normalizing PSA after Successful Treatment of Chronic Prostatitis with High PSA Value Exclude Prostatic Biopsy? Translational Andrology and Urology; Vol 1, No 3 (September 2012): Translational Andrology and Urology 2012.

12. Corning. Corning Cell Culture Surfaces.

13. Dimiev, A. M. Mechanism of Formation and Chemical Structure of Graphene Oxide. In Graphene Oxide; John Wiley & Sons, Ltd, 2016; pp 36–84. https://doi.org/10.1002/9781119069447.ch2.

14. Rico, F.; Russek, A.; González, L.; Grubmüller, H.; Scheuring, S. Heterogeneous and Rate-Dependent Streptavidin–Biotin Unbinding Revealed by High-Speed Force Spectroscopy and Atomistic Simulations. Proceedings of the National Academy of Sciences 2019, 116 (14), 6594–6601. https://doi.org/10.1073/pnas.1816909116.

15. Want, E. J.; Wilson, I. D.; Gika, H.; Theodoridis, G.; Plumb, R. S.; Shockcor, J.; Holmes, E.; Nicholson, J. K. Global Metabolic Profiling Procedures for Urine Using UPLC–MS. Nature Protocols 2010, 5 (6), 1005–1018. https://doi.org/10.1038/nprot.2010.50.

16. Want, E. J.; Masson, P.; Michopoulos, F.; Wilson, I. D.; Theodoridis, G.; Plumb, R. S.; Shockcor, J.; Loftus, N.; Holmes, E.; Nicholson, J. K. Global Metabolic Profiling of Animal and Human Tissues via UPLC-MS. Nature Protocols 2013, 8 (1), 17–32. https://doi.org/10.1038/nprot.2012.135.

Chapter 4

The immunosensing platform for the detection of Hsp72 and antibodies against SARS-CoV-2

This chapter outlines the procedures performed for the detection of Heat shock protein 72 and antibodies against SARS-CoV-2 using the fluorescence quenching-based immunosensing platform. Additionally, urine and human serum samples were analyzed to demonstrate the feasibility of the immunosensing platform for detecting analytes in real samples, serving as a proof-of-concept. The urine samples were supplied by Dr. Norma Bobadilla, who works with patients diagnosed with acute kidney injury, while the human serum samples were obtained from the Universidad Autónoma de Guerrero. All the experimental and statistical methods used to detect target analytes in real samples are thoroughly discussed.

4.1 Introduction

4.1.1 Clinical relevance of Heat shock protein 72 (Hsp72)

Acute kidney injury (AKI) is a clinical syndrome in which the kidneys stop working properly. In the last two decades, AKI has increased significantly due to the rising in obesity, diabetes, and hypertension.[1] Despite recent advances in technical development for clinical care, the rate of AKI mortality (which remains between 40 and 80 %) has not been reduced in the last decades on account of the lack of sensitivity or specificity in the current tools used for early AKI detection. In general, AKI is diagnosed by a rise in serum creatinine.[2,3] However, diverse investigations have demonstrated that serum creatinine levels rise too late, about 48 hours later, of ischemic insult (which is a disease in which Blood vessels shrink and undergo apoptosis which results in poor blood flow in the kidneys), so early diagnosis of AKI cannot be made through serum creatinine levels.[4,5] Therefore, is crucial the identification of sensitive renal biomarkers which facilitates not only the early diagnosis but also the monitoring of AKI. Likewise, ideal biomarkers are those easily detectable and non-invasive. In response to AKI, different mechanisms are activated to regulate the resultant cell injury one of those is the up-regulation of heat

shock proteins (Hsp) that helps to restore the homeostasis of cells. Specifically, the Hsp70 family is constituted by four isoforms: Hsc70, Hsp72, mHsp75, and Grp78. It was demonstrated that during AKI, Hsp72 is induced in renal tubules, and at the same time, proximal tubular detachment is released into the urinary space, so urinary Hsp72 level served as an early biomarker to monitor and detect AKI induced by bilateral renal ischemia/reperfusion.[6] AKI also might be instigated by drugs such as cisplatin (a chemotherapeutic agent used in the treatment of many tumors) or acetaminophen (an analgesic agent widely used to reduce fever and alleviate mild pain) since such drugs are eliminated by kidneys.[7] All in all, Hsp72 is a novel biomarker for the early diagnosis of AKI induced not only by ischemia/reperfusion but also by drug renal toxicity.

4.1.2 COVID-19 global pandemic

At the end of 2019, numerous cases of atypical pneumonia were detected in China, and the viral agent responsible for such infection was quickly identified, Severe Acute Respiratory Syndrome Coronavirus 2 (SARS-CoV-2).[8] In mid-March 2020, the World Health Organization (WHO) proclaimed SARS-CoV-2, responsible for the Coronavirus disease 2019 (COVID-19), as a pandemic, unchaining catastrophic scenarios for economic, public health, and social order. The WHO recommended the international community conduct mass diagnostic testing to reduce virus transmission, avoiding then the saturation of the health system. COVID-19 diagnostic testing is also a valuable resource for understanding the modus operandi of this emerging infectious disease.[9] Moreover, they play a crucial role in deciding convenient decisions regarding the treatment and isolation of infected individuals.

Generally, there are three testing approaches to detect COVID-19, (i) the gold standard in immunodetection: the Polymerase Chain Reaction (PCR) testing which is based on the amplification of specific DNA segments collected from nasopharyngeal samples.[8] PCR testing amplifies tiny portions of ribonucleic acid of SARS-CoV-2 which offers a high sensitivity and specificity biodetection. However, PCR testing just permits virus detection in a short period, generally during an acute COVID-19 infection. (ii) serological tests that detect antibodies produced by the immune system as a defense mechanism against COVID-19, specifically against the spike (S) protein of SARS-CoV-2.[9] The immune system produces during the first 7-10 days of infection the maximum levels of immunoglobulin M (IgM), and after high levels of immunoglobulins G (IgG) directed against spike S protein are produced. Serological tests are carried out directly from serum or human blood, and there are many commercial tests available to detect qualitatively antibodies produced against the spike (S) protein of SARS-CoV-2. (iii) the capture and detection of the complete virus to determine the viral load via specific SARS-CoV-2 antibodies, whose analysis can be performed through saliva or nasopharyngeal samples.[8,9] Herein, fluorescent-tagged SARS-CoV-2 spike receptor-binding domain recombinant protein F-RBD was envisaged to operate as a biosensing probe for the detection of COVID-19 antibodies. The detection process is achieved following the operational principle and experimental procedure described in sections 3.1.1 and 3.2.2, respectively. This work was funded by CONACYT (Grant No. 376135).

4.2 Experimental section

4.2.1 Hsp72 and Anti-Hsp72: general description

The Hsp72 was purchased from Boston Biochem (cat 09956315C) and the Anti-Hsp72 was produced by Dr. Norma Bobadilla and her group at the Molecular Physiology Unit, Instituto de Investigaciones Biomédicas, Universidad Nacional Autónoma de México. Anti-Hsp72 is conjugated with biotin, with a stock concentration of 0.75 mg mL^{-1}. On the other hand, Hsp72 has a stock concentration of 0.5 mg mL^{-1}. As mentioned previously, Hsp72 is an isoform of the Hsp70 family. Heat shock proteins have important functional characteristics such as crucial participation in protein folding, cell stress regulation, and actively participating in cell signaling and immune responses.[6,7]

4.2.2 Conjugation of QDs and Anti-Hsp72

Streptavidin-QDs 655, whose properties were described in section 3.2.5, was conjugated with Biotin-Anti-Hsp72 by non-covalent interactions mentioned in the same section. To establish concentrations of both Streptavidin-QDs and Biotin-Anti-Hsp72 more suitable for conjugation, an experiment was carried out. Firstly, several microwells of a high-binding plate were decorated with 100 µL of Biotin-Anti-Hsp72 concentrated at 100 µg mL-1 and left overnight to allow decoration of the sensing surface. After that, three washing steps are made to the microwells with PBS containing Tween® detergent at 1 % (PBST), to remove the excess of Biotin-Anti-Hsp72 that did not attach onto the microwell. Then, a blocking step is performed in each microwell with blocking buffer (0.5 g milk powder (Nestlé) + 9mL PBS + 1 mL PBST) avoiding thus nonspecific bindings. To this, 50 µL of blocking buffer is added into microwells and left for 45 minutes at constant shaking, 800 rpm. Five washing steps with PBST are also made to each microwell to remove the excess of blocking reagent. Six Streptavidin-QDs concentrations (0.37, 0.75, 1.5, 3, 6 and 12 nM) were prepared and Biotin-Anti-Hsp72 at 100 µg mL^{-1} was also prepared. Then, 50 µL of Streptavidin-QDs and 50 µL of Anti-Hsp72 at 100 µg mL^{-1} were added to the Anti-Hsp72-coated microwells. Specifically, two Anti-Hsp72-coated microwells per concentration of streptavidin-QDs. Also was left interacting for 45 minutes at constant shaking, 800 rpm. The last washing step is made, and 100 µL of PBS is added to every microwell. The fluorescence intensity of microwells is measured by the Cytation 5 plate reader, and figure 4-1 shows the fluorescence intensities measured. The fluorescence signals indicate that there is an excess of Streptavidin-QDs since these start binding with Biotin-Anti-Hsp72 attached to microwell surfaces. Compare with the reference sample (no QDs present), just for Streptavidin-QDs concentration of 12 nM, there is a fluorescence signal. So, from that concentration start to have an excess of QDs. We concluded that an intermediate concentration of Streptavidin-QDs between 6 and 12 nM is suitable for the optimal conjugation with Anti-Hsp72 at 100 µg mL-1. Particularly, we chose the 8 nM Streptavidin-QDs concentration for all the conjugation experiments. This was the protocol also followed by the conjugation of Streptavidin-QDs and Biotin-Anti-PSA described in section 3.2.5.

4.2.3 The immunosensing platform targeting SARS-CoV-2 Spike RBD Antibodies

This work headed by Dr. Eden Morales-Narváez was carried out by his students Mariana Avila-Huerta and Edwin J. Ortiz-Riaño. My workmate Mariana conducted all the experiments for the detection of SARS-CoV-2 spike RBD antibodies and also carried out the experiments for the detection of COVID-19 antibodies in human serum samples. In this context, I performed all the statistical analyses of human serum samples. So, I will describe such statistical analyses of samples. Firstly, it is necessary to describe the optimal immunosensing conditions for the detection of SARS-CoV-2 Spike RBD antibodies. The GO concentration used to cover the surface of the microwells was 1200 µg mL^{-1}. The biosensing probe (F-RBD) concentration was 60 ng mL^{-1}, and for the conjugation process, a FITC conjugation kit (fast)-lightning-link (ab188285) was used to bind FITC with SARS-CoV-2 Spike RBD Recombinant Protein (Cat: 40592-VNAH). The analytical range for the analyte detection was 0.0039-0.5 ng mL^{-1}. The kinetic analysis was for two hours with fluorescence intensity readings every 3 minutes. The orbital shaking mode with a velocity of 180 cpm was added to the kinetic analysis. The best sensitivity of the assay was reached at 42 minutes, and LOD obtained at that time was 3 pg mL^{-1}. The results obtained from this work are published in the American Chemical Society journal, ACS Sensors.[10]

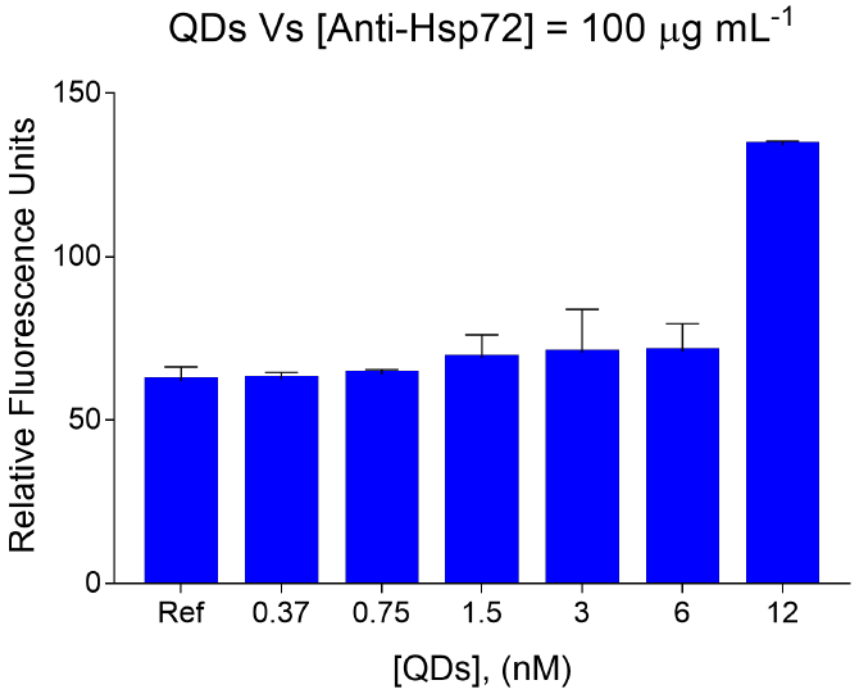

Figure 4-1. Fluorescence signals resulted from the conjugation of Biotin-Anti-Hsp72 and different concentrations of Streptavidin-QDs. Just for the 12 nM concentration, there is a fluorescence signal.

4.2.4 Serum collection

Clinical samples were provided by the Universidad Autónoma de Guerrero. 28 serum samples were negative, collected in 2014 and stored at -20 °C, and 6 were positives

collected from subjects who had a positive COVID-19 PCR test (at least 30 days before serum extraction). All the samples were deactivated following the procedures described in the literature to avoid the risk of infection.[11] These serum samples were obtained with informed consent, as all subjects signed a document adhering to the ethical principles of the Helsinki Declaration (2013). The dilutions of samples were made with PBS and immunoassays with human serum samples were conducted following the experimental procedure section 3.2.2. The only difference regarding the experimental procedure is that kinetic analysis with human serum samples was made for 48 minutes with fluorescence intensity readings every 3 minutes.

4.3 Results and discussion

4.3.1 The immunosensing platform targeting Hsp72

Optimization of GO concentration

As usual, we need to establish the suitable GO concentration which covers the surface of plate microwells intending to obtain the best quenching of fluorescence. A kinetic analysis was performed with four GO concentrations 1600, 1400, 1200, and 800 µg mL^{-1}. Final concentrations for QDs and Anti-Hsp72 were 0.05 nM and 625 ng mL^{-1}, respectively. Such QDs concentration was chosen since provided adequate fluorescence intensity to the fluorescence quenching phenomenon occurs. Figure 4-2 depicts the results of kinetic analysis for every GO concentration. Following the curves of Figure 4-2A, concentrations of 1200 and 800 µg mL^{-1} reached more quenching of fluorescence. Particularly, the GO concentration of 1200 µg mL^{-1} has lower levels of fluorescence which means a more quenching phenomenon. So, this concentration is optimal to quench the fluorescence intensity provided by the QDs concentration used.

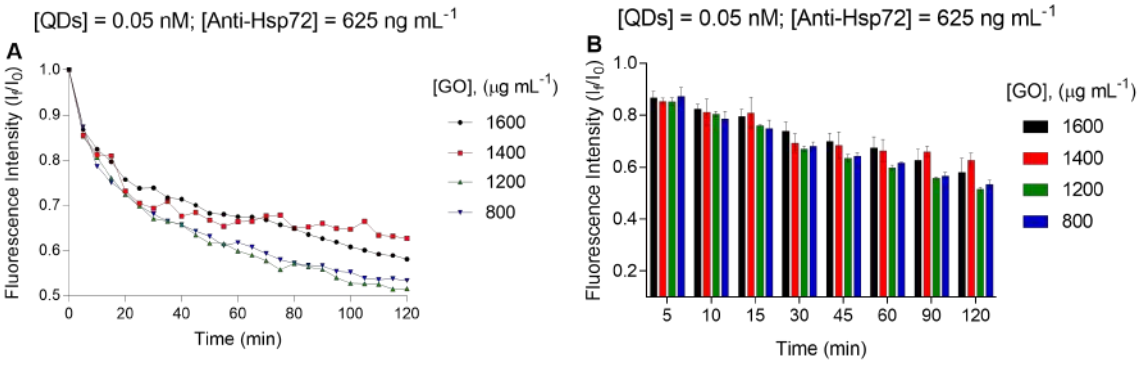

Figure 4-2. Quenching of fluorescence experiment for GO optimization. **A.** Kinetic analysis for fluorescence intensity behavior. **B.** graph of bars at different time intervals.

4.3.2 Optimization of biosensing probe

Knowing the GO concentration that is more convenient to be used in the immunosensing platform, experiments were carried out to determine the proper concentration of Anti-Hsp72, and so establish the optimal biosensing probe (the conjugation of QDs and Anti-Hsp72). Seven serial concentrations of Hsp72 (0.156-10 ng mL^{-1}), and the blank were selected for the experiments. Three Anti-Hsp72 concentrations (312, 781, and 937 ng mL^{-1}) were conjugated with the QDs concentration to determine which ones provide the best analytical performance in terms of Hsp72 detection. The experiments were performed following the experimental procedure described in section 3.2.2. Figure 4-3 shows the results obtained from this experiment. In general, the analyte (Hsp72) was detected by the three biosensing probe concentrations. However, the error is considerably high for Anti-Hsp72 concentrations of 312 and 937 ng mL^{-1}, just as depicted in graph bars. The analytical performance provided by the Anti-Hsp72 concentration of 781 ng mL^{-1} is better since the blank reached highly efficient quenching levels which are in concordance with the operational principle described in section 3.1.1. Nonetheless, error levels for the blank are high, so is important to decrease the error since is vital in the determination of LOD and LOQ. The last step is determining the analytical range in which Hsp72 can be detected by the immunosensing platform.

Analytical range of detection for Hsp72

The analytical range for Hsp72 detection goes from 0.78 to 50 ng mL^{-1}. Serial dilutions were made to evaluate seven Hsp72 concentrations. Figure 4-4 depicts the immunosensing platform targeting Hsp72 with optimal sensing conditions. The difference in quenching levels between the blank and the highest analyte concentration is large, and as a consequence, the sensitivity of this configuration will be high. On the other hand, the error in all analyte concentrations and the blank is small (less than 4 %, see table 4-4) which suggests that all were detected with excellent precision. Now LOD and LOQ can be determined from these results.

Limit of detection and quantification

We need to construct the calibration curves to determine LOD and LOQ values. Figure 4-5 shows these curves for time intervals depicted in Figure 4-4B. A logarithmic transformation is performed to Hsp72 concentrations of the x-axis follow by the linear regression fitting. Then, determination coefficients R2 are calculated to determine the goodness of fitting whose values are shown in Table 4-1. These R^2 values reflected the reliability of linear fitting for all time intervals except for 5 minutes.

Table 4-1. Coefficient of determination values resulting from each fitting curve.

Time (min)	**5**	**10**	**15**	**30**	**45**	**60**	**90**	**120**
$\mathbf{R^2}$	0.8859	0.9416	0.926	0.9585	0.9715	0.9759	0.9863	0.9781

We can proceed to establish the linear equation for each calibration curve through equations described in section 1.4. Table 4-2 displays the correspondent linear param-

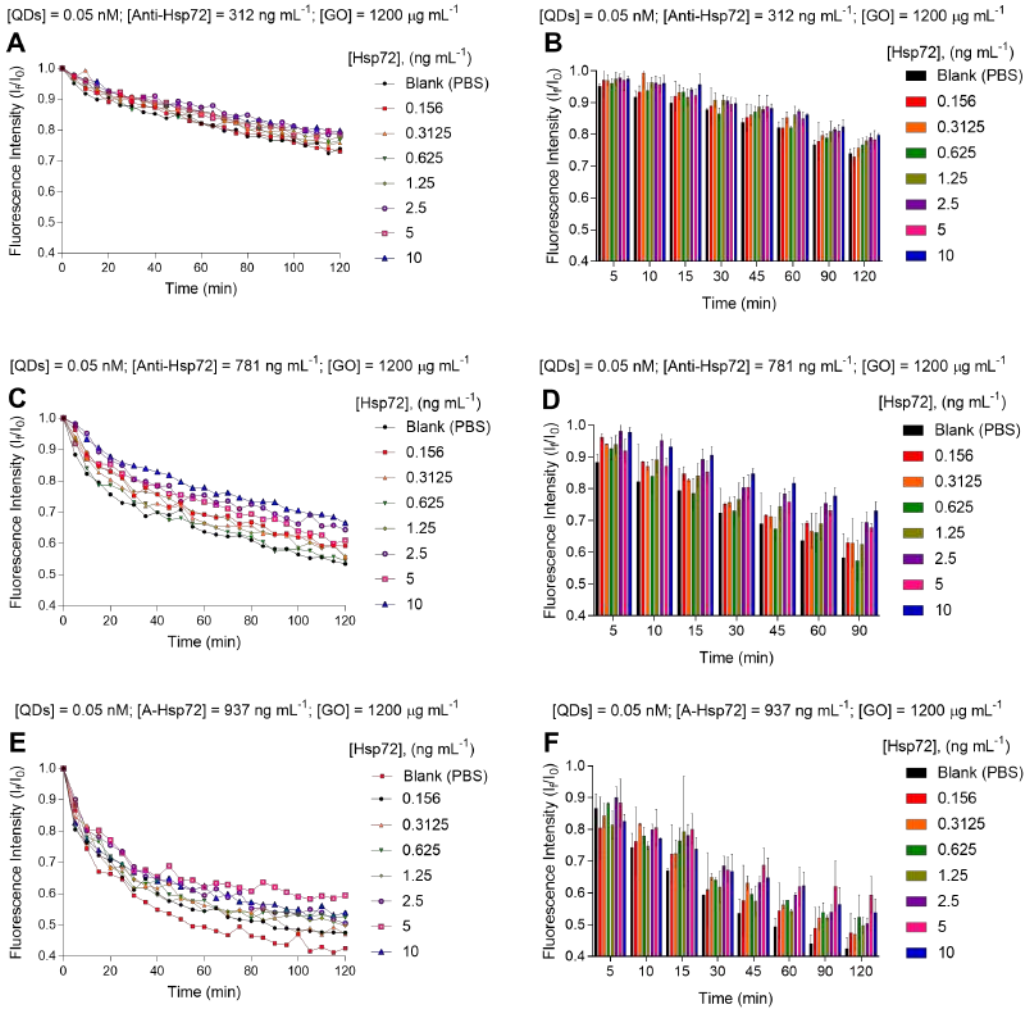

Figure 4-3. Optimization of the proposed immunosensing platform targeting Hsp72 in terms of Anti-Hsp72 concentration. Experimental behavior resultant from the antibody concentrated at **A-B.** 312 ng mL^{-1}. **C-D.** 781 ng mL^{-1}. **E-F.** 937 ng mL^{-1}. All the GOµWs were produced with GO concentrated at 1400 µg mL^{-1}. The final concentration of QDs was kept constant (0.05 nM). The error bars represent the standard deviation of three parallel experiments.

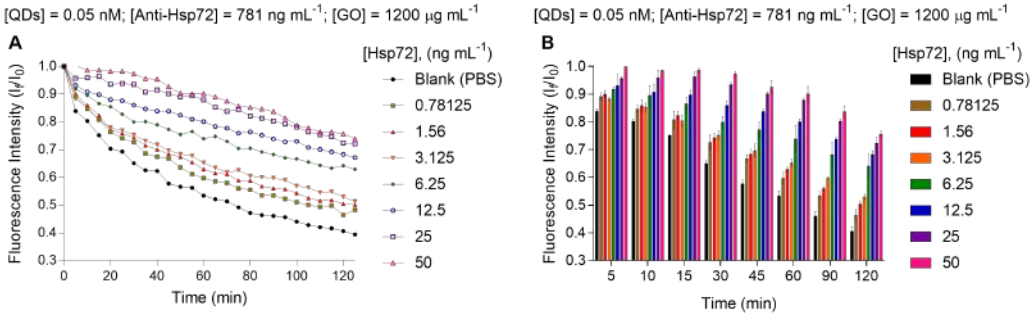

Figure 4-4. Analytical performance of immunosensing platform with optimal conditions for Hsp72 detection. **A.** Real-time kinetic analysis of different concentrations of PSA and the blank, **B.** Relation between concentrations at several intervals to determine the best sensitivity.

eters (with their respective uncertainties) and equations. Thus, LOD and LOQ can be calculated following equations 3-1 and 3-2. The linear parameters and therefore the linear equation was not calculated to 5 minutes since the coefficient of determination was poor reflecting not good fitting for that interval.

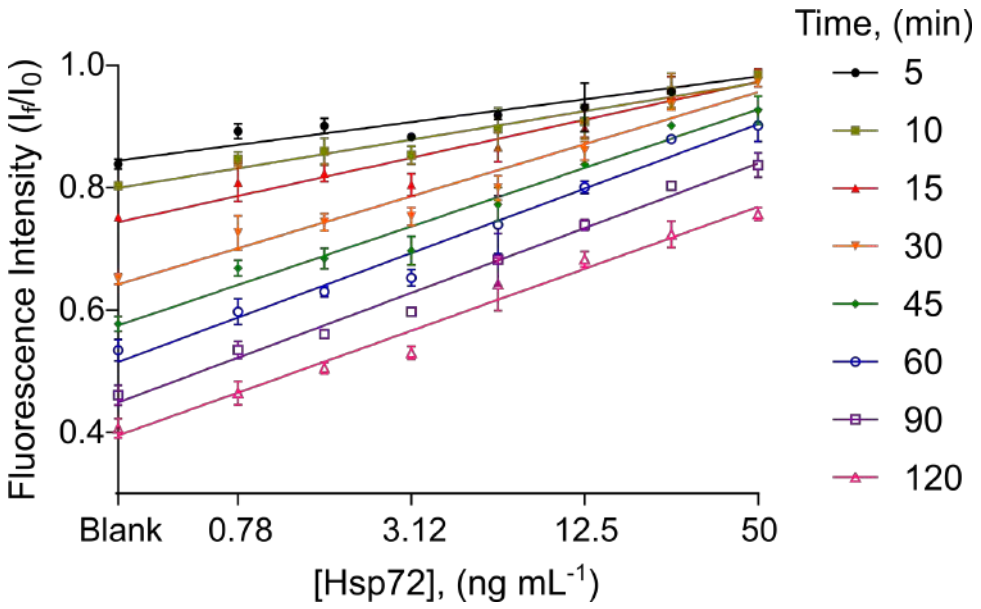

Figure 4-5. Calibrations curves for Hsp72 at specific times.

Table 4-2. Values of linear regression with its respective uncertainties.

Time (min)	Slope	*y*-intercept	L. Equation
10	0.0775 ± 0.0078	0.8401 ± 0.0075	y = 0.0775x + 0.8401
15	0.1034 ± 0.0119	0.7976 ± 0.0113	y = 0.1034x + 0.7976
30	0.1414 ± 0.0120	0.716 ± 0.0114	y = 0.1414x + 0.716
45	0.159 ± 0.0111	0.658 ± 0.0105	y = 0.159x + 0.658
60	0.175 ± 0.0112	0.6064 ± 0.0106	y = 0.175x + 0.6064
90	0.1759 ± 0.0084	0.5409 ± 0.0080	y = 0.1759x + 0.5409
120	0.1682 ± 0.0102	0.4828 ± 0.0097	y = 0.1682x + 0.4828

The LOD and LOQ can be determined to take into account that a logarithmic transformation was made so it is necessary to carry out an exponential transformation to finally obtained the respective values of LOD = $10^{X_{LOD}}$ and LOQ = $10^{X_{LOQ}}$. Table 4-3 shows the values calculated for LOD and LOQ. Interestingly, LOQ values were considerably low indicating an excellent sensitivity.

Table 4-3. LOD and LOQ Values for respective times.

Time (min)	[LOD] ng ml^{-1}	[LOQ] ng ml^{-1}
10	0.83	2.60
15	1.26	0.70
30	0.94	1.51
45	0.57	1.91
60	0.89	3.82
90	0.68	3.05
120	0.77	3.05

Intra-assay precision

Finally, the precision was calculated for each Hsp72 dilution. Table 4-4 shows CV values determined for every concentration at specific times. Such values go from 0.39 to 4.15 % reflecting the high intra-assay precision with which Hsp72 can be detected and quantified. This has important relevance to the detection and analysis of real samples which is described below.

Table 4-4. Precision values to each Hsp72 concentration detected.

[Hsp72] ng mL^{-1}	10 min CV %	15 min CV %	30 min CV %	45 min CV %	60 min CV %	90 min CV %	120 min CV %
Blank	0.86	0.39	1.38	2.17	3.26	3.58	3.89
0.78	1.38	3.85	3.86	1.92	3.54	2.62	4.15
1.56	2.47	1.68	1.87	2.50	1.35	1.01	1.86
3.12	1.72	2.29	1.97	3.42	2.01	0.69	1.99
6.25	3.92	2.77	2.49	3.53	6.41	6.22	6.78
12.5	3.09	1.77	1.79	0.81	1.24	1.16	1.89
25	2.93	1.92	0.83	0.68	0.71	0.73	2.96
50	0.23	0.73	0.82	2.45	2.90	2.40	1.37

4.3.3 Immunosensing of Hsp72 in urine samples

Urine samples were tested to analyze if Hsp72 can be detected in real samples by the immunosensing platform proposed. As previously mentioned, urinary Hsp72 level served as an early biomarker to monitor and detect AKI induced by bilateral renal ischemia\ reperfusion. The group headed by Dr. Norma Bobadilla demonstrated that normal urine Hsp72 levels from healthy donors are 0.22 ± 0.07 whereas values from patients diagnosed with AKI are $\geq 4.90 \pm 1.5$ ng mL^{-1}.[4] Patients who are hospitalized by AKI, exhibit urinary levels of Hsp72 above 10 ng mL^{-1}. Initially, Dra Norma sent us nine urine samples from patients that were diagnosed with AKI. We collected other nine urine samples from volunteers without kidney injuries. All experiments were conducted with the optimal conditions for Hsp72 detection which are depicted in figure 4-4. The kinetic analysis also was for two hours with readings every 5 minutes. The next step was to establish adequate sample dilution that permits distinguishing positive from negative samples. The first dilution factor tested was 1/4, and then an experiment was carried

out following the experimental procedure described in section 3.2.2. Figure 4-6 shows the results of the immunoassay.

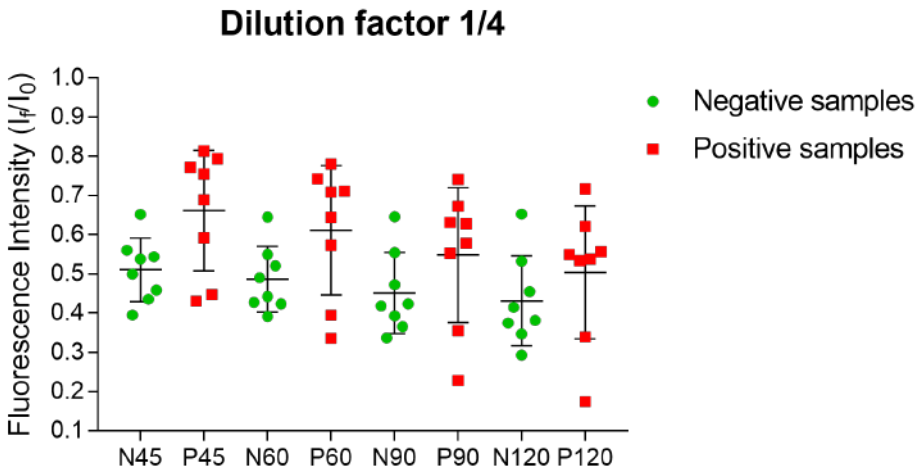

Figure 4-6. Dilution factor of 1/4. Photoluminescent behavior of QDs-Anti-Hsp72 incubated with diluted urine samples in GO-covered surfaces at different times of assay. The experiment was performed with the optimal immunoassay condition for Hsp72 detection.

The intention of figure 4-6 is to compare the fluorescence intensity levels (I_f / I_0) of the two groups: negative and positive samples. It is expected that I_f / I_0 levels of negative samples are lower compared with positives where Hsp72 is present. Following the operational principle of biodetection (section 3.1.1), the more analyte concentration (Hsp72), the less quenching of fluorescence of the biosensing probe. Figure 4-6 depicts the fluorescence intensity levels (I_f / I_0) for both groups of samples at four-time intervals: 45, 60, 90 y 120 minutes. These intervals were selected for analysis since R^2 values (in the calibration curve) are close to 1, so more confidence will have the results for such intervals. Although for 90 and 120 minutes majority of samples get together for both positive and negative samples, there is no considerable difference in I_f / I_0 levels between the two groups. From this fact, we conducted another experiment with a dilution factor of 1/6, and under the same experimental conditions described previously. The results of this experiment are shown in figure 4-7A. It is observed that at 90 and 120 minutes there is a clear difference in I_f / I_0 levels between negative and positive samples. Following the behavior of negative samples, they get together reaching almost the same I_f / I_0 level. On the contrary, positive samples are a little more dispersed which makes sense since each sample has a determined level of Hsp72. So, with a dilution factor of 1/6, the immunosensing platform is capable of detect Hsp72 in urine samples.

We decided to explore with a dilution factor of 1/8, and the performance of the experiment is depicted in Figure 4-7B. The detection efficiency decreased with this dilution due to there is not a considerable difference in I_f / I_0 levels between positive and negative samples. Thus, we concluded that the dilution factor of 1/6 is optimal to detect urinary Hsp72 levels. The optimal time where both sample groups are more distant regarding I_f / I_0 levels is at 90 minutes of assay, which was also in good agreement with the aforementioned optimum conditions to achieve the highest analytical sensitivity in Hsp72 detection. As mentioned before, these results helped to demonstrate that the immunosensing platform proposed is viable for immunodetection in real samples. Indeed,

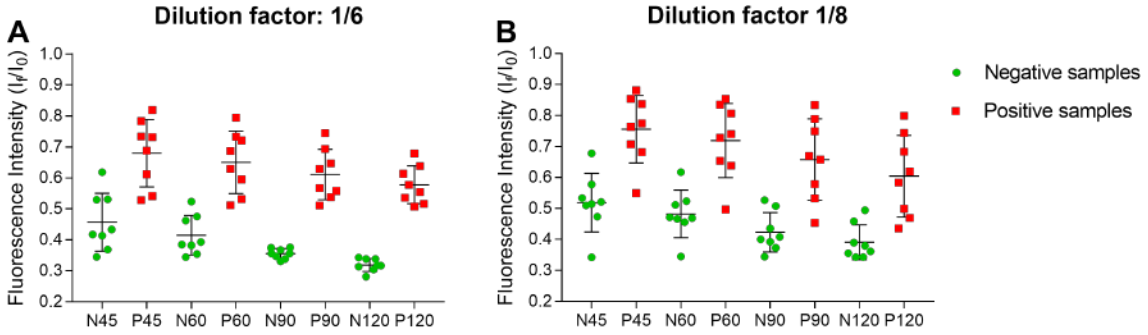

Figure 4-7. Photoluminescent behavior of QDs-Anti-Hsp72 incubated with diluted urine samples in GO-covered surfaces at different times of assay. **A.** dilution factor of 1/6, **B.** dilution factor of 1/8. Experiments were performed with the optimal immunoassay condition for Hsp72 detection.

due to the global pandemic situation, the project could not continue since Dr Norma could not continue sent us more real samples and necessary reagents.

Finally, we analyzed the detection performance of urinary Hsp72 at 90 minutes of assay, which was the optimal immunoassay interval. The I_f / I_0 levels of the blank and the LOD are represented by dot lines in figure 4-8. All negative AKI samples are below the blank suggesting high concordance of results. On the other hand, AKI samples are above LOD and below of Hsp72 concentration of 12 ng mL^{-1}. The I_f / I_0 levels of the blank, LOD, and Hsp72 concentration were taken from the calibration curve, figure 4-5. This is just a qualitative analysis that permits arguing the coherence of results due to the lack of experimentation with more urine samples related to AKI. All in all, urinary Hsp72 samples from patients diagnosed with AKI can be potentially tested by our immunoassay proposal even at different stages of AKI disease.

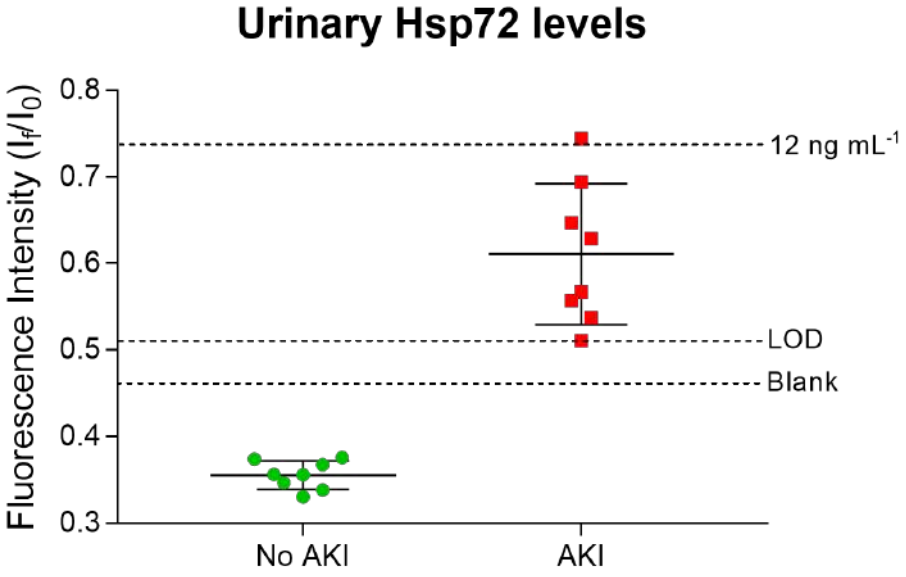

Figure 4-8. Dilution factor of 1/6. Photoluminescent behavior of QDs-Anti-Hsp72 incubated with diluted urine samples in GO-covered surfaces at 90 minutes of assay. Dot lines represent I_f / I_0 levels of the blank, LOD, and Hsp72 concentration of 12 ng mL^{-1}.

4.3.4 Immunosensing of COVID-19 antibodies in human blood serum

The human blood serum samples described above were tested to explore if COVID-19 antibodies can be detected by our biosensing platform. According to the LOD obtained with our immunosensing proposal and the minimum COVID-19 antibodies dilution used in available ELISA kits ($\sim$1/6400),[12] we decided to execute a series of experiments with three dilution factors 1/6000, 1/7000, and 1/8000. For these experiments, four pre-COVID-19 and two COVID-19 samples were tested, Figure 4-9 depicts the results provided by these assays. To compare the means of I_f / I_0 levels of the two groups, we performed an unpaired t-test which is a statistical method that compares the means of two unmatched groups. The statistical significance P is a parameter that refers to the claim that a set of observed data are not the result of chance but can instead be attributed to a specific cause. Particularly, the P-value indicates if there is a difference in the means of I_f / I_0 levels of the two groups (positive and negative samples): the lower the P-value, the bigger the difference in the means of I_f / I_0 levels of such groups. In other words, COVID-19 samples should have greater I_f / I_0 levels than pre-COVID-19 samples since there is an increased amount of antibodies produced against SARS-CoV-2, following the operational principle of biodetection (section 3.1.1). The level at which one can accept whether an event is statistically significant is known as the confidence level, so if the P-value falls below the confidence level, then the result is statistically significant. In this case, the confidence level selected for the t-test was 95 % ($P < 0.05$). None of the dilutions tested showed a P-value with a confidence level, following the tables depicted in figure 4-9. However, dilution factors of 1/7000 and 1/8000 reached better P-values.

From previous results, we decided to conduct an immunoassay with 14 pre-COVID-19 and 6 COVID-19 samples diluted at 1/8875, and the performance of such immunoassay is presented in figure 4-10. There was a clear difference between the two groups in terms of I_f / I_0 levels. Such difference is evident throughout the kinetic analysis of 48 minutes which suggests that factor dilution of 1/8875 is better to avoid possible matrix interferences that might hinder the biodetection. Equally, the unpaired t-test was applied and all P-values fall below of confidence level (< 0.05) reflecting the statistical significance between the two groups regarding I_f / I_0 levels and therefore the biodetection of COVID-19 specific antibodies.

We conducted another immunoassay with the same pre-COVID-19 and COVID-19 samples but with a higher dilution factor: 1/11875. The intention was to explore if biodetection improved by increasing the dilution factor whose results are shown in figure 4-11. Concerning I_f / I_0 level separation of the two groups, both dilution factors have similar performance. P-values are also similar for the two dilution factors. Same way, although there is a considerable difference in the means of I_f / I_0 level of two groups with both dilution factors 1/8875 and 1/11875, is needed that both groups are separated to claim that we know the optimal dilution factor. Thanks to the fact that we obtained a low LOD regarding SARS-CoV-2 antibodies detection (3 pg mL^{-1}), it has been possible to explore high dilutions factor without loose detection sensitivity.

The dilution factor of 1/12220 was also explored and the performance of this immunoassay is depicted in figure 4-12. In this immunoassay, all pre-COVID-19 and COVID-19 samples were tested and we observed that from 15 minutes of assay the sep-

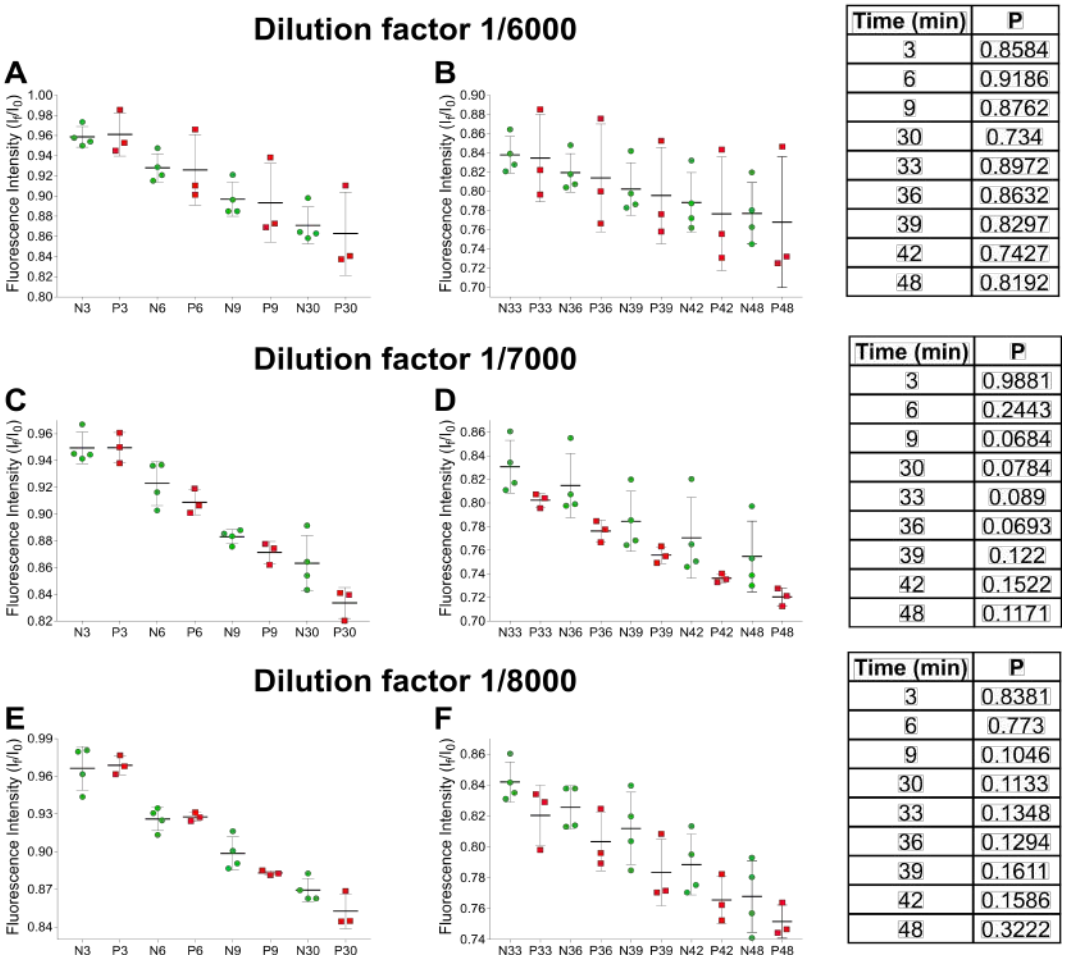

Time (min)	P
3	0.8584
6	0.9186
9	0.8762
30	0.734
33	0.8972
36	0.8632
39	0.8297
42	0.7427
48	0.8192

Time (min)	P
3	0.9881
6	0.2443
9	0.0684
30	0.0784
33	0.089
36	0.0693
39	0.122
42	0.1522
48	0.1171

Time (min)	P
3	0.8381
6	0.773
9	0.1046
30	0.1133
33	0.1348
36	0.1294
39	0.1611
42	0.1586
48	0.3222

Figure 4-9. Performance of the assay with diluted sera throughout time (3 to 48 minutes). **A.** analysis to dilution factor: 1/6000. **B.** analysis to dilution factor: 1/7000. **C.** analysis to dilution factor: 1/8000. The box plots display the median and the extreme values of the respective distribution.

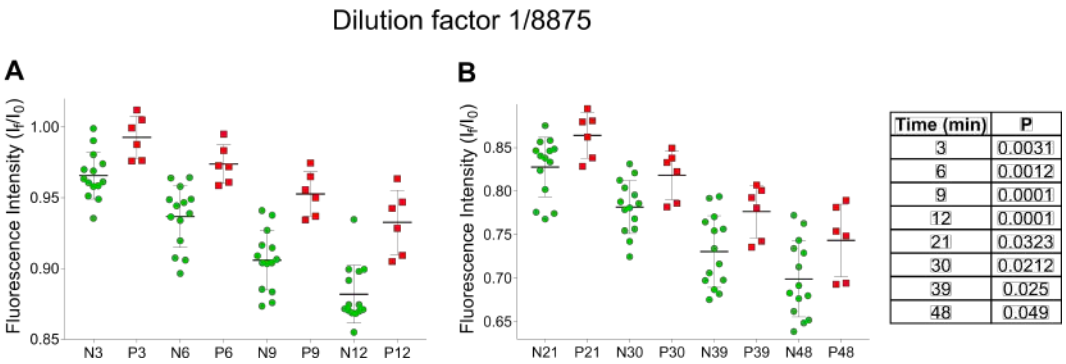

Time (min)	P
3	0.0031
6	0.0012
9	0.0001
12	0.0001
21	0.0323
30	0.0212
39	0.025
48	0.049

Figure 4-10. Performance of the assay with sera throughout time (3-48 minutes). Dilution factor: 1/8875. 12 pre-COVID-19 samples (N) and 6 COVID-19 subjects (P) were assayed. **A.** Analysis from 3 to 12 minutes. **B.** Analysis from 21 to 42 minutes.

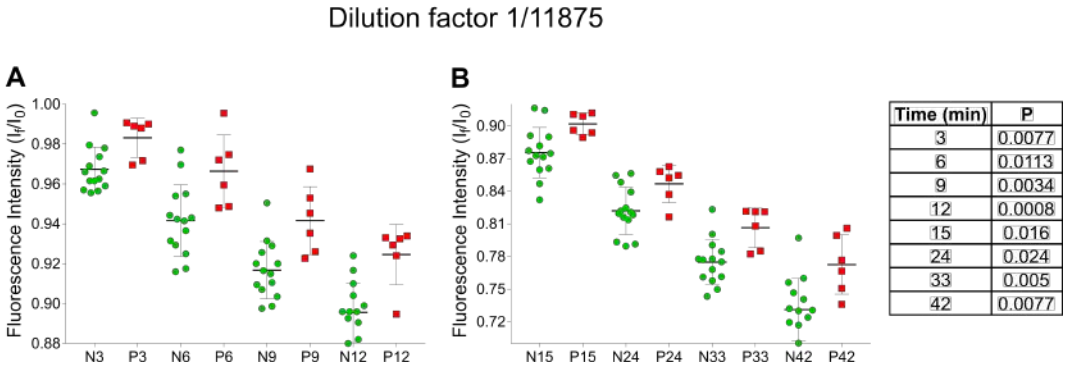

Time (min)	P
3	0.0077
6	0.0113
9	0.0034
12	0.0008
15	0.016
24	0.024
33	0.005
42	0.0077

Figure 4-11. Performance of the assay with sera throughout time (3-48 minutes). Dilution factor: 1/11875. 12 pre-COVID-19 samples (N) and 6 COVID-19 subjects (P) were assayed. **A.** Analysis from 3 to 12 minutes. **B.** Analysis from 15 to 42 minutes.

aration between the two groups starts to be more evident and the maximum separation in terms of the respective means of I_f / I_0 level was reached at 42 minutes. The P-values obtained with this dilution factor are lower from 12 minutes of analysis (< 0.0001) which was in good agreement with the previous dilution factor assessment. So, these results permit us to claim that the optimal dilution factor is around 1/12200. On the other hand, the optimal immunosensing time is 42 minutes which is in concordance with the best sensitivity for the detection of specific SARS-CoV-2 antibodies.[10]

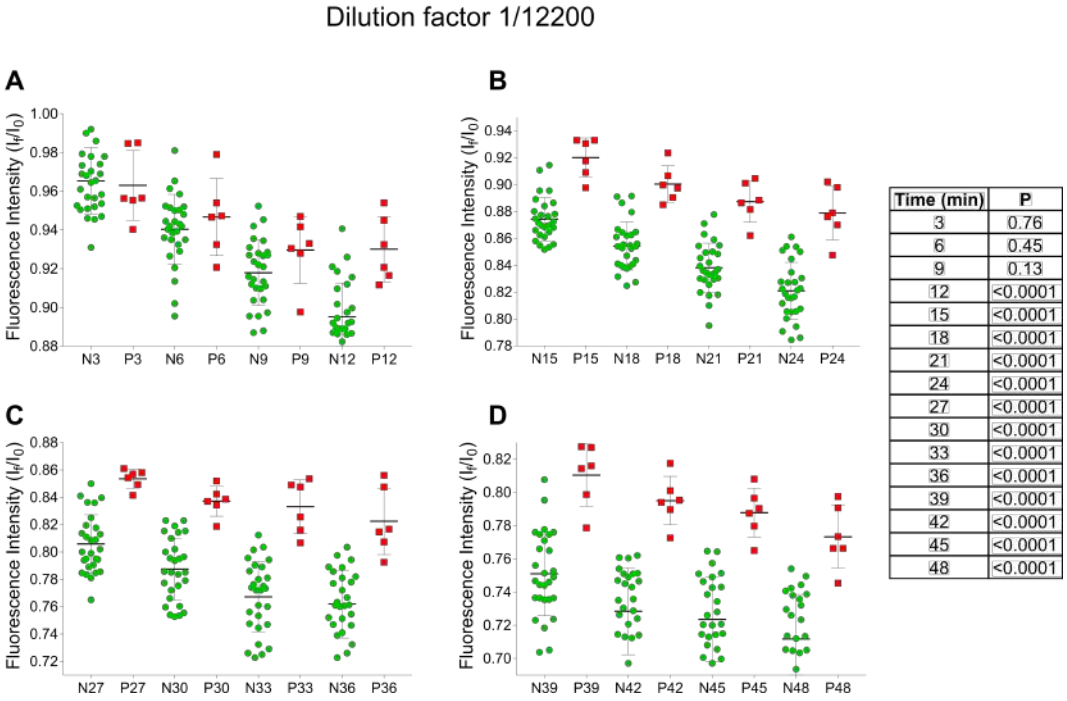

Time (min)	P
3	0.76
6	0.45
9	0.13
12	<0.0001
15	<0.0001
18	<0.0001
21	<0.0001
24	<0.0001
27	<0.0001
30	<0.0001
33	<0.0001
36	<0.0001
39	<0.0001
42	<0.0001
45	<0.0001
48	<0.0001

Figure 4-12. Performance of the assay with sera throughout time (3-48 minutes). Dilution factor: 1/12200. 28 pre-COVID-19 samples (N) and 6 COVID-19 subjects (P) were assayed. **A.** Analysis from 3 to 12 minutes. **B.** Analysis from 15 to 24 minutes. **C.** Analysis from 27 to 36 minutes. **D.** Analysis from 39 to 48 minutes.

We established an I_f / I_0 around 0.767 as a threshold to determine a positive or negative result at optimal immunosensing time (42 minutes), and no false negative/positive were determined, as shown in the figure 4-13. The threshold was calculated as the average of

the higher I_f / I_0 value of pre-COVID-19 samples and the lower I_f / I_0 value of COVID-19 samples. Thus, we can argue that the immunosensing platform proposed is suitable for the qualitative detection of antibodies against SARS-CoV-2 in serum samples. However, a limiting factor is that the specific detection of COVID-19 antibodies in serum samples through this approach may be restricted due to cross-reactivity with other antibodies for instance IgA or IgM which are also present in the serum samples. The direct comparison of serum samples (in optimal biosensing conditions) with the calibration curve, as done in figure 4-8 for Hsp72, was not possible since all the serum samples from COVID-19 subjects yielded I_f / I_0 values exceeding the dynamic range of the optimized calibration curve. So, we attributed the last fact to the cross-reactivity with other immunoglobulins present in serum samples whereas the calibration curve was solely performed with SARS-CoV-2 Spike RBD antibodies (immunoglobulins G).

4.4 Conclusions

The developed immunosensing platform can operate for the detection of several clinically relevant proteins. Particularly, this fact was demonstrated through the utilization of the GO-based immunosensing platform for the detection of H-IgG, PSA, Hsp72, and SARS-CoV-2 Spike RBD Antibodies. Furthermore, diverse configurations of the biosensing probe can be done for instance FITC or Streptavidin-QDs conjugate with antibodies (for the immunosensing of proteins), or FICT conjugated with recombinant proteins (for the immunoassay of antibodies), as far as we are concerned, has not been demonstrated to operate as biosensing probe when incubated in GO-coated surfaces. Additionally, the GO-based immunosensing platform can be used for the qualitative immunosensing in real samples as was demonstrated in the assay of urinary Hsp72 samples from patients diagnosed with AKI, even at different stages of AKI disease, or the determination of COVID-19 seroconversion from human serum samples with statistical significance. Lastly, our method has some advantages compared with the gold standard immunoassay method ELISA which are resumed in table 4-5.

Table 4-5. Some advantages of our method regarding the ELISA technique.

Feature	ELISA	Our method
Antibodies needed	At least two	one
Steps involve	Blocking, separation and washing	One step
Time	Around 6 hours	Around 2 hours
Interrogation	At the end	Real-time
LOD	∼pg-ng mL^{-1}	∼pg-ng mL^{-1}

4.5 References

1. Waikar, S. S.; Curhan, G. C.; Wald, R.; McCarthy, E. P.; Chertow, G. M. Declining Mortality in Patients with Acute Renal Failure, 1988 to 2002. J. Am. Soc. Nephrol. 2006, 17 (4), 1143. https://doi.org/10.1681/ASN.2005091017.

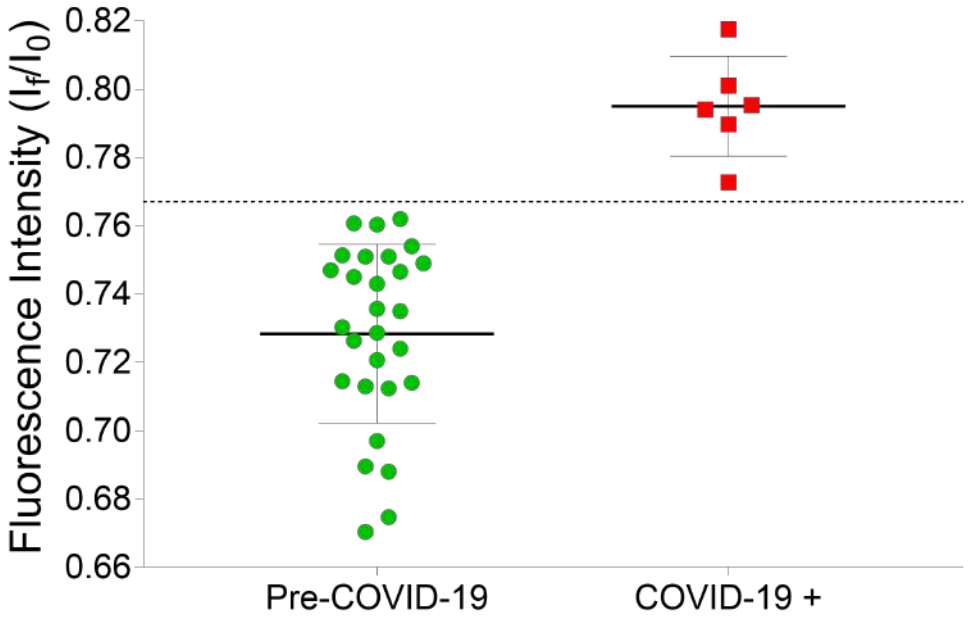

Figure 4-13. Dilution factor of 1/12200. Photoluminescent behavior of F-RBD incubated with diluted serum samples in GO-covered surfaces at 42 minutes of assay. The dotted line represents the threshold I_f / I_0 level calculated as the average of the higher I_f / I_0 value of pre-COVID-19 samples and the lower I_f / I_0 value of COVID-19 samples.

2. Bagshaw, S. M. Diagnosis and Classification of AKI: AKIN or RIFLE? Nature Reviews Nephrology 2010, 6 (2), 71–73. https://doi.org/10.1038/nrneph.2009.225.

3. Lopes, J. A.; Fernandes, P.; Jorge, S.; Gonçalves, S.; Alvarez, A.; Costa e Silva, Z.; França, C.; Prata, M. M. Acute Kidney Injury in Intensive Care Unit Patients: A Comparison between the RIFLE and the Acute Kidney Injury Network Classifications. Critical Care 2008, 12 (4), R110. https://doi.org/10.1186/cc6997.

4. Barrera-Chimal, J.; Pérez-Villalva, R.; Cortés-González, C.; Ojeda-Cervantes, M.; Gamba, G.; Morales-Buenrostro, L. E.; Bobadilla, N. A. Hsp72 Is an Early and Sensitive Biomarker to Detect Acute Kidney Injury. EMBO Molecular Medicine 2011, 3 (1), 5–20. https://doi.org/10.1002/emmm.201000105.

5. Lianos, G. D.; Alexiou, G. A.; Mangano, A.; Mangano, A.; Rausei, S.; Boni, L.; Dionigi, G.; Roukos, D. H. The Role of Heat Shock Proteins in Cancer. Cancer Letters 2015, 360 (2), 114–118. https://doi.org/10.1016/j.canlet.2015.02.026.

6. Murphy, M. E. The HSP70 Family and Cancer. Carcinogenesis 2013, 34 (6), 1181–1188. https://doi.org/10.1093/carcin/bgt111.

7. Pérez-Villalva, R.; Barrera-Chimal, J.; Aguilar-Carrasco, J. C.; Lima-Posada, I.; Cruz, C.; Ramírez, V.; González-Bobadilla, Y.; Uribe, N.; Trumper, L.; Bobadilla, N. A. HSP72 Is an Early Biomarker to Detect Cisplatin and Acetaminophen Nephrotoxicity. Biomarkers 2017, 22 (6), 548–556. https://doi.org/10.1080/1354750X.2017.1315616.

8. Morales-Narváez, E.; Dincer, C. The Impact of Biosensing in a Pandemic Outbreak: COVID-19. Biosensors and Bioelectronics 2020, 163, 112274. https://doi.org/10.1016/j.bios.2020.112274.

9. Drobysh, M.; Ramanaviciene, A.; Viter, R.; Chen, C.-F.; Samukaite-Bubniene, U.; Ratautaite, V.; Ramanavicius, A. Biosensors for the Determination of SARS-CoV-2 Virus and Diagnosis of COVID-19 Infection. International Journal of Molecular Sciences 2022, 23 (2). https://doi.org/10.3390/ijms23020666.

10. Avila-Huerta, M. D.; Ortiz-Riaño, E. J.; Mancera-Zapata, D. L.; Cortés-Sarabia, K.; Morales-Narváez, E. Facile Determination of COVID-19 Seroconversion via Nonradiative Energy Transfer. ACS Sens. 2021, 6 (6), 2136–2140. https://doi.org/10.1021/acssensors.1c00795.

11. Amanat, F.; Stadlbauer, D.; Strohmeier, S.; Nguyen, T. H. O.; Chromikova, V.; McMahon, M.; Jiang, K.; Arunkumar, G. A.; Jurczyszak, D.; Polanco, J.; Bermudez-Gonzalez, M.; Kleiner, G.; Aydillo, T.; Miorin, L.; Fierer, D. S.; Lugo, L. A.; Kojic, E. M.; Stoever, J.; Liu, S. T. H.; Cunningham-Rundles, C.; Felgner, P. L.; Moran, T.; García-Sastre, A.; Caplivski, D.; Cheng, A. C.; Kedzierska, K.; Vapalahti, O.; Hepojoki, J. M.; Simon, V.; Krammer, F. A Serological Assay to Detect SARS-CoV-2 Seroconversion in Humans. Nature Medicine 2020, 26 (7), 1033–1036. https://doi.org/10.1038/s41591-020-0913-5.

12. Cady, N. C.; Tokranova, N.; Minor, A.; Nikvand, N.; Strle, K.; Lee, W. T.; Page, W.; Guignon, E.; Pilar, A.; Gibson, G. N. Multiplexed Detection and Quantification of Human Antibody Response to COVID-19 Infection Using a Plasmon Enhanced Biosensor Platform. Biosensors and Bioelectronics 2021, 171, 112679. https://doi.org/10.1016/j.bios.2020.112679.

Chapter 5

Determination of protein-binding constants via the developed immunosensing system

Determination of macromolecular association is of fundamental importance in diverse fields of biomedical science such as drug development, gene editing, and diagnostics. Therefore, the measurement of the mentioned binding constants is also important in the biosensing field. Surface plasmon resonance is the technique widely used for the determination of macromolecular interactions since it permits monitoring, in real-time, association and dissociation processes. Herein, we demonstrated that the fluorescence quenching-based immunosensing platform developed can be implemented also to monitor the association process occurring between proteins, and therefore, determine binding kinetic constants. We described all procedures performed to the determination of protein-binding constants of three pairs of proteins including (i) H-IgG and fluorophore-labeled anti-H-IgG, (ii) PSA and QDs-labeled anti-PSA, and (iii) antibodies against SARS-CoV-2 and fluorophore-labeled SARS-CoV-2 spike receptor-binding domain recombinant protein.

5.1 Introduction

5.1.1 The practical relevance of binding kinetic constants

Measurement of binding kinetic constants is crucial in diverse biomedical applications such as biosensing, where antibodies are employed, so antibody affinity is fundamental in quality control to ensure high sensitivity during analyte detection;[1] in drug discovery, the pharmacological effect/mode of action is determined through the specific association of a drug with its respective receptor;[2] in biochemistry, the understanding of structure/function relationships are in function of protein-protein interactions;[3] in diagnostics, the validation of potential biomarkers is made in terms of binding kinetics parameters.[4] In general, binding kinetic constants are determined from ligand-binding type experiments where saturation is often reached and the concentration of one reactant is varied.[3] Quantitative analysis of binding kinetics constants is very important since it accounts for

the strength of the resulting binding and determines the affinity of such interaction.

Protein-protein association and dissociation rate constants are typically determined using SPR, a highly sensitive label-free technique, which allows for the real-time monitoring of the binding event occurring in an immunoreaction (ex. antibody-antigen).[5] However, SPR technology possesses some limitations; for instance, (i) external factors (such as temperature) may alter the refractive index and so contribute to false-positive signals, (ii) the kinetic analysis can be affected by mass transport, (iii) inappropriate orientation of the ligand onto the surface of sensor chip may hinder the analyte binding,[6] and (iv) the instrumentation and biochips, in general, are expensive. High-performance affinity chromatography is another technique used to study binding interactions in which the affinity column can be reused for several experiments, which is an important advantage of this technique.[7] However, the binding requires the immobilization of the biorecognition element, and therefore, validation protocols are needed to ensure that the protein association happened correctly. Many other techniques have been used for the measurement of binding kinetic constants. Table 5-1 summarizes these techniques, and also the advantages and limitations of each method are mentioned.

5.1.2 The operational principle for measurement of binding kinetic constants

GO, which is an excellent quencher of fluorescence, has been observed to exhibit a high affinity with proteins that are not forming immunocomplexes.[8] Hence, the fluorescence intensity of F-Ab (fluorophore-labeled protein) (a donor) can be strongly quenched when F-Ab is incubated within GO-covered microwell surfaces (an acceptor) via non-radiative energy transfer (a phenomenon efficiently occurring when the distance between donor and acceptor is below 20 nm).[9] However, the formation of immunocomplexes involves non-covalent intermolecular interactions such as hydrogen bonding, electrostatic interactions, hydrophobic, and Van der Waals forces.[10] We hypothesize that such intermolecular interactions hinder the affinity between immunocomplexes and GO-covered microwell surfaces, and as a consequence, in the proposed biosensing platform, the aforementioned non-radiative energy transfer is not efficient upon immunocomplexes development. Moreover, the analyte acts as a spacer between F-Ab and the GO-covered microwell surface, hence, upon immunocomplexes formation, the distance between donor and acceptor does not facilitate non-radiative energy transfer. In other words, the F-Ab remain highly fluorescent during protein association, whereas F-Ab that are not associated with their counterparts are quenched by GO. Thus, this approach is intended for the assessment of the association phase occurring between two proteins. Particularly, we determined the binding kinetic constants of three pairs of proteins: the interaction of (i) human immunoglobulin G (H-IgG) with fluorophore-labeled Anti-H-IgG, (ii) Prostate-Specific Antigen (PSA) with quantum dot-labeled Anti-PSA, and (iii) Anti-RBD with fluorophore-labeled SARS-CoV-2 spike receptor-binding domain recombinant protein.

Table 5-1. Overview of different methods for the determination of protein kinetics.

Analytical technique	Label	Advantages	Limitations	Experimental steps	Ref
SPR	Free	Real-time measurements. Highly sensitive. Small volume and sample are needed	Mass transport. Bulky and expensive instrumentation. Non-specific binding to surfaces.	Ligand immobilization, blocking steps, and sample injection. Glass surface coated with inert metal (gold).	6
Bio-layer interferometry	Free	Real-time measurement. Allows for the measurement of binding properties in crude samples, complex matrices, and/or solvents.	Require special instrumentation. it can only be applied to peptides that present specific types of amino acids in their sequence.	Multiple washing and blocking steps. Ligand immobilization.	11
Acoustic device	Free	Real-time measurements. The microfluidic module for multi-sample integration, rapid analysis, and reduced sample consumption. Easy to assemble and use.	SAW sensors are sensitive to a variety of parameters. The sensing system may not work efficiently due to in biological solution the intensity of acoustic waves can decrease.	Require special materials such as gold, quartz, and polydimethylsiloxane for the chip configuration.	12

Electro-chemical	Free	Good reproducibility and sensitivity Easy to assemble and use. The small amplitude perturbation from the steady state makes it a non-destructive technique.	Several requirements are needed to obtain a valid impedance spectrum. The accuracy of EIS measurement depends not only on the technical precision of the instrumentation but also on the operating procedures	Needs specific surface architecture Such as electrodes coated with gold. Diverse washing, electrochemical polishing, and blocking steps.	13,14
Capacitive	Free	Portability, rapidity, and real-time measurement.	Needs specific surface architecture. Instability to detect small molecules, reusability, and sufficient stability for repetitive measurements. Lack of sufficient selectivity for application in real samples.	Needs specific surface architecture Such as electrodes coated with gold. Diverse washing, electrochemical polishing, and blocking steps.	14

Optical fiber	GO	High compactness and potential miniaturization. High compatibility with optoelectronic devices. Multiplexing and remote measurement capability as the signal is spectrally modulated.	Measurement accuracy is limited because of its broad line width at full-width at half maximum. Needs specific surface architecture. Require special instrumentation.	Photosensitive silicate fiber whose core is doped with germanium. Several washing steps.	15,16
Chromogenic assay	Peptide labeling	Good specificity in complex matrices.	Require special instrumentation, and in general, is very expensive. Complicated procedures.	Diverse washing and blocking steps.	17
Micromechanical resonators	Free	Extreme sensitivity, fast response, low cost, and the small amount of sample required for operation.	Non-specific absorption makes measurement interpretation difficult.	Diverse washing and blocking steps. Gold and silicon nitride are used on the surface chip. Ligand immobilization.	18

Chemiluminescent	Free	Real-time measurement. Simple manipulation, low cost, and high speed. It avoids the decrease of affinity resulting from steric hindrance, occupation of the antigenic determinants, and deactivation of antibodies.	Lack of sufficient selectivity and sensitivity to various physicochemical factors. CL emission intensities are sensitive to a variety of environmental factors such as temperature, solvent, ionic strength, pH, and other species present in the system.	Diverse washing and blocking steps.	19
Photoluminescence	ZnO-nanorods	Good sensitivity. Portable immunosensor.	Needs specific surface architecture. Complicated procedures	The glass surface is coated with ZnO-nanorods and protein A. Ligand immobilization.	20
Fluorescence	Fluorescence labeling	High sensitivity, accuracy, and rapidity.	Require special instrumentation. Complicated procedures.	Few optical components are needed due to the use of SMFC. Multiple cleaning and blocking steps.	21

Ellipsometry	Free	High sensitivity and accuracy.	Require special instrumentation. Complicated procedures.	Gold and Chromium are used on the surface chip Multiple cleaning and blocking steps.	22
Fluorescence	Fluorescence labeling	Real-time and in vivo measurements. Good sensitivity.	Cumbersome procedures	Diverse washing and blocking steps.	23
Radioligand	Radioligand labeling	Sensitivity and minimal modification of the chemical structure of the ligand. Non-destructive technique.	Every compound of interest must be custom synthesized and labeled with a radioisotope which is cost and time prohibitive.	Multiple incubation and blocking steps.	24
Isothermal titration	Free	Allows for the measurement of binding properties in crude samples, complex matrices, and/or solvents	A large amount of sample is needed. It is a slow technique with low throughput.	Multiple washing and blocking steps.	25
Fluorescence quenching	Fluorescence labeling	Real-time measurements. High sensitivity, accuracy, and rapidity. low cost and a small amount of sample required for operation.	Requires special instrumentation such as a microplate reader.	Single-step immunosensing.	This work

5.2 Experimental section

The experimental protocols for the immunoassays targeting H-IgG and PSA are described in the experimental section of Chapter three, and for immunoassays of Hsp72 and antibodies against SARS-CoV-2 such experimental protocols are mentioned in Chapter four.

5.2.1 Immunoassay

Generally, 100 µL of the biosensing probe and 100 µL of the protein counterpart were added. FITC-Anti-H-IgG was added at a final concentration of 0.125 µg mL^{-1}, QD-Anti-PSA was added at a final concentration of 0.028 µg mL^{-1}, and F-RBD was added at a final concentration of 0.06 µg mL^{-1}. The liquid was then mixed to homogenize the content of the microwells. Afterward, the intensity of fluorescence is recorded by interrogating the fluorescence in each microwell every 5 minutes via a kinetic analysis of two hours. In general, seven serial dilutions of the protein counterpart were analyzed. Blank samples were also assayed as a control in each immunoassay. All the experiments were carried out in the microplate reader Cytation 5 (Biotek), at room temperature.

5.2.2 Open-source software

We also developed a graphical User Interface (GUI) in python for the determination of Binding kinetics constants. The data resulting from the association process is loaded in the GUI and automatically the binding constants can be calculated. Our software to determine binding kinetic constants of proteins is publicly available via `https://github.com\/BioNanosensors/GUI-Kinetics-Protein.git`. All the details related to the installation and operation of this software are available in the same link.

5.3 Results and discussion

5.3.1 The theoretical model of binding kinetic constants

As depicted in table 5-1, many techniques have been used for the determination of the affinity and kinetics of an interaction between two biomolecules. The affinity describes how strong the interaction is between two biomolecules, and is expressed via the equilibrium dissociation constant K_D.[3] This parameter is the concentration of ligand at which half the ligand-binding sites on the protein are occupied in the system at equilibrium (In a biochemical reaction, equilibrium is the state in which the proteins, ligands, and protein-ligand complexes are at a point where there is no observable change in the properties of the system), and it is defined as

$$K_D = \frac{K_d}{K_a} \tag{5-1}$$

hence, the smaller the K_D, the greater the affinity between biomolecules. On the other hand, kinetic is related to how fast the interaction happens (the association rate

constant K_a), and also how specific the interaction is between two biomolecules (the dissociation rate constant K_d).[26] The association rate constant describes the rate at which the forward reaction is taking place so that the protein-ligand complex is formed. This rate is dependent on the concentration of the protein and ligand and it is measured in terms of M^{-1} s^{-1}. On the contrary, the dissociation rate constant describes the rate of the backward reaction depicting the rate at which the complexes dissociate into separate proteins and ligands. This rate is independent of the concentration of the free proteins and ligands in the system, and it is measured in s^{-1}.

Following the model proposed by Oshannessy and colleagues,[27] the interaction between a protein P and its respective antibody L can be described as,

$$L + P \leftrightarrow LP \tag{5-2}$$

so, the rate of formation of the product, LP, at time t is described as follows

$$\frac{d[LP]}{dt} = K_a[L][P] - K_d[LP] \tag{5-3}$$

after some reaction time, P = [P_0] – [LP] so Eq 5-3 can be written as

$$\frac{d[LP]}{dt} = K_a[L]([P_0] - [LP]) - K_d[LP] \tag{5-4}$$

where P_0 is the initial concentration of protein at time t = 0. The observed signal R is proportional to the formation of immunocomplexes LP. In our immunosensing platform, R is the signal provided by the respective quenching of fluorescence (for example, the signal provided by the interaction (immunocomplex formation) of an analyte concentration and its respective fluorophore-labeled antibody). R_{max} is the maximum value of the explored signal, that is, in our particular case, the maximum quenching of fluorescence reached by the blank sample. So, we have that

$$\frac{dR}{dt} = K_a[C]([R_{max} - R] - K_d[R] \tag{5-5}$$

C is the concentration of the respective analyte and dR/dt is the rate of immunocomplexes formation (biosensing probe-analyte). [R_{max}– R] is equivalent to the number of unoccupied binding sites in the biosensing probe. Rearranging equation 5-5 we have that

$$\frac{dR}{dt} = CK_aR_{max} - (CK_a + K_d)R \tag{5-6}$$

Rearranging,

$$\int dt = \int \frac{dR}{CK_aR_{max} - (CK_a + K_d)R} \tag{5-7}$$

Integrating we obtained the following expression for R

$$R = \frac{CK_aR_{max}(1 - e^{-(CK_a+K_d)t})}{CK_a + K_d} \tag{5-8}$$

From this expression, it is difficult to calculate K_a and K_d since both are unknown. So, defining k_s as

$$k_s = CK_a + K_d \tag{5-9}$$

Equation 5-8 takes the form

$$R = \frac{CK_aR_{max}(1 - e^{-k_st})}{k_s} \tag{5-10}$$

Finally, we obtained an expression to calculate K_a

$$K_a = \frac{k_sR}{CR_{max}(1 - e^{-k_st})} \tag{5-11}$$

And so, K_d can be determined from equation 5-9. Through our fluorescence quenching-based immunosensing platform the association process is followed, for this reason, the association rate constant can be directly determined and K_d and K_D are calculated from equations 5-9 and 5-1, respectively.

5.3.2 Development and operation of GUI

Important Note: This application was developed in collaboration with Dr. Fernando Arce-Vega at Centro de Investigaciones en Óptica.

The first steps consist in load the file (.xlsx or .csv) with R values measured at given intervals. Figure 5-1 shows how the information used by the GUI should be organized. In the first column, the values of time must be in seconds. Then, the next columns contain the measurements of R, which is represented by the quenching of fluorescence in our biosensing platform, and the ultimate row contains the information of analyte concentrations in molar units. Therefore, each column includes the quenching signal R for every reading time and the respective analyte concentration.

When the user clicks on the calculate button, the application computes the calibration curves of the quenching signals R finding a mathematical model that fits the data provided. Given the exponential nature of quenching signals R, the one-phase association model was used, which is described by the following equation:

$$R_t = R_0 + (Plateau - R_0)(1 - e^{k_st}) \tag{5-12}$$

where R_t is the quenching signal expressed in arbitrary units, Plateau is the R-value at infinite times, k_s is the rate constants (expressed in reciprocal of the X-axis time units, If X is in seconds, then K is expressed in inverse seconds), and R_0 is the value of R at time 0. The optimization algorithm used by the GUI to fit the curves and determine the plateau, k_s, and R_0 variables is the Lavender-Marquardt,[28] which is implemented

in the SciPy library.[29] The algorithm iteratively adjusts these variables to reduce the least-squares function:

	Time (S)	Meas_1	Meas_2	Meas_3	Meas_4	Meas_5	Meas_6	Meas_7
2	300	0.112192	0.1095233	0.098531	0.0890977	0.0799177	0.0976597	0.0807645
3	600	0.1971515	0.1711907	0.160895	0.1555717	0.145995	0.1455947	0.121252
4	900	0.2483995	0.2332323	0.216382	0.2025547	0.1983523	0.1734133	0.175542
5	1200	0.3068355	0.274749	0.264633	0.2375463	0.22685	0.2216697	0.2097615
6	1500	0.356465	0.3280603	0.29083	0.2726927	0.2632017	0.2337083	0.2303085
7	1800	0.394989	0.3626927	0.3339237	0.3022083	0.2915883	0.2706557	0.2558145
8	2100	0.4302315	0.3869373	0.3567803	0.3313213	0.3152287	0.2872803	0.2860345
9	2400	0.4560605	0.4165877	0.385338	0.3463717	0.3424807	0.3175633	0.3071695
10	2700	0.484378	0.4379753	0.4002817	0.3637757	0.3538693	0.3496583	0.307469
11	3000	0.505222	0.4588583	0.4173983	0.3858613	0.3692753	0.3574277	0.333716
12	3300	0.5174805	0.4786087	0.4316513	0.4034693	0.3902247	0.37435	0.3466985
13	3600	0.5439355	0.4910373	0.458853	0.4223183	0.4077237	0.3810993	0.3675085
14	3900	0.5534185	0.5117567	0.4647453	0.4349557	0.4200387	0.3936297	0.382201
15	4200	0.5750415	0.532996	0.478162	0.443591	0.42707	0.4066177	0.3848035
16	4500	0.5798825	0.5379923	0.4995123	0.4605717	0.445451	0.428745	0.403744
17	4800	0.5813655	0.553968	0.505325	0.46156	0.451394	0.4400233	0.4065235
18	5100	0.5975155	0.568747	0.518314	0.4787333	0.4688517	0.456244	0.421718
19	5400	0.6194915	0.5786207	0.526928	0.490222	0.4785183	0.469735	0.432974
20	5700	0.6180955	0.5792723	0.535964	0.5019673	0.48325	0.4766513	0.433334
21	6000	0.6251405	0.5856827	0.5404733	0.5036897	0.5053583	0.480837	0.43986
22	6300	0.6333375	0.5969217	0.539253	0.516599	0.492494	0.4899243	0.454772
23	6600	0.641805	0.5994523	0.5577853	0.518964	0.5130523	0.5151287	0.460094
24	6900	0.643989	0.602788	0.5690597	0.527608	0.507148	0.508853	0.4748365
25	7200	0.6539065	0.6239033	0.581978	0.5354263	0.5250897	0.516583	0.4801465
26	7500	0.657842	0.636425	0.585474	0.538567	0.5168463	0.524683	0.4827005
27	C (M)	0	6.25E-11	2.50E-10	5.00E-10	1.00E-09	2.00E-09	4.00E-09
28	C (ng mL^{-1})	0	9.37	37.5	75	150	300	600

Figure 5-1. Organization of the information for the determination of binding kinetic constants through the GUI.

$$armin_{\beta} \sum_{i=1}^{n} [R_i - f(t_i, \beta)]^2 \tag{5-13}$$

where β are the arguments plateau, k_s, and R_0 of the one-phase association function f, and n is the number of measurements. Once these variables have been calculated, the application displays on the right widget a figure with the calibration curves in continuous lines and dashed lines for the R signals and saves a .png image inside the output folder. In addition, the application displays on the left widget the parameters obtained from the one-phase association model and the R^2 metric of the predictions regarding the R signals using the scikit-learn librar,[30] then the application saves these values in the text file. After the Plateau, k_s, and R_0 variables have been obtained for all the signals, the next step of the application is to calculate the Span and R_{max} variables. Span is a vector composed of the difference between R_0 and Plateau signals, and R_{max} is the maximum value of the Span vector computed as:

$$span = R_0 - Plateau$$

$$R_{max} = max(span)$$

So, the GUI calculates the binding kinetic constants from equations 5-1, 5-9, and 5-11. Finally, the application computes the absolute error to determine the relative error of measurements using the equations:

$$Err_{abs} = \sqrt{\frac{\sum_{i=1}^{n}[A_i - \bar{A}]^2}{n(n-1)}} \tag{5-14}$$

$$Err_{rel} = \frac{Err_{abs}}{\bar{A}} \tag{5-15}$$

Err_{abs} is the absolute error of the measurements, Err_{rel} is the relative error of the measurements, $\bar{A}$ is the average of measurements A, and n the number of measurements. The relative error of the measurements is expressed in parentheses using a plus-minus symbol $\pm$ in the graphical interface. Finally, this information is displayed in the left widget and saved in the text file, along with the time in seconds that the process of determining the binding kinetic constants required. The procedure for the installation of GUI is described in detail at `https://github.com/BioNanosensors/GUI-Kinetics-Protein.git`.

5.3.3 Determination of binding kinetic constants for H-IgG

According to the operational principle of the proposed immunosensing platform (described in section 5.1.2.), we employed the quenching signal R as the indicator of the association between a protein P and an antibody L. Figure 5-2a depicts the row data obtained (under optimal biosensing conditions) for the detection of H-IgG. The fluorescence intensity I_f/I_0 decreases throughout the kinetics analysis, and therefore, the quenching signal increases, see figure 5-2b. The quenching signal is obtained through the transformation R = (1 - I_f/I_0), where I_f is the fluorescence intensity in the studied microwell at time f and I_0 is the intensity of fluorescence in the explored microwell at time 0. Therefore, R values close to 1 suggest a strong quenching of fluorescence, and on the contrary, R values close to 0 indicate a weak quenching phenomenon. We concluded that the quenching of fluorescence is inversely proportional to the analyte concentration, that is the lower the analyte concentration, the higher the R values. Following this, R_{max} is then reached by blank samples (no analyte).

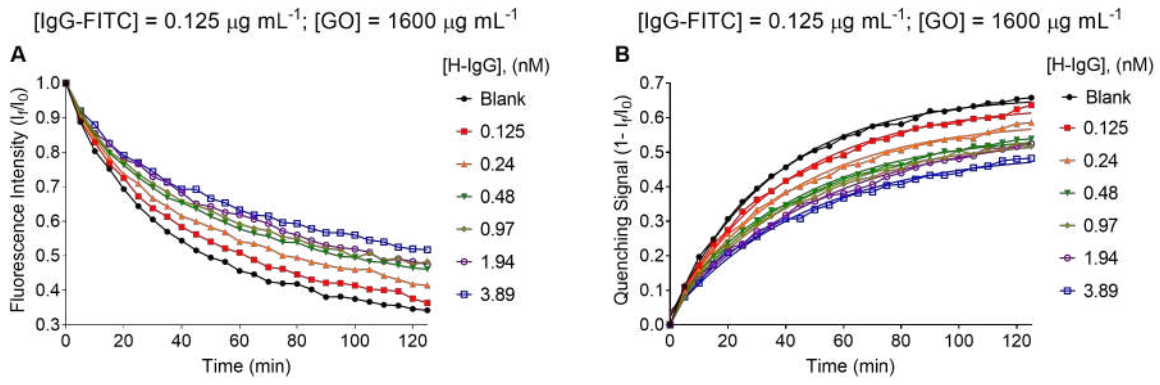

Figure 5-2. **A.** Raw data of the interaction between H-IgG and F-Anti-H-IgG. **B.** Association curves for the measurement of H-IgG binding constants.

Obtaining typical association curves for H-IgG, through GUI developed we obtained the parameters of the one-phase association fitting which are shown in table 5-2. The

analyte concentrations used in the experiments were transformed to molarity because of the units of binding constants.

Table 5-2. Parameters resulting from the one-phase association, human immunoglobulin G (H-IgG) – fluorophore-labeled Anti-H-IgG.

Concentration (ng mL^{-1})	**Blank**	**9.37**	**37.5**	**75**	**150**	**300**	**600**
Molarity (nM)	Blank	0.125	0.24	0.48	0.97	1.94	3.89
R0	0.022	0.027	0.029	0.029	0.025	0.038	0.027
Plateau	0.664	0.64	0.593	0.556	0.542	0.568	0.504
Ks (s^{-1})	0.028	0.025	0.024	0.024	0.023	0.019	0.021
R^2	0.997	0.996	0.995	0.995	0.995	0.994	0.994

So, the GUI has all parameters necessary to calculate the binding kinetic constants K_a , K_d and K_D. The values of such constants for every H-IgG concentration are resumed in table 5-3. The average value of K_D represent the affinity of anti-H-IgG to H-IgG. As seen in table 5-3, each binding constant was computed with its respective error.

Table 5-3. Binding kinetic constants of H-IgG – fluorophore-labeled Anti-H-IgG.

[H-IgG]; (nM)	**K_a(M^{-1}s^{-1})**	**K_d(s^{-1})**	**K_D(M)**
0.125	2.93 x10^{08} ($\pm$0.06)	6.9 x10^{-03} ($\pm$0.16)	4.15 x10^{-11} ($\pm$0.32)
0.24	6.52 x10^{07} ($\pm$0.06)	8.1 x10^{-03} ($\pm$0.12)	2.02 x10^{-10} ($\pm$0.29)
0.48	2.91 x10^{07} ($\pm$0.06)	8.97 x10^{-03} ($\pm$0.1)	4.79 x10^{-10} ($\pm$0.27)
0.97	1.39 x10^{07} ($\pm$0.06)	9.31 x10^{-03} ($\pm$0.09)	1.05 x10^{-09} ($\pm$0.27)
1.94	5.39 x10^{06} ($\pm$0.07)	7.78 x10^{-03} ($\pm$0.09)	2.15 x10^{-09} ($\pm$0.22)
3.89	2.88 x10^{06} ($\pm$0.06)	9.76 x10^{-03} ($\pm$0.07)	5.03 x10^{-09} ($\pm$0.23)
Average	6.83 x10^{07} ($\pm$0.67)	8.47 x10^{-03} ($\pm$0.05)	1.49 x10^{-09} ($\pm$0.51)

The resultant K_D values were benchmarked with data found in the literature and the value provided by the respective bioreagent suppliers. So, for anti-H-IgG, the reported K_D range from 2 to 13 nM whereas the value of K_D obtained with our fluorescence quenching-based immunosensing platform was 1.49 nM, see table 5-4. Bioreagent suppliers do not provide any K_D value for anti-H-IgG. Table 5-4 also brings information regarding the methods employed to the determination of K_D.

Table 5-4. K_D reported values in the literature for anti-H-IgG associations.

K_D (nM)	**2**	**4.2**	**13.26**	**5**	**12**	**1.49**
Detection Method	SPR	SPR	Photonic Crystal-sensor	SPR	Difference interferometer	Quenching of fluorescence
Reference	31	32	33	34	35	This work

5.3.4 Determination of binding kinetic constants for PSA

Figure 5-3a depicts the row data obtained (under optimal biosensing conditions) for the detection of PSA. The association process for each PSA concentration in terms of quenching signal $R=(1-I_f)/I_0$ is depicted in figure 5-3b.

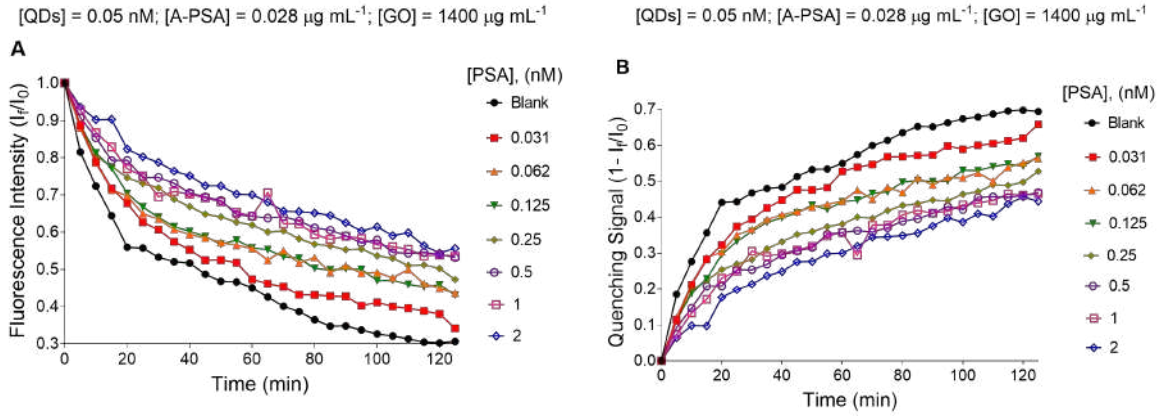

Figure 5-3. **A.** Raw data of the interaction between PSA and QDs-Anti-PSA. **B.** Association curves for the measurement of PSA binding constants.

Now through the GUI developed, the parameters of the one-phase association fitting are calculated which are shown in table 5-5. The PSA range was smaller than H-IgG, and the fluorophore used for the conjugation with Anti-PSA was QDs. Same way, PSA concentrations were transformed to molarity due to the units of binding constants.

Table 5-5. Parameters resulting from the one-phase association, PSA – QDs-labeled Anti-PSA.

Concentration (ng mL^{-1})	**Blank**	**0.15**	**0.32**	**0.62**	**1.25**	**2.5**	**5**	**10**
Molarity (nM)	Blank	0.031	0.062	0.125	0.25	0.5	1	2
R_0	0.081	0.033	0.039	0.035	0.06	0.048	0.033	0.022
Plateau	0.686	0.622	0.521	0.541	0.512	0.486	0.47	0.499
k_s(s^{-1})	0.032	0.031	0.037	0.031	0.023	0.021	0.024	0.016
R^2	0.957	0.986	0.962	0.978	0.974	0.977	0.952	0.984

So, the GUI has all parameters necessary for the calculation of binding kinetic constants which are presented in table 5-6. Each binding constant is computed with its respective error following the equations 5-14 and 5-15.

Table 5-6. Binding kinetic constants of PSA – QDs-labeled Anti-PSA.

[PSA]; (nM)	$K_a(M^{-1}s^{-1})$	$K_d(s^{-1})$	$K_D(M)$
0.031	8.06 x10^{08} (±0.05)	6.08 x10^{-03} (±0.23)	1.42 x10^{-11} (±0.39)
0.062	4.22 x10^{08} (±0.05)	1.08 x10^{-02} (±0.12)	3.64 x10^{-11} (±0.27)
0.125	1.77 x10^{08} (±0.05)	9.31 x10^{-03} (±0.13)	7.95 x10^{-11} (±0.28)
0.25	5.67 x10^{07} (±0.06)	8.73 x10^{-03} (±0.09)	2.08 x10^{-10} (±0.21)
0.5	2.32 x10^{07} (±0.06)	9.08 x10^{-03} (±0.07)	5.36 x10^{-10} (±0.21)
1	1.33 x10^{07} (±0.06)	1.04 x10^{-02} (±0.08)	1.15 x10^{-09} (±0.25)
2	3.91 x10^{06} (±0.07)	7.95 x10^{-03} (±0.07)	3.21 x10^{-09} (±0.23)
Average	2.14 x10^{08} (±0.54)	8.91 x10^{-03} (±0.06)	7.49 x10^{-10} (±0.58)

The K_D values for anti-PSA reported in the existing literature range from 0.23 to 21.7 nM, and the value reported by the bioreagent suppliers was 0.54 nM, see table 5-7. The K_D value calculated by the GUI was 0.74 nM, which is in the same order as that reported by the suppliers. Also, the detection methods used in each paper for the determination of binding kinetic constants are shown.

Table 5-7. K_D values reported in the literature for Anti-PSA association.

K_D(nM)	**0.23, 0.61**	**3.7**	**21.7, 17.5**	**0.5, 1.1, 0.3**	**0.54**	**0.74**
Antibody tested	P001D and P008P	A67-B/E3 (Used by us)	Ab10187 and Ab10185	60-8A2, 22-1A2 and 22-8A2	A67-B/E3	A67-B/E3
Manufacturer	The authors	Abcam	Abcam	The authors	Abcam	Abcam
Detection Method	SPR	Immunometric assay	SPR	Titration ELISA	OI-RD measurement	Quenching of fluorescence
Reference	36	37	38	39	Supplier	This work

5.3.5 Determination of binding kinetic constant for antibodies against SARS-CoV-2

The association curves of the interaction of antibodies against the RBD region of SARS-CoV-2 and F-RBD are depicted in figure 5-4. As mentioned previously, in this immunoassay configuration the RBD recombinant protein of SARS-CoV-2 is conjugated with fluorophore FITC and the antibodies against this recombinant protein are detected.

The results obtained from the one-phase association fitting, performed with the GUI, are shown in table 5-8. The range of concentrations of antibodies against SARS-CoV-2 are lower in order of pM.

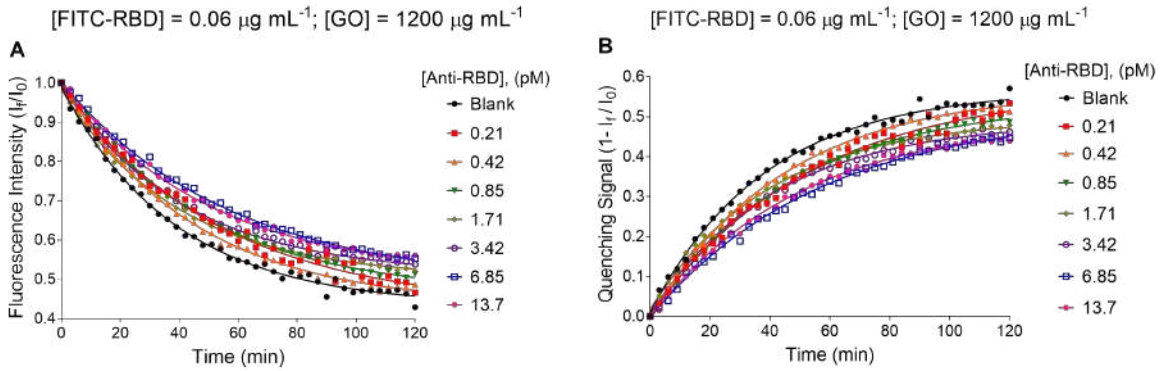

Figure 5-4. **A.** Raw data of the interaction between antibodies against SARS-CoV-2 (anti-RBD) and FITC-RBD. **B.** Association curves for the measurement of anti-RBD binding constants.

Table 5-8. Parameters resulting from the one-phase association, Anti-RBD – fluorophore-labeled SARS-CoV-2 spike receptor-binding domain recombinant protein.

concentration (ng ml^{-1})	**Blank**	**0.03**	**0.062**	**0.12**	**0.25**	**0.5**	**1**	**2**
Molarity (pM)	Blank	0.21	0.42	0.85	1.71	3.42	6.85	13.7
R_0	0.011	0.002	0.003	0.003	0.017	0.006	0.002	0.005
Plateau	0.568	0.574	0.567	0.538	0.497	0.489	0.514	0.494
K_s (s^{-1})	0.026	0.019	0.022	0.021	0.025	0.024	0.018	0.020
R^2	0.994	0.989	0.998	0.999	0.997	0.996	0.996	0.997

The values obtained of K_a, K_d and K_D for every analyte concentration are shown in table 5-9. The affinity of anti-RBD antibodies is high as evidenced by the average value of K_D.

Table 5-9. Binding kinetic constants of Anti-RBD–fluorophore-labeled SARS-CoV-2 spike receptor-binding domain recombinant protein.

[Anti-RBD]; (pM)	**K_a($M^{-1}s^{-1}$)**	**K_d(s^{-1})**	**K_D(M)**
0.21	5.79 x10^{10} (±0.06)	6.89 x10^{-03} (±0.1)	2.83 x10^{-13} (±0.31)
0.42	3.57 x10^{10} (±0.06)	7.3 x10^{-03} (±0.11)	5.05 x10^{-13} (±0.33)
0.85	1.6 x10^{10} (±0.06)	7.95 x10^{-03} (±0.09)	1.16 x10^{-12} (±0.31)
1.71	9.26 x10^{09} (±0.05)	9.27 x10^{-03} (±0.08)	1.82 x10^{-12} (±0.25)
3.42	4.22 x10^{09} (±0.06)	9.53 x10^{-03} (±0.08)	4.64 x10^{-12} (±0.31)
6.85	1.4 x10^{09} (±0.06)	7.97 x10^{-03} (±0.07)	1.37 x10^{-11} (±0.32)
13.7	8.27 x10^{08} (±0.06)	8.92 x10^{-03} (±0.07)	2.86 x10^{-11} (±0.41)
Average	1.76 x10^{10} (±0.45)	8.26 x10^{-03} (±0.04)	7.26 x10^{-12} (±0.54)

For antibodies against SARS-Cov-2, the K_D values reported in the literature range from nM order to pM order, see table 5-10. In addition, the supplier reports a K_D value of 6 pM, whereas our immunosensing platform measured a K_D value of 7.54 pM. Therefore, the K_D values measured through our approach are consistent with those of

existing literature and even with those provided by the manufacturers. Figure 5-5 depicts all the information provided by the GUI developed. On the right side, the calibration curves are represented by continuous lines, and dashed lines are the experimental data. On the top left side, the parameters obtained from the one-phase association model, and on the bottom left side the binding kinetic constants, with their respective errors, and the coefficient of determination R^2 are presented.

Table 5-10. K_D reported values in the literature for the association of antibodies against the SARS-CoV-2 spike receptor-binding domain.

K_D(nM)	**0.996, 3.34, 5,17**	**0.027**	**0.006**	**0.00754**
Antibody tested	5F8, 3F11 and 2F2	CT-P59	40592-R001	40592-T62
Manufacturer	The authors	The authors	Sino Biological	Sino Biological
Detection Method	SPR	SPR	Octet RED System	Quenching of fluorescence
Reference	40	41	Sino Biological	This work

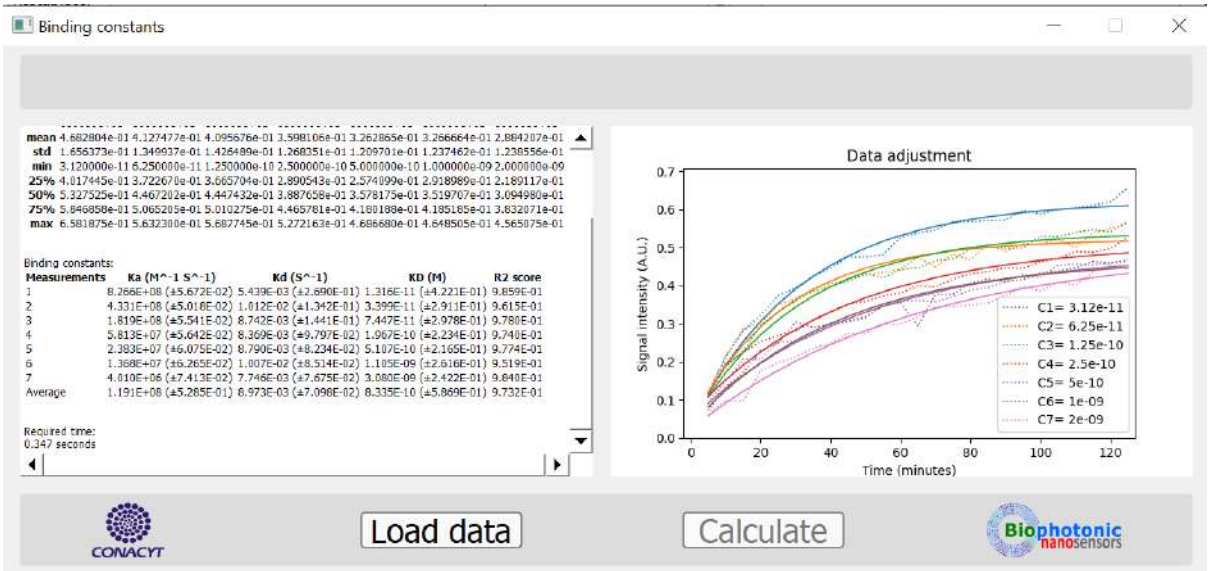

Figure 5-5. Parameters calculated by the GUI. The application was developed by Dr. Fernando Arce Vega.

5.3.6 Determination of the inter-assay variability in the measurement of binding kinetic constants

Intending to validate our approach at the interassay level, we assessed the variability of our immunosensing platform for the determination of binding kinetics constants. The experiments for such validation were performed using the pair H-IgG and F-anti-H-IgG. Three experiments were conducted, and the results are shown in figure 5-6. Experiments show similar performance regarding the studied protein association. Table 5-11 establishes the values of binding kinetic constants for each experiment.

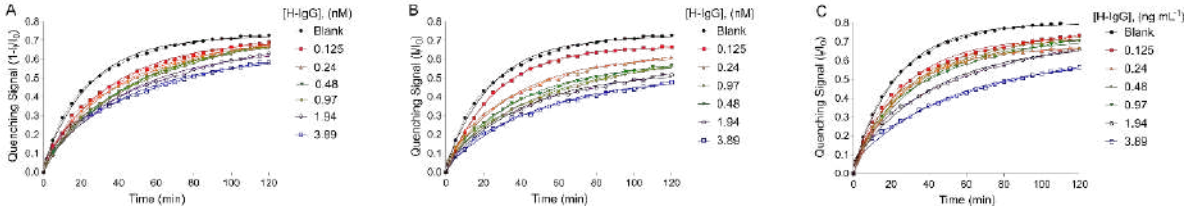

Figure 5-6. Experiments were performed in different microwell plates using the protein pair H-IgG and F-Anti-H-IgG as a model. **A.** First experiment. **B.** Second experiment. **C.** Third experiment.

Table 5-11. Binding kinetic constants of H-IgG – fluorophore-labeled Anti-H-IgG across different plates (inter-assay evaluation).

[H-IgG]; (nM)	**K_a($M^{-1}s^{-1}$)**	**K_d(s^{-1})**	**K_D(M)**
Plate 1			
0.125	3.47 x10^{08} (±0.05)	6.28 x10^{-03} (±0.2)	3.55 x10^{-11} (±0.34)
0.24	7.66 x10^{07} (±0.06)	8.43 x10^{-03} (±0.17)	2.4 x10^{-10} (±0.31)
0.48	3.1 x10^{07} (±0.06)	7.07 x10^{-03} (±0.16)	3.71 x10^{-10} (±0.31)
0.97	1.52 x10^{07} (±0.07)	7.82 x10^{-03} (±0.16)	1.44 x10^{-09} (±0.35)
1.94	7.38 x10^{06} (±0.06)	7.89 x10^{-03} (±0.13)	1.71 x10^{-09} (±0.32)
3.89	3.39 x10^{06} (±0.06)	9.82 x10^{-03} (±0.1)	3.86 x10^{-09} (±0.23)
Average	8.02 x10^{07} (±0.68)	7.89 x10^{-03} (±0.04)	1.06 x10^{-09} (±0.48)
Plate 2			
0.125	3.4 x10^{08} (±0.06)	7.25 x10^{-03} (±0.16)	3.87 x10^{-11} (±0.33)
0.24	6.29 x10^{07} (±0.06)	7.35 x10^{-03} (±0.16)	2.6 x10^{-10} (±0.3)
0.48	3.52 x10^{07} (±0.06)	8.64 x10^{-03} (±0.12)	3.95 x10^{-10} (±0.28)
0.97	1.45 x10^{07} (±0.06)	9.63 x10^{-03} (±0.09)	1.54 x10^{-09} (±0.26)
1.94	6.18 x10^{06} (±0.07)	8.73 x10^{-03} (±0.09)	1.6 x10^{-09} (±0.28)
3.89	2.74 x10^{06} (±0.07)	8.03 x10^{-03} (±0.09)	4.48 x10^{-09} (±0.24)
Average	7.69 x10^{07} (±0.66)	8.27 x10^{-03} (±0.04)	1.15 x10^{-09} (±0.5)
Plate 3			
0.125	2.84 x10^{08} (±0.05)	6.94 x10^{-03} (±0.17)	4.38 x10^{-11} (±0.31)
0.24	7.44 x10^{07} (±0.06)	7.77 x10^{-03} (±0.13)	2.04 x10^{-10} (±0.33)
0.48	3.97 x10^{07} (±0.05)	8.53 x10^{-03} (±0.16)	4.82 x10^{-10} (±0.31)
0.97	1.32 x10^{07} (±0.06)	8.45 x10^{-03} (±0.14)	1.19 x10^{-10} (±0.25)
1.94	7.56 x10^{06} (±0.06)	8.17 x10^{-03} (±0.1)	1.51 x10^{-09} (±0.31)
3.89	2.65 x10^{06} (±0.06)	9.01 x10^{-03} (±0.07)	4.49 x10^{-09} (±0.32)
Average	7.03 x10^{07} (±0.67)	8.14 x10^{-03} ($\pm$0.02)	1.14 x10^{-09} (±0.54)

To establish the inter-assay variability, it was estimated the coefficient of variation at the inter-assay level, whose results are shown in Table 5-12. As observed, such CV values did not exceed 20 %, thus, this variability is acceptable for immunoassays. Also, the drug and food administration recommended that a CV upper limit of 30 % can be accepted in those parameters obtained with immunoassays.[42,43]

Table 5-12. Coefficient of variation values at the inter-assay level: binding kinetics constants for H-IgG.

[H-IgG] (nM)	K_a(CV %)	K_d (CV %)	K_D (CV %)
0.125	10.62	7.30	10.60
0.24	10.36	6.93	12.11
0.48	12.27	10.83	14.19
0.97	7.22	10.61	12.99
1.94	10.69	5.17	6.30
3.89	13.89	9.97	8.37
Average	10.62	7.30	10.60

5.3.7 Assessment of the temporal stability of GO adhesion onto microwell surfaces

The stability of the adhesion of GO onto the surface of the microplates was also evaluated. First, half of a plate was covered with a GO concentration of 1600 µg mL^{-1} and left overnight at constant agitation (600 rpm). Then, three washing steps were made to remove the excess GO that did not attach to the microwell surface. The employed probe to evaluate the performance of quenching of fluorescence was FITC-Anti-IgG at a concentration of 0.125 µg mL^{-1}. The intensity of fluorescence was recorded every five minutes in kinetic analysis for 2 hours. Non-GO-coated microwells were also included as a control revealing the photobleaching or natural decay of the probe in each experiment. These series of experiments were conducted from 1 to 31 days and the average resulting from two plates was plotted, Figure 5-7 depicts these results, panels A and B represent the kinetic results from Day 1 to Day 31 for the control experiment and GO-modified microwells, respectively. Panel C shows the percentage of intensity of natural decay of the probe (without GO). Panel D shows the percentage of quenching of fluorescence caused by GO. All in all, the natural decay levels are below 20 % whereas the quenching of fluorescence levels are between 50 to 60 %. So, GO adhesion remains relatively stable for at least one month.

5.4 Conclusions

It was demonstrated that the proposed fluorescence quenching-based immunosensing platform is not only a versatile method for the detection of diverse proteins offering a sensitivity from the picomolar to the nanomolar range but is also a method useful for the measurement of binding kinetic constants. Moreover, results obtained according to GUI developed to binding data are in concordance with values reported in the literature and provided by the respective suppliers. Such reported data were measured with well-established methods such as SPR or immunoaffinity chromatography, which brings credibility to our method for binding kinetic analysis. However, different from such conventional techniques, our method does not require cumbersome procedures like blocking separation or washing steps. Since the interrogation occurs in the liquid phase, the biorecognition element does not need special orientation. In addition, biofunctionaliza-

tion of the sensing surface Is not required. Lastly, in general, the instrumentation needed in SPR or immunoaffinity chromatography techniques is expensive, whereas our proposal is relatively cost-effective as the assay is around 0.47 USD per test, at a laboratory scale.[44]

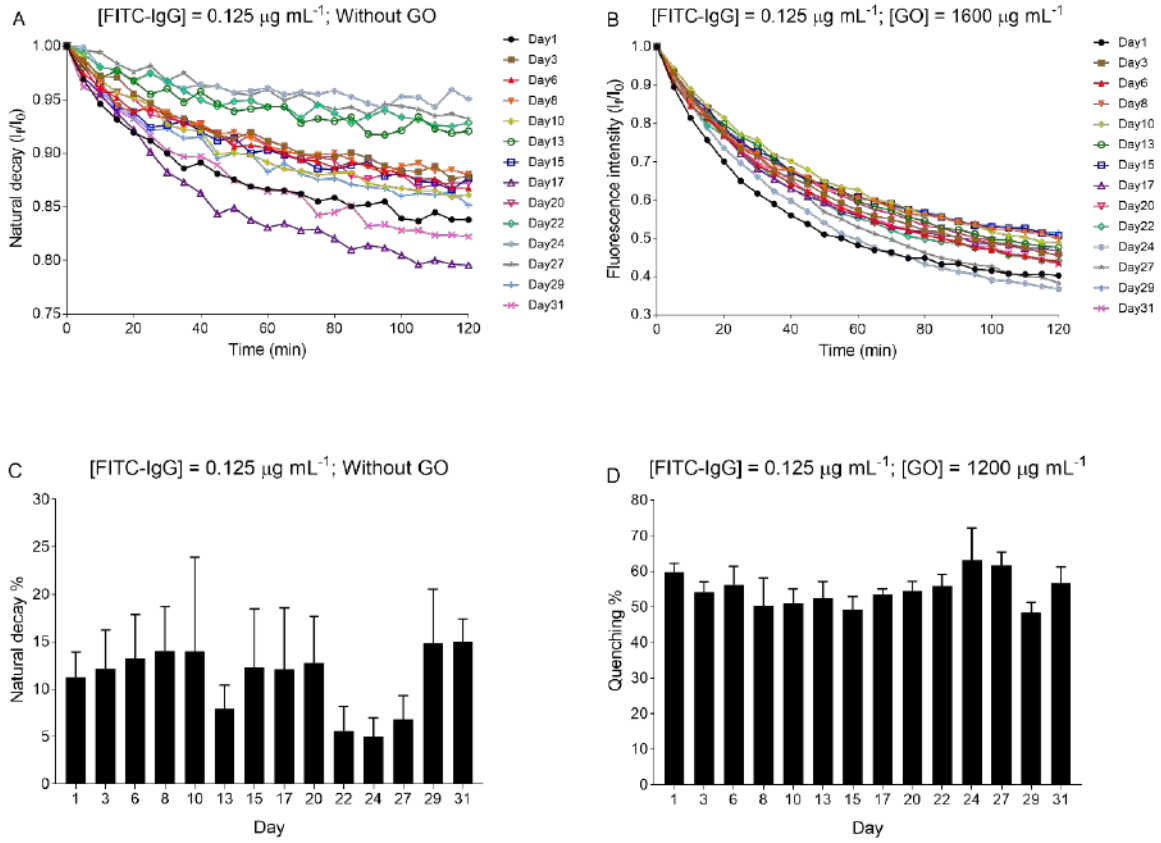

Figure 5-7. **A.** Kinetic behavior of the photoluminescent probe in nude microwells (without GO). **B.** Kinetic behavior of the probe across days in GO-modified microwells. **C.** Natural decay percentages for fluorophore without GO. **D.** Quenching of fluorescence percentages caused by GO to the fluorophore. The error bars represent the standard deviation resulting from the inter-assay analysis of two plates (3 microwells per plate) analyzed on different days.

5.5 References

1. Huang, A. T.; Garcia-Carreras, B.; Hitchings, M. D. T.; Yang, B.; Katzelnick, L. C.; Rattigan, S. M.; Borgert, B. A.; Moreno, C. A.; Solomon, B. D.; Trimmer-Smith, L.; Etienne, V.; Rodriguez-Barraquer, I.; Lessler, J.; Salje, H.; Burke, D. S.; Wesolowski, A.; Cummings, D. A. T. A Systematic Review of Antibody Mediated Immunity to Coronaviruses: Kinetics, Correlates of Protection, and Association with Severity. Nature Communications 2020, 11 (1), 4704. https://doi.org/10.1038/s41467-020-18450-4.

2. Pan, A. C.; Borhani, D. W.; Dror, R. O.; Shaw, D. E. Molecular Determinants of Drug–Receptor Binding Kinetics. Drug Discovery Today 2013, 18 (13), 667–673. https://doi.org/10.1016/j.drudis.2013.02.007.

3. Sykes, D. A.; Stoddart, L. A.; Kilpatrick, L. E.; Hill, S. J. Binding Kinetics of Ligands Acting at GPCRs. Molecular and Cellular Endocrinology 2019, 485, 9–19. https://doi.org/10.1016/j.mce.2019.01.018.

4. Lassman, M. E.; McAvoy, T.; Lee, A. Y. H.; Chappell, D.; Wong, O.; Zhou, H.; Reyes-Soffer, G.; Ginsberg, H. N.; Millar, J. S.; Rader, D. J.; Gutstein, D. E.; Laterza, O. Practical Immunoaffinity-Enrichment LC-MS for Measuring Protein Kinetics of Low-Abundance Proteins. Clin Chem 2014, 60 (9), 1217–1224. https://doi.org/10.1373/clinchem.2014.222455.

5. Singh, P. SPR Biosensors: Historical Perspectives and Current Challenges. Sensors and Actuators B: Chemical 2016, 229, 110–130. https://doi.org/10.1016/j.snb.2016.01.118.

6. Helmerhorst, E.; Chandler, D. J.; Nussio, M.; Mamotte, C. D. Real-Time and Label-Free Bio-Sensing of Molecular Interactions by Surface Plasmon Resonance: A Laboratory Medicine Perspective. Clin Biochem Rev 2012, 33 (4), 161–173.

7. Iftekhar, S.; Ovbude, S. T.; Hage, D. S. Kinetic Analysis by Affinity Chromatography. Frontiers in Chemistry 2019, 7, 673. https://doi.org/10.3389/fchem.2019.00673.

8. Ortiz-Riaño, E. J.; Avila-Huerta, M. D.; Mancera-Zapata, D. L.; Morales-Narváez, E. Microwell Plates Coated with Graphene Oxide Enable Advantageous Real-Time Immunosensing Platform. Biosensors and Bioelectronics 2020, 165, 112319. https://doi.org/10.1016/j.bios.2020.112319.

9. Morales-Narváez, E.; Merkoçi, A. Graphene Oxide as an Optical Biosensing Platform: A Progress Report. Advanced Materials 2019, 31 (6), 1805043. https://doi.org/10.1002/adma.201805043.

10. Cheeveewattanagul, N.; Morales-Narváez, E.; Hassan, A.-R. H. A.; Bergua, J. F.; Surareungchai, W.; Somasundrum, M.; Merkoçi, A. Straightforward Immunosensing Platform Based on Graphene Oxide-Decorated Nanopaper: A Highly Sensitive and Fast Biosensing Approach. Advanced Functional Materials 2017, 27 (38), 1702741. https://doi.org/10.1002/adfm.201702741.

11. Rhea, K. Determining the Binding KineticsKinetics of Peptide MacrocyclesPeptidemacrocycles Using Bio-Layer Interferometry (BLI)Bio-Layer Interferometry (BLI). In Peptide Macrocycles: Methods and Protocols; Coppock, M. B., Winton, A. J., Eds.; Springer US: New York, NY, 2022; pp 355–372. https://doi.org/10.1007/978-1-0716-1689-5_19.

12. Mitsakakis, K.; Gizeli, E. Multi-Sample Acoustic Biosensing Microsystem for Protein Interaction Analysis. Biosensors and Bioelectronics 2011, 26 (11), 4579–4584. https://doi.org/10.1016/j.bios.2011.05.030.

13. Bahadır, E. B.; Sezgintürk, M. K. A Review on Impedimetric Biosensors. null 2016, 44 (1), 248–262. https://doi.org/10.3109/21691401.2014.942456.

14. Fernandes, F. C. B.; Santos, A.; Martins, D. C.; Góes, M. S.; Bueno, P. R. Comparing Label Free Electrochemical Impedimetric and Capacitive Biosensing Architectures. Biosensors and Bioelectronics 2014, 57, 96–102. https://doi.org/10.1016/j.bios.2014.01.044.

15. Chiavaioli, F.; Baldini, F.; Tombelli, S.; Trono, C.; Giannetti, A. Biosensing with Optical Fiber Gratings. Nanophotonics 2017, 6 (4), 663–679. https://doi.org/10.1515/nanoph-2016-0178.

16. Sridevi, S.; Vasu, K. S.; Asokan, S.; Sood, A. K. Sensitive Detection of C-Reactive Protein Using Optical Fiber Bragg Gratings. Biosensors and Bioelectronics 2015, 65, 251–256. https://doi.org/10.1016/j.bios.2014.10.033.

17. Jung, J.; Bong, J.-H.; Lee, S. J.; Kim, M.-J.; Sung, J. S.; Lee, M.; Kang, M.-J.; Song, J.; Jose, J.; Pyun, J.-C. Screening of Fv Antibodies with Specific Binding Activities to Monosodium Urate and Calcium Pyrophosphate Dihydrate Crystals for the Diagnosis of Gout and Pseudogout. ACS Appl. Bio Mater. 2021, 4 (4), 3388–3397. https://doi.org/10.1021/acsabm.0c01680.

18. Tardivo, M.; Toffoli, V.; Fracasso, G.; Borin, D.; Dal Zilio, S.; Colusso, A.; Carrato, S.; Scoles, G.; Meneghetti, M.; Colombatti, M.; Lazzarino, M. Parallel Optical Read-out of Micromechanical Pillars Applied to Prostate Specific Membrane Antigen Detection. Biosensors and Bioelectronics 2015, 72, 393–399. https://doi.org/10.1016/j.bios.2015.05.026.

19. Zhou, Y.; Wang, P.; Xiong, J.; Yue, H.; He, Y.; Ouyang, H.; Wang, L.; Fu, Z. A Label-Free Strategy for Measuring the Affinity between Monoclonal Antibody and Hapten Using Microdialysis Sampling Combined with Chemiluminescent Detection. Biosensors and Bioelectronics 2017, 87, 404–409. https://doi.org/10.1016/j.bios.2016.08.068.

20. Viter, R.; Savchuk, M.; Iatsunskyi, I.; Pietralik, Z.; Starodub, N.; Shpyrka, N.; Ramanaviciene, A.; Ramanavicius, A. Analytical, Thermodynamical and Kinetic Characteristics of Photoluminescence Immunosensor for the Determination of Ochratoxin A. Biosensors and Bioelectronics 2018, 99, 237–243. https://doi.org/10.1016/j.bios.2017.07.056.

21. Song, D.; Yang, R.; Wang, H.; Fang, S.; Liu, Y.; Long, F.; Zhu, A. Development of Dual-Color Total Internal Reflection Fluorescence Biosensor for Simultaneous Quantitation of Two Small Molecules and Their Affinity Constants with Antibodies. Biosensors and Bioelectronics 2019, 126, 824–830. https://doi.org/10.1016/j.bios.2018.12.010.

22. Plikusiene, I.; Balevicius, Z.; Ramanaviciene, A.; Talbot, J.; Mickiene, G.; Balevicius, S.; Stirke, A.; Tereshchenko, A.; Tamosaitis, L.; Zvirblis, G.; Ramanavicius, A. Evaluation of Affinity Sensor Response Kinetics towards Dimeric Ligands Linked with Spacers of Different Rigidity: Immobilized Recombinant Granulocyte Colony-Stimulating Factor Based Synthetic Receptor Binding with Genetically Engineered Dimeric Analyte Derivatives. Biosensors and Bioelectronics 2020, 156, 112112. https://doi.org/10.1016/j.bios.2020.112112.

23. Giakoumakis, N. N.; Rapsomaniki, M. A.; Lygerou, Z. Analysis of Protein Kinetics Using Fluorescence Recovery After Photobleaching (FRAP). In Light Microscopy: Methods and Protocols; Markaki, Y., Harz, H., Eds.; Springer New York: New York, NY, 2017; pp 243–267. https://doi.org/10.1007/978-1-4939-6810-7_16.

24. Bosma, R.; Stoddart, L. A.; Georgi, V.; Bouzo-Lorenzo, M.; Bushby, N.; Inkoom, L.; Waring, M. J.; Briddon, S. J.; Vischer, H. F.; Sheppard, R. J.; Fernández-Montalván, A.; Hill, S. J.; Leurs, R. Probe Dependency in the Determination of Ligand Binding Kinetics at a Prototypical G Protein-Coupled Receptor. Scientific Reports 2019, 9 (1), 7906. https://doi.org/10.1038/s41598-019-44025-5.

25. Falconer, R. J.; Schuur, B.; Mittermaier, A. K. Applications of Isothermal Titration Calorimetry in Pure and Applied Research from 2016 to 2020. Journal of Molecular Recognition 2021, 34 (10), e2901. https://doi.org/10.1002/jmr.2901.

26. Knezevic, J.; Langer, A.; Hampel, P. A.; Kaiser, W.; Strasser, R.; Rant, U. Quantitation of Affinity, Avidity, and Binding Kinetics of Protein Analytes with a Dynamically Switchable Biosurface. J. Am. Chem. Soc. 2012, 134 (37), 15225–15228. https://doi.org/10.1021/ja3061276.

27. Oshannessy, D. J.; Brighamburke, M.; Soneson, K. K.; Hensley, P.; Brooks, I. Determination of Rate and Equilibrium Binding Constants for Macromolecular Interactions Using Surface Plasmon Resonance: Use of Nonlinear Least Squares Analysis Methods. Analytical Biochemistry 1993, 212 (2), 457–468. https://doi.org/10.1006/abio.1993.1355.

28. Gavin, H. P. The Levenberg-Marquardt Algorithm for Nonlinear Least Squares Curve-Fitting Problems; 2019.

29. Virtanen, P.; Gommers, R.; Oliphant, T. E.; Haberland, M.; Reddy, T.; Cournapeau, D.; Burovski, E.; Peterson, P.; Weckesser, W.; Bright, J.; van der Walt, S. J.; Brett, M.; Wilson, J.; Millman, K. J.; Mayorov, N.; Nelson, A. R. J.; Jones, E.; Kern, R.; Larson, E.; Carey, C. J.; Polat, İlhan; Feng, Y.; Moore, E. W.; VanderPlas, J.; Laxalde, D.; Perktold, J.; Cimrman, R.; Henriksen, I.; Quintero, E. A.; Harris, C. R.; Archibald, A. M.; Ribeiro, A. H.; Pedregosa, F.; van Mulbregt, P.; SciPy 1.0 Contributors. SciPy 1.0: Fundamental Algorithms for Scientific Computing in Python. Nature Methods 2020, 17, 261–272. https://doi.org/10.1038/s41592-019-0686-2.

30. Pedregosa, F.; Varoquaux, G.; Gramfort, A.; Michel, V.; Thirion, B.; Grisel, O.; Blondel, M.; Prettenhofer, P.; Weiss, R.; Dubourg, V.; Vanderplas, J.; Passos, A.; Cournapeau, D.; Brucher, M.; Perrot, M.; Duchesnay, E. Scikit-Learn: Machine Learning in Python. Journal of Machine Learning Research 2011, 12, 2825–2830.

31. Stubenrauch, K.; Wessels, U.; Essig, U.; Kowalewsky, F.; Vogel, R.; Heinrich, J. Characterization of Murine Anti-Human Fab Antibodies for Use in an Immunoassay for Generic Quantification of Human Fab Fragments in Non-Human Serum Samples Including Cynomolgus Monkey Samples. Journal of Pharmaceutical and Biomedical Analysis 2013, 72, 208–215. https://doi.org/10.1016/j.jpba.2012.08.023.

32. Kumada, Y.; Hasegawa, Y.; Horiuchi, J. Efficient and Robust Isolation of Rabbit ScFv Antibodies Using Antigen-Coupled Multilamellar Vesicles. Journal of Bioscience and Bioengineering 2021, 131 (3), 299–304. https://doi.org/10.1016/j.jbiosc.2020.10.007.

33. Sinibaldi, A.; Occhicone, A.; Munzert, P.; Danz, N.; Sonntag, F.; Michelotti, F. Label-Free Monitoring of Human IgG/Anti-IgG Recognition Using Bloch Surface Waves on 1D Photonic Crystals. Biosensors 2018, 8 (3). https://doi.org/10.3390/bios8030071.

34. Ouellet, E.; Lausted, C.; Lin, T.; Yang, C. W. T.; Hood, L.; Lagally, E. T. Parallel Microfluidic Surface Plasmon Resonance Imaging Arrays. Lab Chip 2010, 10 (5), 581–588. https://doi.org/10.1039/B920589F.

35. Schlatter, D.; Barner, R.; Fattinger, Ch.; Huber, W.; Hübscher, J.; Hurst, J.; Koller, H.; Mangold, C.; Müller, F. The Difference Interferometer: Application as a Direct Affinity Sensor. Biosensors and Bioelectronics 1993, 8 (2), 109–116. https://doi.org/10.1016/0956-5663(93)80059-X.

36. Abraham, R.; Buxbaum, S.; Link, J.; Smith, R.; Venti, C.; Darsley, M. Determination of Binding Constants of Diabodies Directed against Prostate-Specific Antigen Using Electrochemiluminescence-Based Immunoassays. Journal of Molecular Recognition 1996, 9 (5–6), 456–461. https://doi.org/10.1002/(SICI)1099-1352(199634/12)9:5/6<456::AID-JMR282>3.0.CO;2-8.

37. Paus, E.; Nustad, K.; Børmer, O. P. Epitope Mapping and Affinity Estimation of 83 Antibodies against Prostate-Specific Antigen. Tumor Biology 1999, 20(suppl 1) (Suppl. 1), 52–69. https://doi.org/10.1159/000056531.

38. Damborský, P.; Madaboosi, N.; Chu, V.; Conde, J. P.; Katrlík, J. Surface Plasmon Resonance Application in Prostate Cancer Biomarker Research. Chemical Papers 2015, 69 (1), 143–149. https://doi.org/10.1515/chempap-2015-0053.

39. Corey, E.; Wegner, S. K.; Stray, J. E.; Corey, M. J.; Arfman, E. W.; Lange, P. H.; Vessella, R. L. Characterization of 10 New Monoclonal Antibodies against Prostate-Specific Antigen by Analysis of Affinity, Specificity and Function in Sandwich Assays. International Journal of Cancer 1997, 71 (6), 1019–1028. https://doi.org/10.1002/(SICI)1097-0215(19970611)71:6<1019::AID-IJC18>3.0.CO;2-8.

40. Chi, X.; Liu, X.; Wang, C.; Zhang, X.; Li, X.; Hou, J.; Ren, L.; Jin, Q.; Wang, J.; Yang, W. Humanized Single Domain Antibodies Neutralize SARS-CoV-2 by Targeting the Spike Receptor Binding Domain. Nature Communications 2020, 11 (1), 4528. https://doi.org/10.1038/s41467-020-18387-8.

41. Kim, C.; Ryu, D.-K.; Lee, J.; Kim, Y.-I.; Seo, J.-M.; Kim, Y.-G.; Jeong, J.-H.; Kim, M.; Kim, J.-I.; Kim, P.; Bae, J. S.; Shim, E. Y.; Lee, M. S.; Kim, M. S.; Noh, H.; Park, G.-S.; Park, J. S.; Son, D.; An, Y.; Lee, J. N.; Kwon, K.-S.; Lee, J.-Y.; Lee, H.; Yang, J.-S.; Kim, K.-C.; Kim, S. S.; Woo, H.-M.; Kim, J.-W.; Park, M.-S.; Yu, K.-M.; Kim, S.-M.; Kim, E.-H.; Park, S.-J.; Jeong, S. T.; Yu, C. H.; Song, Y.; Gu, S. H.; Oh, H.; Koo, B.-S.; Hong, J. J.; Ryu, C.-M.; Park, W. B.; Oh, M.;

Choi, Y. K.; Lee, S.-Y. A Therapeutic Neutralizing Antibody Targeting Receptor Binding Domain of SARS-CoV-2 Spike Protein. Nature Communications 2021, 12 (1), 288. https://doi.org/10.1038/s41467-020-20602-5.

42. Want, E. J.; Wilson, I. D.; Gika, H.; Theodoridis, G.; Plumb, R. S.; Shockcor, J.; Holmes, E.; Nicholson, J. K. Global Metabolic Profiling Procedures for Urine Using UPLC–MS. Nature Protocols 2010, 5 (6), 1005–1018. https://doi.org/10.1038/nprot.2010.50.

43. Want, E. J.; Masson, P.; Michopoulos, F.; Wilson, I. D.; Theodoridis, G.; Plumb, R. S.; Shockcor, J.; Loftus, N.; Holmes, E.; Nicholson, J. K. Global Metabolic Profiling of Animal and Human Tissues via UPLC-MS. Nature Protocols 2013, 8 (1), 17–32. https://doi.org/10.1038/nprot.2012.135.

44. Avila-Huerta, M. D.; Ortiz-Riaño, E. J.; Mancera-Zapata, D. L.; Cortés-Sarabia, K.; Morales-Narváez, E. Facile Determination of COVID-19 Seroconversion via Nonradiative Energy Transfer. ACS Sens. 2021, 6 (6), 2136–2140. https://doi.org/10.1021/acssensors.1c00795.

Final Remarks and Outlook

We developed a novel fluorescence quenching-based immunosensing platform for the detection of clinically relevant proteins such as Human immunoglobulin G, Prostate Specific Antigen, Heat Shock Protein 72, and antibodies against SARS-CoV-2. The quenching of fluorescence is caused by Förster resonance energy transfer FRET between graphene oxide (the acceptor) and the respective fluorophore (the donor) used in each configuration. In general, the quenching efficiency was around 60 to 70 % for FITC fluorophore and 50 to 60 % for QDs. So, the immunosensing platform is not limited to a specific fluorophore, and therefore diverse can be used for the detection of proteins. This is on account of the broad absorption spectrum of GO (with an absorption peak at about 233 nm[1]) since FRET occurs where the absorption spectrum of the acceptor overlaps with the emission spectrum of the donor.

H-IgG was the first analyte employed in the immunosensing platform. H-IgG was detected in the dynamic range from 9.37 to 600 ng mL^{-1}, with a concentration of the biosensing probe (Anti-H-IgG-FITC) of 0.125 µg mL^{-1}, GO concentration of 1600 µg mL^{-1}, and a volume of 200 µL per microwell (100 µL of the biosensing probe and 100 µL of each analyte concentration). The optimal time of assay was 60 minutes since both the coefficient of determination of the linear fitting and LOD were the highest of intervals analyzed 0.98 and 2.38 ng mL^{-1}, respectively. The LOQ obtained was 15.5 ng mL^{-1} and the coefficient of variation percentages go from 0.69 to 4.8 % reflecting an excellent intra-assay precision. The Prostate Specific Antigen PSA is a protein used as a biomarker of prostate cancer. Biotin Anti-PSA concentrated at 28 ng mL^{-1} was conjugated with Streptavidin-QDs concentrated at 0.05 nM forming then the biosensing probe for the assay of PSA. The concentration of GO used was 1400 µg mL^{-1} and the dynamic range of PSA goes from 0.15 to 10 ng mL^{-1}. The optimal assay time for PSA detection was 90 minutes with a LOD and LOQ of 0.049 and 0.3 ng mL^{-1}, respectively. The intra-assay precision was excellent with percentages less than 15 %. For Heat Shock Protein 72 the dynamic range of detection goes from 0.78 to 50 ng mL^{-1}, with an optimal assay time of 90 minutes obtaining a LOD and LOQ of 0.68 and 3.05 ng mL^{-1}, respectively. The intra-assay precision percentages were below 4 %. So, it was possible to obtain excellent limits of detection and quantification for every analyte analyzed which is the fundamental importance in the development of immunosensing systems. In addition, it is a highly transformative approach since can operates not only with different analytes but also with organic dye-conjugated antibodies and streptavidin-QDs conjugated to biotinylated antibodies due to the universal fluorescence quenching ability of GO this immunosensing platform can work at different wavelengths. Moreover, a single antibody conjugated with a fluorophore is necessary for its operation avoiding cumbersome procedures such as blocking, washing, or separation steps which contribute to saving valuable time and

reagents. Intra-assay precision was obtained for every analyte tested and, in general, percentages do not exceed 15 %, indicating high precision in measurements, and therefore low dispersion of data.

Additionally, the GO-based immunosensing platform can be used for the qualitative immunosensing of real samples as demonstrated in the assay of urinary Hsp72 samples from patients diagnosed with AKI, even at different stages of AKI disease, or the determination of COVID-19 seroconversion from human serum samples with statistical significance. We could qualitatively classify the urine samples where all negative samples were below the blank sample whereas AKI samples (positive samples) are above LOD and below of Hsp72 concentration of 12 ng mL^{-1}. These results were obtained at the optimal assay time for Hsp72 detection which was 90 minutes. This is just a qualitative analysis that permits arguing the coherence of results due to the lack of experimentation with more urine samples related to AKI. All in all, urinary Hsp72 samples from patients diagnosed with AKI can be potentially tested by our immunoassay proposal even at different stages of AKI disease. On the other hand, we can argue that the immunosensing platform proposed is also suitable for the qualitative detection of antibodies against SARS-CoV-2 in serum samples. However, a limiting factor is that the specific detection of COVID-19 antibodies in serum samples through this approach may be restricted due to cross-reactivity with other antibodies for instance IgA or IgM which are also present in the serum samples.[2] The direct comparison of serum samples (in optimal biosensing conditions) with the calibration curve, as done for Hsp72, was not possible since all the serum samples from COVID-19 subjects yielded I_f/I_0 values exceeding the dynamic range of the optimized calibration curve.

Compared with the gold standard of the immunoassays ELISA, our immunosensing platform just need a single antibody for the capture and detection process whereas in ELISA at least two antibodies are involved. Also, that method includes some cumbersome procedures like washing, blocking, and separation steps and our proposal is a single-step method. In general, LOD obtained with our method are in the same order that ELISA from ng mL^{-1} to pg mL^{-1}, but with our proposal, the interrogation process can be followed in real-time whereas ELISA can be made at the end of the process.

Importantly, our immunosensing method is also useful for the measurement of binding kinetic constants. Moreover, results obtained (according to the GUI developed to binding data) were in concordance with values reported in the literature and provided by the respective suppliers. Such reported data were measured with well-established methods such as SPR or immunoaffinity chromatography, which brings credibility to our method for binding kinetic analysis. However, different from such conventional techniques, our method does not require cumbersome procedures like blocking separation or washing steps. Since the interrogation occurs in the liquid phase, the biorecognition element does not need special orientation, and it does not require the biofunctionalization of the sensing surface. The variability of our immunosensing platform for the determination of binding kinetics constants at the interassay level was assessed. CV values did not exceed 20 %, thus, this variability is acceptable for immunoassays. Lastly, in general, the instrumentation needed in SPR or immunoaffinity chromatography techniques is expensive, whereas our proposal is relatively cost-effective as the assay is around 0.47 USD per test, at a laboratory scale.

The period during the natural course of a disease where symptoms are not yet ap-

parent, but the disease is biologically present is known as the preclinical phase. In the last years, the interest for discover biomarkers that permit the early diagnosis of diseases has increased. In this work was mentioned that PSA and Hsp72 are biomarkers used for the preclinical diagnosis of Prostate cancer and Acute Kidney Injury, respectively. It was mentioned that normal PSA levels in the blood are $\leq$ 4 ng mL-1, and normal urinary levels of Hsp72 are $\leq$ 4.9 ng mL-1. Through our fluorescence quenching-based immunosensing platform we could detect such analytes with LOD values below these values. Therefore, it is a potential method for the preclinical diagnosis of prostate cancer and AKI. On the other hand, our immunosensing platform also has the potential to monitor the association process of proteins, and consequently, can be used in biosensing for the determination of the antibody affinity, in biochemistry studies where the understanding of structure/function relationships are in function of protein-protein interactions, or even in the validation of potential biomarkers which are made in terms of binding kinetic parameters. Future work is related to applying the fluorescence quenching-based immunosensing platform for the detection of more clinically relevant proteins, and testing such proteins in real samples to improve the validation of the method in the preclinical scenario and have more statistical results contributing to such validation. Likewise, transferring the technique to point-of-care testing devices is an important step since these types of devices are frequently used in the healthcare industry and are performed outside of the laboratory setting.

1. Saxena, S.; Tyson, T. A.; Shukla, S.; Negusse, E.; Chen, H.; Bai, J. Investigation of Structural and Electronic Properties of Graphene Oxide. Appl. Phys. Lett. 2011, 99 (1), 013104. https://doi.org/10.1063/1.3607305.

2. Avila-Huerta, M. D.; Ortiz-Riaño, E. J.; Mancera-Zapata, D. L.; Cortés-Sarabia, K.; Morales-Narváez, E. Facile Determination of COVID-19 Seroconversion via Nonradiative Energy Transfer. ACS Sens. 2021, 6 (6), 2136–2140. https://doi.org/10.1021/acssensors.1c00795.